IDENTIFYING PERFORMANCE CRITERIA OF FULLY BIORESORBABLE SCAFFOLDS FOR ENDOVASCULAR APPLICATIONS

by

Jahid Ferdous

Bachelor of Science
Bangladesh University of Engineering and Technology 2005

Master of Engineering
Nanyang Technological University 2009

Submitted in Partial Fulfillment of the Requirements

for the Degree of Doctor of Philosophy in

Biomedical Engineering

College of Engineering and Computing

University of South Carolina

2014

Accepted by:

Tarek Shazly, Major Professor

Melissa Moss, Committee Member

James Blanchette, Committee Member

Jamil Khan, Committee Member

Lacy Ford, Vice Provost and Dean of Graduate Studies

Abstract

Background: Bioresorbable scaffolds (BRS) have revolutionized percutaneous coronary intervention in clinical cardiovascular medicine. As opposed to permanent alternatives such as metallic stents, BRS have an inherent potential to reduce the occurrence of untoward events such as vessel re-narrowing or thrombosis by virtue of undergoing complete and controlled resorption post- implantation. While BRS platforms demonstrate a clear potential to mitigate risk stemming from incomplete vessel healing, they introduce a new set of considerations to clinical safety and efficacy. Foremost among these issues is the fate of and biological response to material by-products that evolve throughout the scaffold degradation and erosion processes, motivating a comprehensive assessment of how material design and deployment parameters impact scaffold performance in the arterial environment.

Dissertation summary: The overall goal of this project is to identify performance criteria of BRS for endovascular applications. First, we develop a computational model to predict scaffold by-product generation and release throughout the tissue healing process. Parametric studies are used to elucidate the material and deployment parameters which most significantly modulate by-product fate and thus patient risk. We next perform an array of in vitro studies to understand how BRS fracture risk depends on the expansion ratio imparted at implantation. Due to the inherent potential for fracture during endovascular delivery, BRS over-expansion is a more serious concern as compared to analogous deployment of metallic stents. Conversely, under-expansion increases the risk of thrombosis due to an alteration of in situ geometry and concomitant disturbance of arterial blood flow. To gain insight on the effects of scaffold expansion, computational studies are complemented by in vitro measures of BRS erosion, degradation, radial strength, and drug delivery kinetics under plausible alterations of the degree of expansion. Finally, a dynamic flow system which mimics arterial blood flows is developed and used to study the effects of the specific implantation site on BRS performance. Taken together, the studies encompassed in this dissertation provide an efficient means for iterative evaluation of candidate scaffolds as well as the basis to optimize material design and delivery strategies as this technology continues to evolve.

Table of Contents

List of Tables

List of Figures

Chapter 1

INTRODUCTION

1.1 Overview

Ischaemic Artery Disease

Ischaemic heart disease (IHD) is the leading cause of death on a national and global scale. According to the world health organization, IHD associated mortality in the world was 12.8% of total deaths (7.25 millions) and in developed countries 15.6% of total deaths in 2008 (1.42 million) in 2008 [35]. Atherosclerosis, the narrowing of arterial lumen due to deposition of fatty substances and proliferation of smooth muscle cell (SMC) in the artery, is the most common cause of IHD. Elevated levels of cholesterol, hypertension, smoking and other hemodynamic factors damage the innermost layer of an artery, the endothelium, which trigger fatty substance absorption and provokes SMC proliferation (Figure 1.1). Reduction of arterial blood flow due to atherosclerosis restricts downstream nutrients transport that may permanently damage segment of heart muscle and eventually lead to myocardial infarction.

Percutaneous Coronary Intervention

The physical condition of patient, possibility of future complications, the extent of severity and type of the artery jointly determine the mode of treatment for atherosclerosis. Coronary artery bypass graft (CABG) is preferred for patients having multiple blockages and diabetes [78], where arteries from a different part of the body are grafted adjacent to the diseased regions to redirect the blood flow. In less com-

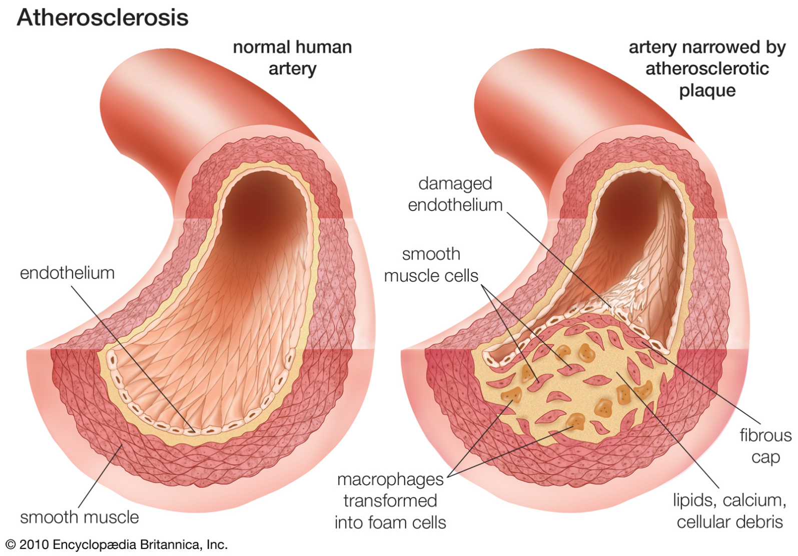

Figure 1.1 Mechanism of atherosclerosis [34].

plicated conditions with partial occlusion and more stable atherosclerotic plaques, percutaneous coronary intervention (PCI) is implemented either using percutaneous transluminal coronary angioplasty (PTCA) or a stent/scaffold.

Introduction of PTCI by Andreas Grüentzig in 1977 started new clinical era of revascularization [29]. A balloon-tipped catheter is inserted in the body and inflated in the diseased region to open the artery and restore downstream blood flow. However, PTCA patency is primarily limited by acute recoiling, constrictive remodeling, and healing response for neointimal hyperplasia (Table 1.1) [63].

Bare metal stents (BMS) was the next breakthrough technology in interventional cardiology where metallic scaffold is permanently implanted at the stenotic region. First human implantations of a self-expanding and balloon-expandable BMS were in 1986 and 1987, respectively [77, 64]. Although BMS shows few beneficial aspects over balloon angioplasty in terms of acute occlusion and recoiling, increases in the risk of thrombosis and restenosis are notable (Table 1.1). Vascular injury during BMS implantation leads to neointimal hyperplasia and requires re-intervention in many patients [21].

The third generation technology in the PCI field was drug-eluting stet (DES), where an active therapeutic agent (antiproliferative or immunosuppressant) is either coated directly on the metal surface or loaded within a polymer coating on the metal surface. DES effectively reduces the rate of restenosis via inhibition of SMC proliferation and migration. The first approved DES by Federal Drug and Administration (FDA) was Cypher stent (Johnson and Johnson, USA) containing immunosuppressant sirolimus/rapamycin in 2003. Antiproliferative paclitaxel based DES, Taxus stent (Boston, USA), was approved by FDA in 2004. Zotarolimu based Endeavor stent (Medtronic, USA) and everolimus based Xience V stent (Abbott, USA) also got approval from FDA in 2008. However, the long term outcome is not satisfactory due to increased risk of late and very late stent thrombosis (Table 1.1) [63, 60, 27].

The future of interventional cardiology is projected to be dominated by fully bioresorbable scaffolds (BRS), a potentially ideal solution for obstructive coronary disease. The first BRS was developed and implanted in animals in mid-1980s at Duke University [80]. Since then, researchers are trying to understand different aspects associated with BRS that must be overcome prior to clinical implementation.

Bioresorbable Scaffolds

BRS have several inherent potential advantages over all other PCI technologies [60, 27]. Following balloon angioplasty, mechanical support is only temporally required during the healing period to prevent immediate recoiling - this can be achieved with sufficiently stiff BRS. The synchrony between scaffold resorption and tissue healing can potentially address stent thrombosis, vessel vasomotion, late luminal enlargement, and late expansive remodeling. BRS can be designed to confer minimal injury as viscoelastic behavior of most degradable materials favors less-chronic deployment [12, 74]. Moreover, BRS implantation does not preclude repeated interventions at the treated site, which is sometimes required and problematic with permanent implants. As with DES, BRS can be used as a reservoir for local drug delivery. Drug pharmacokinetics can be controlled through tuning materials physical and structural properties like resorption rate, composition, and morphology.

The first clinical trial of BRS was performed with poly-l-lactide (PLLA) based Igaki-Tamai stent in 2000, which completely degraded between 18 to 24 months [83]. In months follow up, low restenosis rate and re-intervention rate of 10.5% along with 0.48 mm angiographic loss index were reported. No negative vessel remodeling or luminal narrowing was also reported after 2 years of implantation (Table 1.2).

Table 1.1 Potential advantages of BRS different PCI techniques [63, 60].

	Balloon Angioplasty	Bare Metal Stent	Metallic Drug-eluting Stent	Bioresorbable Scaffold
Acute occlusion	-	+	+	+
Acute scaffold thrombosis	NA	-	+/-	+
Subacute scaffold thrombosis	NA	-	-	+
Acute recoil	-	+	+	+
Constrictive remodeling	-	+	+	+
Neointimal hyperplasia	-	-	+	+
Expansive remodeling	+	-	-	+
Late luminal enlargement	+	-	-	+
Late ST/scaffold thrombosis	NA	-	-	+
Acute occlusion	-	+	+	+

+ = Prevented; - = Not prevented; NA = Not applicable.

The absorbable metallic stent, AMS-1 (Biotronik, Germany) was the first metallic BRS primarily composed of magnesium (Mg) [18]. After two major revisions, AMS-3 was designed to reduce neointimal hyperplasia through incorporating bioresorbable matrix for controlled release of antiproliferative drug delivery [60].

The REVA stent (Boston Scientific, USA) is a fabricated from poly(tyrosine carbonate). This radiopaque BRS has a noble mechanical locking mechanism, side-and-lock design, which potentially addresses acute stent recoil [44]. BTI stent (Bioabsorbable Therapeutics Inc, Menlo Park, CA) consists of a backbone of polyanhydride ester based on salicyclic acid and adipic acid anhydride with sirolimus coating. It takes 9-12 months to fully degrade, whereas complete drug elution takes place within 30 days [39].

Bioresorbable vascular scaffold, BVS, (Abbott, USA) is a PLLA based BRS containing everolimus drug. Two year follow-up data from the ABSORB trial shows no cardiac death, re-intervention, or stent thrombosis. After 24 months of implantation,

Table 1.2 Currently available BRS in clinical trials [60].

Product	Strut Materials	Coating Materials	Absorption Products	Drug Elution	Duration Radial Support	Absorption Time	Late Loss @ 6 months	TLR*
Igaki-Tamai	PLLA	Nil	LA,CO_2, H_2O	Nil	6 months	2 years	0.44 mm	6.7% @ 6 months
AMS-3	Metal-Mg alloy	Nil	NA	Nil	Weeks	>4 months	0.68 mm	9.1% @ 6 months
REVA	PDTE Carbonate	Nil	Amino acid, Ethanol, CO_2	Yes	3-6 months	2 years	1.81 mm	67% @ 1 year
BTI	Polymer Salicylate + linker	Salicylate + different linker	Salicylate, CO_2, H_2O	Sirolimus Salicylate	3 months	6 months		
BVS 1.1	PLLA	Poly-D,L-lactide	LA,CO_2, H_2O	Everolimus	3 months	2 years	0.19 mm	3.6% @ 1 year

*TLR = Target Lesion Revascularization; NA = Not Applicable.

the entire scaffold is absorbed in a porcine coronary model, whereas all drugs are eluted within 4 months. Revised versions of this BRS, BVS 1.1, shows improved performance with angiographic late loss of 0.19 mm [73].

1.2 Scope

Despite some encouraging outcomes over the first 25 years of BRS clinical deployment, this technology is still under-utilized due to a myriad of concerns and only partially understood risk factors. Several distinct challenges need to be overcome for BRS technology to displace current metallic DES in percutaneous interventions. The following open questions, hypotheses and specific aims drive this project, which seeks to ultimately provide a basis for continued advancement of BRS technologies.

Open Questions

1. What are the factors that dictate the fate of material by-products following BRS implantation?
2. Can released drug and developed material by-product kinetics be independently tuned in BRS applications?
3. What factors determine the optimal residence time for BRS?
4. Will deployment parameters, such as immediate environment and utilized expansion, significantly impact BRS performance?

Hypotheses

1. BRS by-product retention and distribution within arterial tissue are dictated by a complex interplay between polymer degradation, vascular remodeling, and metabolic clearance.

2. Several intrinsic material properties that can be controlled during the manufacturing process will have differential impact on various metrics of BRS performance.

3. The degree of BRS radial expansion impact the physical properties of the constituent polymeric network and as a result attenuate metrics of scaffold performance.

4. Fluid flow enhances the clearance of soluble by-products, and as a result reduces the autocatalytic component of BRS degradation.

Specific Aims

1. Develop a physics-based computational model that characterizes the bulk degradation and by-product transport from a BRS.

2. Develop a mathematical model to quantify how compositional and structural parameters affect key metrics of BRS performance.

3. Characterize the effect of radial expansion on scaffold performance and drug pharmacokinetics using a representative drug-eluting BRS.

4. Quantify time-dependent BRS properties following submersion in static and dynamic medium, including alterations in scaffold mechanical properties, retained mass, and network structure.

Chapter 2

ASSESSMENT OF MATERIAL BY-PRODUCT FATE FROM BIORESORBABLE VASCULAR SCAFFOLDS

[1]

2.1 Abstract

Fully bioresorbable vascular scaffolds (BVS) are attractive platforms for the treatment of ischemic artery disease owing to their intrinsic ability to uncage the treated vessel after the initial scaffolding phase, thereby allowing for the physiological conditioning that is essential to cellular function and vessel healing. Although scaffold erosion confers distinct advantages over permanent endovascular devices, high transient by-product concentrations within the arterial wall could induce inflammatory and immune responses. To better understand these risks, we developed an integrated computational model that characterizes the bulk degradation and by-product fate for a representative BVS comprised of poly(L-lactide) (PLLA). Parametric studies were conducted to evaluate the relative impact of PLLA degradation rate, arterial remodeling, and metabolic activity on the local lactic acid (LA) concentration within arterial tissue. The model predicts that both tissue remodeling and PLLA degradation kinet-

---

[1] Shazly T., Kolachalama V. B., Ferdous, J., Oberhauser J. P., Hossainy S., and Edelman E. R. 2012. *Annals of Biomedical Engineering.* 40(4): 955-965.
Reprinted here with permission of publisher.

ics jointly modulate LA fate and suggests that a synchrony of these processes could minimize transient concentrations within local tissue. Furthermore, simulations indicate that LA metabolism is a relatively poor tissue clearance mechanism compared to convective and diffusive transport processes. Mechanistic understanding of factors governing by-product fate may provide further insights on BVS outcome and facilitate development of future generation scaffolds.

2.2 Introduction

Percutaneous coronary intervention (PCI) has transformed clinical cardiovascular medicine. Polymer-coated, metallic drug-eluting stents (DES) serve as permanent implants that prevent vessel re-narrowing and control the release of antiproliferative pharmacological compounds intended to attenuate the neointimal hyperplastic response. However, issues related to incomplete vessel healing characterized by poor re-endothelialization, stent thrombosis, and late clinical fatalities create concerns about the long-term effects of metallic-based stent platforms [42, 38, 32]. Emerging technologies attempting to mitigate these risks are now gaining impetus, and in particular, bioresorbable vascular scaffolds (BVS) comprised of fully resorbable polymers are being evaluated pre-clinically and clinically across various vascular beds [12, 40]. While BVS platforms demonstrate a clear potential to mitigate risk stemming from incomplete vessel healing, they introduce a new set of considerations to clinical safety and efficacy. Foremost among these issues is the fate of and biological response to material by-products that evolve throughout the scaffold degradation and resorption processes. Several studies have quantified biodegradable material behavior *in vitro* and *in vivo* [49, 90, 65], but the physical and chemical factors that govern by-product fate and associated biological response are difficult to quantify in traditional experimental settings.

Computational modeling offers an efficient framework to predict and understand the behavior of resorbable implants. Aliphatic polyesters are a class of polymers for which the erosion process is typically modeled using a reaction-transport framework, where degradation is dictated by an autocatalytic hydrolysis mechanism and transport includes diffusion through the polymer matrix [25, 76, 9]. Reaction-transport models have been applied to a range of aliphatic polyesters, including poly(orthoester), poly(4-methylcaprolactone), poly(caprolactone), poly(L-lactide) (PLLA), and poly(D,L-lactide-co-glycolide) [84]. Hybrid models that employ stochastic reaction frameworks are mathematically complex but offer greater detail of transient polymer composition [10, 79]. Despite these and other efforts [4, 31, 66], previous models have not been extended to characterize the various kinetic factors that modulate by-product fate in the arterial environment. We have applied a reaction-transport framework to study how the outcome of material by-products released from a tissue-embedded BVS is governed by the hydrolytic degradation rate of the polymer, vascular remodeling, and arterial uptake.

We present a three-dimensional computational model of a BVS that is primarily composed of PLLA and fully embedded within an arterial wall. A volume of tissue surrounding the scaffold that undergoes cellular and extracellular remodeling post-implantation was represented as a distinct region with time-varying transport properties throughout the initial phases of erosion. PLLA degradation internal to the scaffold was modeled as a reaction-diffusion system, and transport of lactic acid (LA) external to the scaffold was modeled as a reaction-convection-diffusion system coupled with equations governing luminal blood flow. Parametric studies were performed to quantify how local peak LA concentrations in tissue vary with PLLA degradation rate, temporal changes in LA transport properties due to tissue remodeling, and LA metabolism rate. Model predictions indicate that the relative rates of tissue remodeling and polymer degradation modulate LA transport and suggest that a synchrony of these processes can minimize transient LA concentrations in tissue. Results further indicate that LA metabolism does not dramatically affect tissue concentrations and is an insignificant clearance mechanism relative to convective and diffusive transport. These observations add to our understanding of the means by which BVS degradation products are processed physiologically and the factors that may influence biological response to BVS therapy for coronary artery disease.

2.3 Methods

A three-dimensional computational model exploiting symmetric vessel characteristics was constructed based on the geometric and compositional characteristics of a representative bioresorbable vascular scaffold (BVS) (Abbott Vascular, Santa Clara, CA). The BVS implant is manufactured primarily from poly(L-lactide) (PLLA) and consequently yields lactic acid (LA) as a late degradation by-product. A two-dimensional

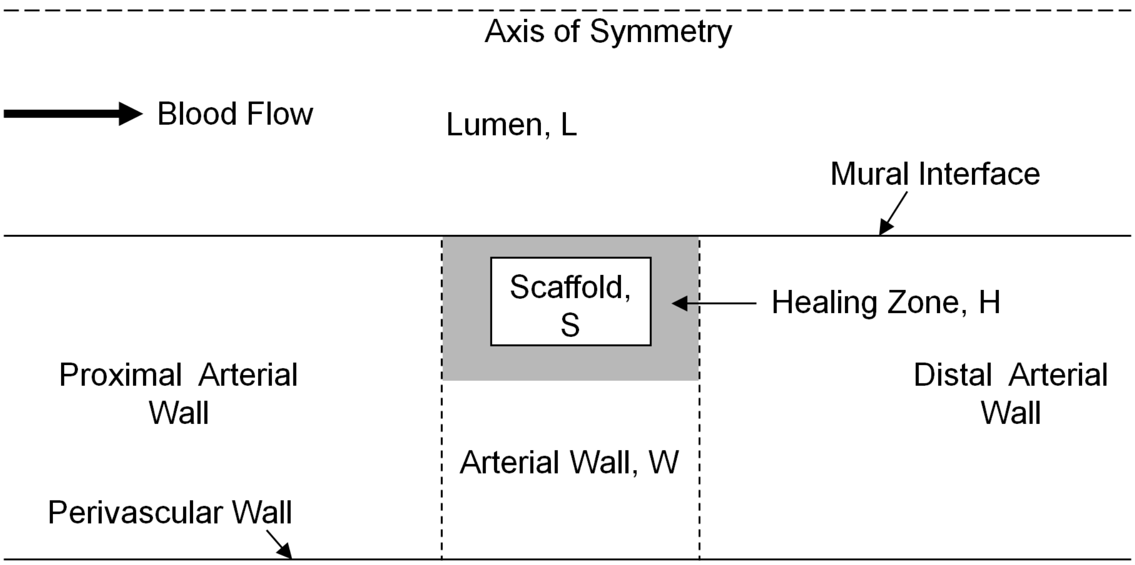

Figure 2.1 Schematic of the two-dimensional computational domain comprising a longitudinal scaffold segment (S) fully embedded within the arterial wall (W), a tissue healing zone (H) that undergoes marked changes in transport properties post-implantation, and the arterial lumen (L) (not to scale).

schematic of the computational domain utilized in this study depicts four geometric sub-domains: a longitudinal scaffold segment fully embedded within the arterial wall (S), a tissue healing zone (H) with transient transport properties at early implantation times, the remaining portion of the arterial wall (W), and the arterial lumen (L) (Figure 2.1). A three-dimensional geometry reflecting these sub-domains was constructed using SolidWorks (Dassault Systèmes) [45], where the diameter and length of the lumen were and respectively, and the thickness of the healing zone and arterial wall were and respectively (Figure 2.2A)

Blood was considered as an incompressible, Newtonian fluid, and its flow through the lumen was assumed to be steady, laminar, and fully developed. Luminal flow was described by the momentum and continuity equations as follows:

$$\rho_L \left(\mathbf{u_L} \cdot \nabla\right) \mathbf{u_L} = -\nabla P_L + \mu_L \nabla^2 \mathbf{u_L} \tag{2.1}$$

$$\nabla \cdot \mathbf{u_L} = 0, \tag{2.2}$$

where $\mathbf{u_L}$, $\rho_L = 1060$ kg m^{-3}, $\mu_L = 3.5 \times 10^{-3}$ Pa-s, and P_L are respectively blood velocity, blood density, blood viscosity, and pressure within the luminal region.

Blood flow through both the porous arterial wall and healing zone were modeled using momentum and continuity equations:

$$\rho_W \left(\mathbf{u_W} \cdot \nabla\right) \mathbf{u_W} = -\nabla P_W + (\frac{1}{\epsilon_W})\mu_W \nabla^2 \mathbf{u_W} - (\frac{\mu_W}{\kappa_W})\mathbf{u_W} \tag{2.3}$$

$$\nabla \cdot \mathbf{u_W} = 0 \tag{2.4}$$

$$\rho_H \left(\mathbf{u_H} \cdot \nabla\right) \mathbf{u_H} = -\nabla P_H + (\frac{1}{\epsilon_H})\mu_H \nabla^2 \mathbf{u_H} - (\frac{\mu_H}{\kappa_H})\mathbf{u_H} \tag{2.5}$$

$$\nabla \cdot \mathbf{u_H} = 0, \tag{2.6}$$

where $\mathbf{u_W}$, $\rho_W = 1050$ kg m^{-3}, $\mu_W = 7.2 \times 10^{-4}$ Pa-s, P_W, $\kappa_W = 1.43 \times 10^{-18}\ m^2$, and $\epsilon_W = 0.43$ are respectively steady-state velocity, density, viscosity, pressure, Darcy's

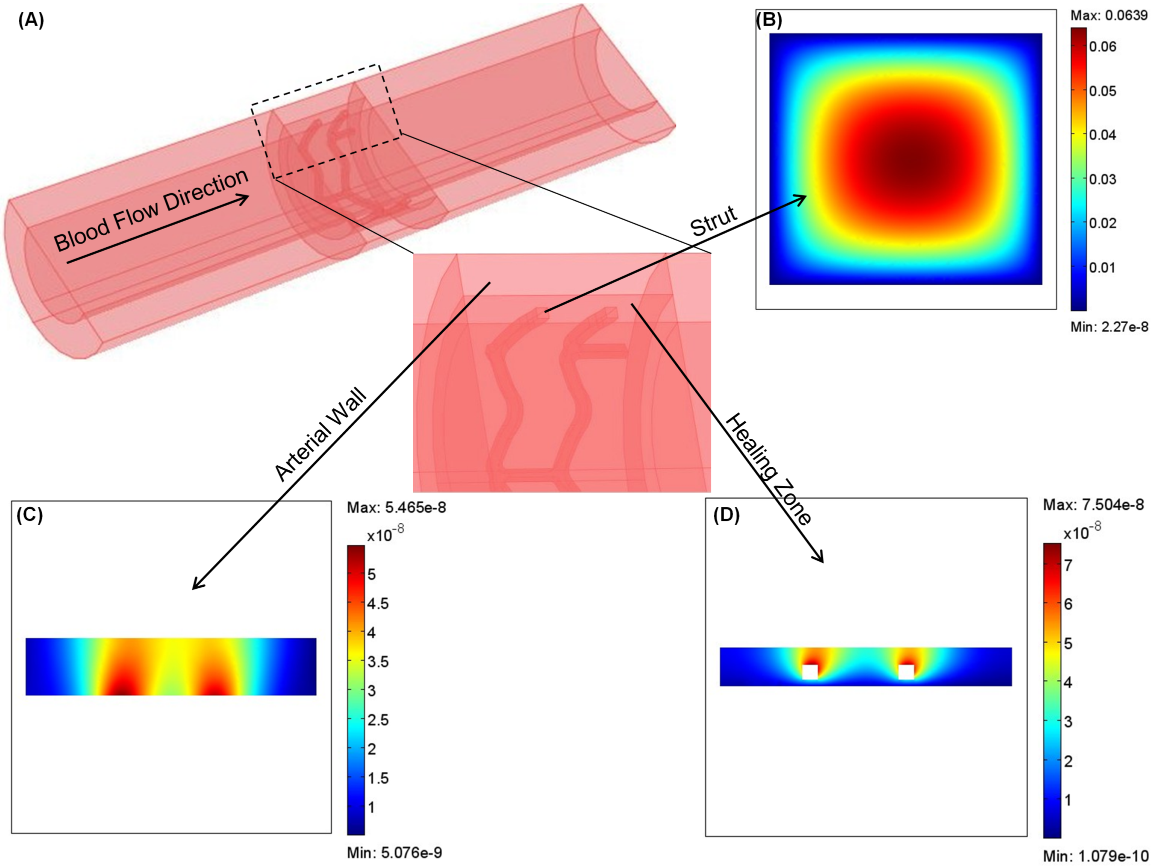

Figure 2.2 **(A)** Three-dimensional computational model of a fully-erodible scaffold residing in the arterial wall. Blood is flowing in the lumen and the porous arterial wall. Insets show high magnification images of the strut (S), arterial wall (W), and healing zone (H). **(B)** Lactic acid concentration is maximal at the scaffold core and diminishes towards the boundary with the healing zone. **(C, D)** Lactic acid released from the scaffold is transported through H and W via diffusion and convection. Lactic acid concentration is highest near the scaffold surface and reduces towards the perivascular wall. Hydrolytic degradation rate of $1 \times 10^{-7}\ s^{-1}$, lactic acid healing zone diffusivity change rate of $1 \times 10^{-7}\ s^{-1}$, and lactic acid metabolism rate of $1 \times 10^{-6}\ s^{-1}$ were used in depicted simulation results. Color bars represent lactic acid concentration for each inset.

permeability, and porosity characterizing interstitial blood plasma flow in the arterial wall; $\mathbf{u_H}$, $\rho_H = 1025$ kg m^{-3}, $\mu_H = 7.2 \times 10^{-4}$ Pa-s, P_H, $\kappa_H = 1.43 \times 10^{-18}\ m^2$, and $\epsilon_H = 0.43$ are respectively the steady-state velocity, density, viscosity, pressure, Darcy's permeability, and porosity characterizing interstitial blood plasma flow in the healing zone [82].

PLLA degradation was described by a reaction-diffusion model that considers autocatalyzed hydrolytic reactions. A simplified first-order degradation model was constructed based on the following reactions [22, 94]:

$$S_1 \overset{K}{\to} n_2 S_2 \overset{K}{\to} n_3 S_3 \overset{K}{\to} n_4 S_4 \overset{K}{\to} n_5 S_5, \tag{2.7}$$

where S_i, n_i, and K are respectively polymer species $i (i = 1, 2, 3, 4, 5)$, the stoichiometric coefficient of species i, and the effective PLLA hydrolytic degradation rate that describes the conversion between molecular species. Initial polymer monodispersity was assumed in all simulations, implying the presence of a single high molecular weight (100 kDa) species prior to scaffold degradation. Although complete PLLA degradation would actually yield numerous distinct oligomers, the degradation process was modeled as a systematic evolution of four oligomers groups ($S_1 - S_4$) and eventually LA (S_5). These five species constituted a reduced representation of transient scaffold composition throughout the degradation and resorption processes (Table 2.1).

Autocatalysis caused by the formation of acid end-groups through each hydrolysis reaction was assumed to occur only within the scaffold. Oligomers in excess of the PLLA solubility limit ($S_1 - S_4$) were assumed to be static within the scaffold for all times, with only diffusion and transient release of LA (S_5) into the surrounding tissue

Table 2.1 Range and average molecular weight of different species used to describe the degradation process of a fully erodible PLLA endovascular scaffold.

Species	Concentration (M)	M_w range (kDa)	Average M_w (kDa)
S_1	C_1	$80 \leq M_w < 120$	100
S_2	C_2	$40 \leq M_w < 80$	60
S_3	C_3	$10 \leq M_w < 40$	25
S_4	C_4	$0.1 \leq M_w < 10$	5
S_5	C_5	$0.1 \leq M_w$	0.1

[92]. Transient reaction-diffusion equations in the scaffold were considered as follows:

$$\frac{\partial C_l^S}{\partial t} = -KC_1 - K_a C_1 \sqrt{C_5} \tag{2.8}$$

$$\frac{\partial C_2^S}{\partial t} = n_2 K C_1 + n_2 K_a C_1 \sqrt{C_5} - KC_2 - K_a C_2 \sqrt{C_5} \tag{2.9}$$

$$\frac{\partial C_3^S}{\partial t} = \frac{n_3}{n_2} K C_2 + \frac{n_3}{n_2} K_a C_2 \sqrt{C_5} - KC_3 - K_a C_3 \sqrt{C_5} \tag{2.10}$$

$$\frac{\partial C_4^S}{\partial t} = \frac{n_4}{n_3} K C_3 + \frac{n_4}{n_3} K_a C_3 \sqrt{C_5} - KC_4 - K_a C_4 \sqrt{C_5} \tag{2.11}$$

$$\frac{\partial C_5^S}{\partial t} = \nabla \cdot (D_{C_5}^S \nabla C_5^S) + \frac{n_5}{n_4} K C_4 + \frac{n_5}{n_4} K_a C_4 \sqrt{C_5}, \tag{2.12}$$

where $C_1 - C_5$, $D_{C_5}^S = 10^{-15}\ m^2 s^{-1}$, and $K_a = 7.5 \times 10^{-8} \sqrt{molm^{-3} s^{-1}}$ are respectively the concentration of chemical species $S_1 - S_5$, the LA diffusion coefficient within the scaffold, and the autocatalytic degradation rate constant [31].

The metabolism of LA in both the healing zone and the arterial wall was modeled as a first-order reaction [43]. LA concentration inside the healing zone was modeled as transient reaction-diffusion-convection process:

$$\frac{\partial C_5^H}{\partial t} + \mathbf{u_H} \cdot \nabla C_5^H = \nabla \cdot (D_{C_5}^H \nabla C_5^H) - K_{m,H} C_5^H, \tag{2.13}$$

where $D_{C_5}^S$ and $K_{m,H}$ are respectively LA diffusion coefficient and metabolism rate within the healing zone [56]. $D_{C_5}^S$ was modeled as an exponentially decaying transport property with an initial maximum value equal to the LA diffusion coefficient in the lumen ($D_{C_5}^L = 10^{-8}\ m^2 s^{-1}$) and a minimum value that is equal to the LA diffusion coefficient in the arterial wall ($D_{C_5}^W = 10^{-12}\ m^2 s^{-1}$). The transient value of $D_{C_5}^S$ was modeled as follows:

$$D_{C_5}^H - D_{C_5}^W = (D_{C_5}^L - D_{C_5}^W) e^{-\alpha t}, \tag{2.14}$$

where α is the exponential constant that describes the transformation from blood-like to arterial-wall like behavior. LA concentration within the arterial wall was also modeled as a transient reaction-diffusion-convection process as follows:

$$\frac{\partial C_5^W}{\partial t} + \mathbf{u_W} \cdot \nabla C_5^W = \nabla \cdot (D_{C_5}^W \nabla C_5^W) - K_{m,W} C_5^W, \tag{2.15}$$

where $K_{m,W}$ is LA metabolism rate in the arterial wall. LA transport within the lumen was modeled as transient diffusion-convection process as follows:

$$\frac{\partial C_5^L}{\partial t} + \mathbf{u_L} \cdot \nabla C_5^L = \nabla \cdot (D_{C_5}^L \nabla C_5^L), \tag{2.16}$$

A fully developed, parabolic velocity profile with a mean velocity of 0.265 $m\ s^{-1}$ was assumed at the luminal inlet [45]. A transmural velocity boundary condition was imposed in the normal direction of the mural interface on the basis of Kedem-Katchalsky equation [41], whereas a constant pressure boundary condition was imposed on the perivascular wall [81]. Symmetry boundary conditions were assigned both at the arterial wall inlet and outlet, and along the vessel center-line.

For species evolution and transport, S_1 with unit concentration was the initially imposed within the scaffold sub-domain. Flux continuity of the mobile species S_5 was maintained at the scaffold surface, healing zone-arterial wall interface, and the mural interface, while a convective flux boundary condition was also imposed at the perivascular wall. A zero-concentration condition was assumed at the lumen inlet, as upstream species transport is largely prevented by luminal flow [7, 15]. Conversely, downstream species transport is flow-assisted and assumed to be a convection-dominated process, motivating the use of a convective flux boundary condition at the lumen outlet [95].

The computational domain was meshed using 102,845 tetrahedral elements, with a relative tolerance of 10^{-5} required for solution convergence. An adaptive meshing procedure was used to create a continuous mesh with maximum density at the scaffold surface and minimum density along the center-line of the lumen, facilitating high fidelity results in the tissue regions of interest. The finite-element framework (COMSOL Multiphysics^{TM}) yielded a mesh-independent solution that was defined as a less than 0.1% relative change in C_1 within the scaffold at 24 months following successive adaptive refinements.

2.4 Results

Our computational model provided converged solutions for the spatial and temporal distribution of BVS by-products over a wide range of kinetic parameters characterizing PLLA degradation, arterial remodeling, lactic acid (LA) transport, and metabolism. The spatial distribution of LA within the scaffold was maximal at the core and decreased towards the boundary with the healing zone for all times, confirming diffusion-mediated LA transport within the scaffold sub-domain (Figure 2.2B). However, a substantial amount of LA was transported by transmural convection both in the healing zone and the arterial wall, evidenced by a greater increase in LA concentration in the radial as opposed to axial direction within both sub-domains (Figures 2.2C & D). These trends are a consequence of the simulated average transmural blood velocity ($1.64 \times 10^{-8}\ m\ s^{-1}$), which is consistent with the previously reported experimental results attained within rabbit aortic walls ($1.78 \times 10^{-8}\ m\ s^{-1}$) [54]. Moreover, the LA concentration was evidently higher in the distal compared to proximal region of both the scaffold and healing zone, indicating that blood flow affects transport in these sub-domains.

The simulated autocatalytic degradation process resulted in a nonlinear decrease of the number-averaged molecular weight (M_n) of the insoluble scaffold species post-implantation (Figure 2.3A). For a given set of parameters, our model predictions correlate well (R = 0.99, p <0.05) to in vivo measurements of BVS scaffold degradation [59],providing support for the employed degradation model and analyzed range of degradation rates. When the PLLA hydrolytic degradation rate (K) was 7.5×10^{-8} s^{-1}, the scaffold underwent a rapid reduction of M_n in first twelve months, followed

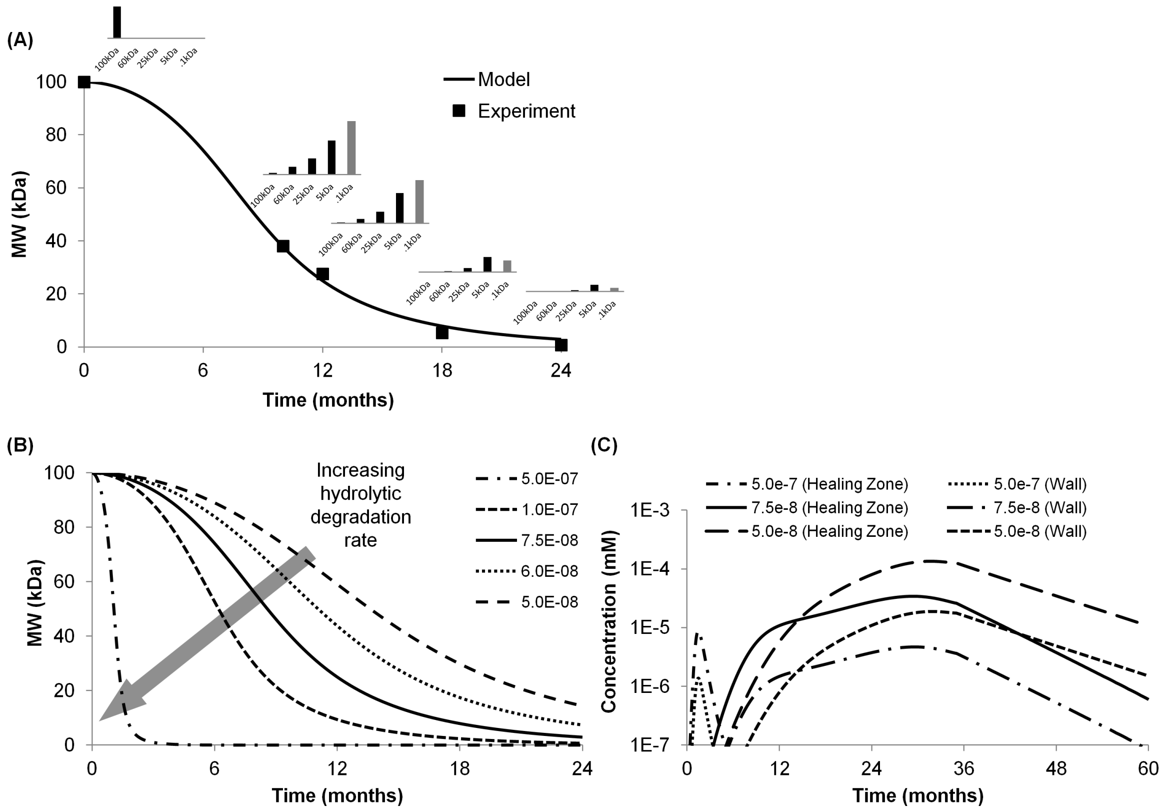

Figure 2.3 **(A)** Simulated number averaged molecular weight change of insoluble scaffold species (smooth line) as a function of implantation time agree with previously reported experimental measurements of BVS [59].Insets depict the relative concentration of the insoluble oligomer species (black bars) and soluble species (gray bars) within the scaffold domain throughout the degradation process. **(B)** The number averaged molecular weight of the scaffold as a function of time for various hydrolytic degradation rates. Increased hydrolytic degradation rate (K) leads to a markedly faster reduction in scaffold number-averaged molecular weight. **(C)** Lactic acid concentration within the healing zone and arterial wall over five years post-implantation for various hydrolytic degradation rates. At all times, the lactic acid concentration is approximately an order of magnitude greater in the healing zone compared to the arterial wall. A hydrolytic degradation rate of $7.5 \times 10^{-8}\ s^{-1}$ was used for **(A)**. A lactic acid healing zone diffusivity change rate of $1 \times 10^{-7}\ s^{-1}$ and lactic acid metabolism rate of $1 \times 10^{-6}\ s^{-1}$ were used in all illustrated simulation results **(A-C)**.

by period of gradual decline to approximately 3% of the initial value after two years. Transient scaffold molecular distributions (insets in Figure 2.3A) demonstrate that defined chemical species groups are present in various concentrations through the degradation process, with a relatively high concentration of LA within the scaffold at early times (<12 months post implantation). Early accumulation of LA within the scaffold implies that the generation rate exceeds the diffusion-mediated transport rate, a phenomena that is in agreement with previously reported computational results [67].

An order of magnitude variation in K dramatically affects scaffold M_n over a two-year period (Figure 2.3B). M_n is reduced by over 40% within one month under the fastest K ($7.5 \times 10^{-8}\ s^{-1}$), while an order of magnitude decrease in K results in less than 1% M_n reduction at the same time point. The significant model response to variation in K is an expected characteristic of autocatalytic polymers such as PLLA, where trace levels of LA within the material can substantially accelerate degradation.

The transient LA concentration within the scaffold is consistently orders of magnitude greater than that in the lumen or surrounding arterial wall, suggesting that the arterial environment behaves as a sink for evolved by-products. The healing zone is a predefined region of arterial tissue (10% of arterial wall thickness) surrounding the scaffold that is postulated to undergo changes in transport properties as a consequence of tissue remodeling. As a consequence of proximity to the scaffold, LA concentrations are consistently higher in the healing zone than in the arterial wall (Figure 2.3C), implying that local tissue is at a greatest risk of by-product accumulation despite initially accelerated transport associated with incomplete healing. Transient LA concentrations within the healing zone and the arterial wall follow similar trends for a prescribed hydrolytic degradation rate (K). However, a strong dependence of the time course and nature of these trends on K is observed. Under the fastest K ($5 \times 10^{-7}\ s^{-1}$), LA concentration sharply increases over the first month, but is essentially cleared by one year. For intermediate K , there is a moderately sharp increase in LA concentration over the first ten months followed by a period

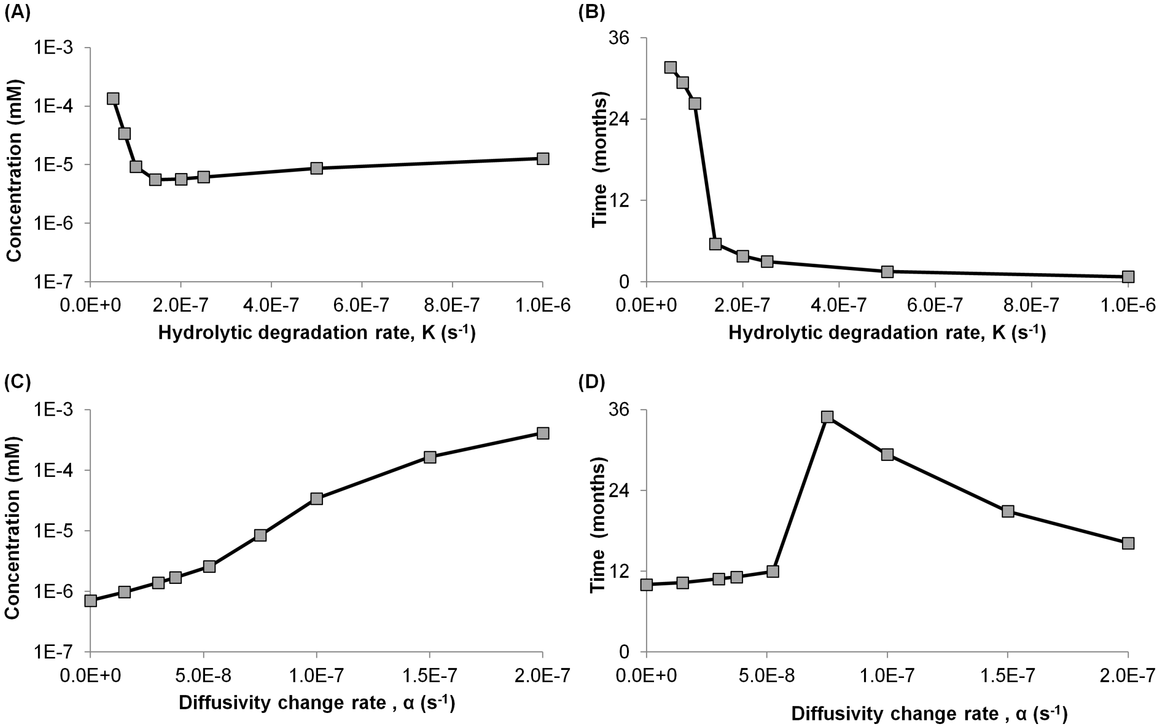

Figure 2.4 **(A-B)** Hydrolytic degradation rate (K) modulated both peak lactic acid concentration within the healing zone (Cmax) and the time after implantation (tmax) at which that concentration occurred. Dependence of C_{max} on K follows U-shaped kinetics, whereas t_{max} monotonically decreases with K. **(C-D)** Lactic acid concentration within the healing zone and arterial wall over five years post-implantation for various hydrolytic degradation rates. At all times, the lactic acid concentration is approximately an order of magnitude greater in the healing zone compared to the arterial wall.

of sustained concentration that persists until approximately 29 months. When K is lowest ($5 \times 10^{-8}\ s^{-1}$), a gradual increase of LA concentration occurs over a period of 32 months followed by a protracted decline thereafter.

The peak concentration of LA within the healing zone (C_{max}) varied nonlinearly with K (Figure 2.4A). Trends indicate that C_{max} initially has a strong negative dependence on K until a critical limit is surpassed. At K exceeding $1.4 \times 10^{-7}\ s^{-1}$, faster degradation results in slightly greater LA accumulation within local tissue. The time point at which C_{max} occurs (t_{max}) is monotonically reduced with faster

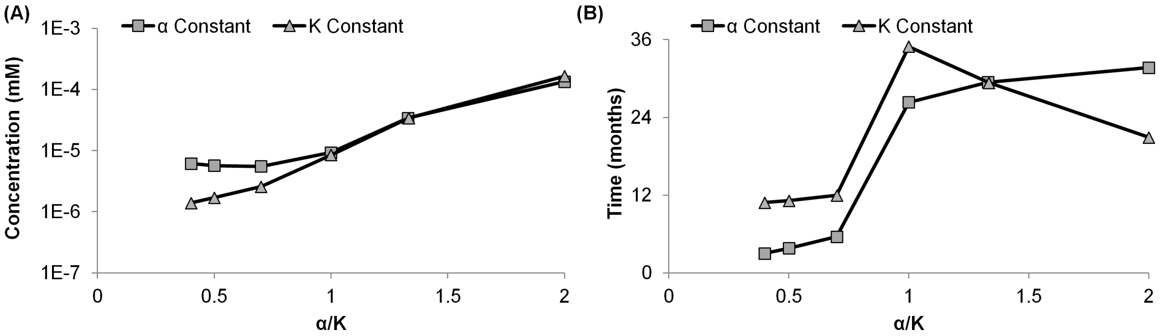

Figure 2.5 The ratio of the diffusivity change rate within the healing zone (α) to the hydrolytic degradation rate of the scaffold (K) was varied between 0.2 and 2 by altering either rate constant in isolation. **(A)** The peak lactic acid concentration within the healing zone (C_{max}) generally had a positive dependence on $\frac{\alpha}{K}$ regardless of which rate was varied. **(B)** The time at which C_{max} occurs (t_{max}) showed a near binary dependence on $\frac{\alpha}{K}$. When $\frac{\alpha}{K}$ <1, t_{max} was less than 12 months for all tested cases; when $\frac{\alpha}{K}$ >1, t_{max} was comparatively longer (21 - 35 months).

degradation, and abruptly drops from over two years to less than six months post-implantation when K approaches the critical limit of $1.4 \times 10^{-7}\ s^{-1}$ (Figure 2.4B). The temporal change in LA diffusivity within the healing zone reflects the transition from lumen-like to arterial wall-like transport properties as local tissue is remodeled. An increase in the exponential rate constant governing diffusivity (α) leads to a higher C_{max}, implying that transient transport properties adjacent to a scaffold can influence LA accumulation (Figure 2.4C). The values for t_{max} are nearly constant for $\alpha < 5.25 \times 10^{-8}\ s^{-1}$, suggesting that clearance within this regime is not limited by transport through the healing zone (Figure 2.4D). However, a more complex dependence is observed when $\alpha \geq 7.5 \times 10^{-8}\ s^{-1}$, as peak LA levels are not only orders of magnitude higher as compared to lower rates, but also occur at substantially later times post-implantation.

The relative rates of transport property change within the healing zone and PLLA hydrolytic degradation ($\frac{\alpha}{K}$) show bi-modal governance of C_{max} (Figure 2.5A). When $\frac{\alpha}{K}$ <1, the resultant C_{max} is always less than the value observed when $\frac{\alpha}{K} = 1$. Con-

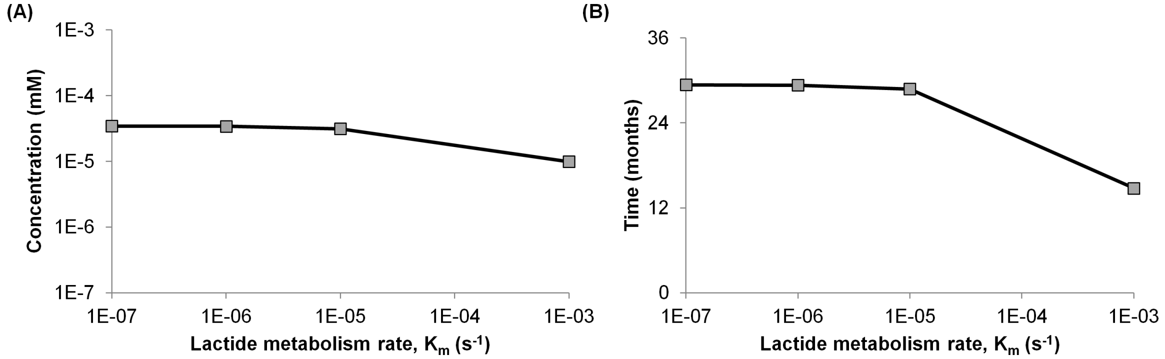

Figure 2.6 Metabolism of lactic acid is a secondary clearance mechanism from tissue as compared to convective/diffusive transport. **(A-B)** The peak lactic acid concentration within the healing zone (C_{max}) and the time at which C_{max} occurs (t_{max}) were largely independent of metabolism rate (K_m), with an effect observed only at the maximal simulated rate (K_m) $= 1 \times 10^{-3}\ s^{-1}$.

versely, when $\frac{\alpha}{K}$ >1, C_{max} is comparatively elevated. These trends suggest that LA is most effectively cleared from local tissue when the rate of scaffold degradation is greater than the rate of conversion from a lumen-like to an arterial wall-like domain. The operative $\frac{\alpha}{K}$ also modulates t_{max}, although in a less uniform manner (Figure 2.5B). In general, $\frac{\alpha}{K}$ <1 results in the peak concentrations occurring at earlier times post-implantation, while $\frac{\alpha}{K}$ >1 leads to relatively greater t_{max}.

In all simulations, LA metabolism rates within the healing zone ($K_{m,H}$) and arterial wall ($K_{m,W}$) were set to equal values ($K_{m,W} = K_{m,H} = K_m$). Two order of magnitude variations in K_m $1 \times 10^{-7}\ s^{-1}$ - $1 \times 10^{-5}\ s^{-1}$ had an insignificant effect on both the resultant C_{max} and t_{max} (Figure 2.6A & B). Only an extreme metabolic rate of $1 \times 10^{-3}\ s^{-1}$ influenced transient LA levels in local tissue, with approximately a 70% reduction in C_{max} compared to lower rates.

2.5 DISCUSSION

The ultimate fate of implant-derived chemical species is subject to a complex array of factors that often preclude delineation through traditional experimentation. Even when carefully designed bench-top experiments provide characterizations of material degradation and erosion, results do not always reflect *in vivo* performance. Prediction of implant behavior and degraded species fate *in vivo* is confounded by variations in governing processes such as species generation/release rates, diffusive/convective transport, and metabolism, all of which are subject to change based on precise implantation site, implant composition and properties, and patient status. While fully bioresorbable vascular scaffolds (BVS) have the potential to improve upon current treatment options for ischemic artery disease, we must understand the numerous factors that will dictate device safety and efficacy. Complete scaffold erosion could potentially mitigate long-term risks that limit permanent alternatives, but also introduces new concerns with injurious by-product accumulation in local arterial tissue.

It is critical to account for the transient levels of LA that accumulate in local tissue throughout the implant lifetime to predict the safety of BVS composed of PLLA. Convective and diffusive transport coupled with metabolic elimination governs naturally fluctuating LA tissue levels in normal physiologic scenarios. While the same clearance mechanisms would be operative following scaffold implantation, high transient LA concentrations could arise in local tissue during the erosion process and create an acidic environment [90]. BVS evaluation, both in terms of functional performance and safety, requires extensive *in vivo* studies that measure LA generation, release, and concentration in tissue over the implant lifetime - these experiments are conducted at high cost and on the timescale of years. Computational modeling offers an efficient and complementary framework for critical implant assessment and facilitates both understanding and prediction of BVS behavior.

In an intriguing fashion, our results predict that the kinetic rates of PLLA hydrolysis (K) and the local change in arterial diffusivity associated with tissue remodeling

(α) dominate over metabolism (K_m) in determining the peak local tissue LA concentrations (C_{max}). Degradation kinetics modulated C_{max} in a complex fashion, with a trend inflection observed at an intermediate rate within the analyzed parametric space (Figure 2.4A). The trend results from an interplay between polymer degradation and arterial healing rates, which is further revealed upon direct analyses of the dimensionless constant $\frac{\alpha}{K}$ (Figure 2.5A). LA clearance from local tissue is favored at low $\frac{\alpha}{K}$, where degradation dominates and is far faster than the reduction in transport associated with healing. The rate of transformation of local tissue from a temporary clot immediately following implantation (lumen-like) to a stable cellularized substrate (arterial wall-like) therefore cannot be overlooked when changes in the material structure and arterial transport properties are on similar timescales. Synchrony between the degradation and healing processes emerges as a design guideline that can be applied to BVS, but obviously must be balanced against the need for physical persistence of the scaffold at the implantation site in order to achieve the therapeutic effect [1, 11].

Our simulations predict that extreme variations in LA metabolism will have a negligible effect on local tissue concentrations, suggesting that convective and diffusive transport are the primary clearance mechanisms within the arterial environment (Figure 2.6A. Because scaffold lifetime is presumably independent of LA metabolism within the tissue, our results imply that patient-specific variations in metabolic activity can largely be ignored in designing BVS prototypes for clinical use. Conversely, the change in LA transport that accompanies tissue transformation is a strong determinant of scaffold safety that may implicate more application-specific variation driven by deployment protocols and operator techniques.

2.6 Study Limitations and Future Works

As with most computational studies, results and drawn inferences become all the more valuable when coupled with experimental and/or clinical data. Previous studies provided qualitative assessment of the transient tissue response following BVS implantation in the pig coronary artery [59]. Based on these studies, we were able to assume reasonable spatial dimensions for the simulated healing zone and confidently treat this region as being geometrically stable throughout the simulation time. However, there is no reported study of chemical species transport properties within the arterial wall and over time. In our model, we assumed that healing zone transport properties would transition from blood-like to arterial-wall like in a manner that is independent of local physiological factors. This not necessarily the case *in vivo* - local LA concentration could potentially impact tissue remodeling and thus transient transport properties. In lieu of definitive experimental data, our approach was to conduct parametric analyses to predict how the kinetics of local tissue transformation will modulate LA transport and accumulation. Due to the multitude of simulated physicochemical processes, technical challenges in related experiments, and long simulated time periods ($\sim$ 5 years), some model assumptions related to the healing zone preclude experimental validation and should be carefully considered when interpreting computational results.

While important in modeling flow-mediated transport in the arterial lumen, previous studies suggest that blood pulsatility minimally influences the chemical species transport within the arterial wall [95, 45]. Histology of the main coronary artery of pigs following implantation of BVS indicates that scaffolds are fully-covered by a fibromuscular neointima after only 28 days [59]. As this time period represents just an early stage of the developed computational model (60 months), we treated the scaffold as a fully embedded implant through the entire simulation time and discarded the pulsatile nature of luminal flow. Nevertheless, our developed framework paves way for future studies that account for various levels of scaffold embedding and/or blood pulsatility.

Although able to match experimental data for a given set of parameters (Figure 2.3A), our PLLA degradation model featured a limited number of oligomer/monomer species generated through abbreviated degradation steps governed by a single rate constant. Scaffold degradation could be more accurately modeled with either (i) a probabilistic modifier of the degradation rate constant to describe chain scission from a longer chain into multiple smaller chains or (ii) a stochastic model governed by the intrinsic degradation rate constant that allows for generation of all possible oligomers throughout the degradation process. Moreover, we assumed that the scaffold was initially a monodisperse polymer matrix with a normalized concentration of the single species. In the tissue domains, lactic acid metabolism was modeled as a single-step process governed by a single rate K_m, even though the actual metabolic pathway is considerably more complex. The assumptions driving the employed degradation and metabolism models enable management of computational cost and facilitate parametric analyses of multiple key processes.

Future work should include more realistic models of degradation and increasingly be based on system-specific experimental data. Because of our model assumptions, the reported by-product concentrations cannot be directly used to predict clinical safety, but instead enable elucidation of deterministic processes and relationships among various kinetic parameters. While limitations and assumptions must be taken into account, computational modeling provides a cost-effective approach to gain new insight on the interplay between tissue remodeling, polymer degradation, and metabolic clearance in determining by-product retention and distribution within arterial tissue.

2.7 CONCLUSION

Our study suggests that tissue remodeling and polymer degradation kinetics modulate lactic acid (LA) accumulation within adjacent arterial tissue in the case of a tissue-embedded, fully bioresorbable vascular scaffold (BVS) comprised of PLLA. On the other hand, peak LA concentrations were insensitive to large variation in the tissue metabolic rate, suggesting that metabolism is a secondary by-product clearance mechanism compared to diffusive and convective transport. Synchrony between rates of remodeling and degradation is predicted to minimize peak LA levels in local tissue over the scaffold lifetime. As BVS are increasingly considered for the treatment of coronary artery disease, insights on the production and tissue retention of degradation by-products can help predict clinical performance and provide a basis for iterative device design.

Chapter 3

IMPACT OF POLYMER STRUCTURE AND COMPOSITION ON FULLY-RESORBABLE ENDOVASCULAR SCAFFOLD PERFORMANCE

[1]

3.1 Abstract

Fully-erodible endovascular scaffolds are increasingly considered for the treatment of obstructive arterial disease owing to their potential to mitigate long-term risks associated with permanent alternatives. While complete scaffold erosion facilitates vessel healing, generation and release of material degradation by-products from candidate materials such as poly-L-lactide (PLLA) may elicit local inflammatory responses that limit implant efficacy. We developed a computational framework to quantify how the compositional and structural parameters of PLLA-based fully-erodible endovascular scaffolds affect degradation kinetics, erosion kinetics, and the transient accumulation of material by-products within the arterial wall. Parametric studies reveal that while some material properties have similar effects on these critical processes, others induce qualitatively opposing responses. For example, scaffold degradation is only mildly responsive to changes in either PLLA polydispersity or the initial degree of crystallinity, while erosion kinetics are comparatively sensitive to crystallinity. More-

---

[1] Ferdous, J., Kolachalama V. B., and Shazly T. 2013. *Acta Biomaterialia.* 9(4): 6052-6061. Reprinted here with permission of publisher.

over, lactide doping can effectively tune both scaffold degradation and erosion, but a concomitant increase in local by-product accumulation raises concerns about implant safety. Optimized erodible endovascular scaffolds must precisely balance therapeutic function and biological response over the implant lifetime, where compositional and structural parameters will have differential effects on implant performance.

3.2 Introduction

Poly-L-lactide (PLLA) is a bioresorbable polymer considered for multiple clinical applications due to generally acceptable biocompatibility and tunable physicochemical properties [80, 5]. PLLA is currently used in the fabrication of resorbable sutures, wound healing scaffolds, orthopedic fixation devices, and controlled drug/gene delivery systems [47, 55, 57]. Resorbable endovascular scaffolds composed primarily of PLLA have been recently proposed as an alternative to permanent metallic devices [58]. Like traditional stents, resorbable scaffolds can provide sufficient structural support to prevent acute vessel re-narrowing and serve as a platform for the controlled release of anti-proliferative or anti-inflammatory drugs. Additionally, resorbable scaffolds have the inherent potential to reduce the occurrence of untoward events such as vessel re-narrowing or thrombosis by virtue of undergoing complete resorption over a period of two to three years following implantation [59, 58].

Following deployment, endovascular implants are gradually embedded within tissue due to fiber capsule formation and vessel remodeling over the course of approximately four weeks [59]. In the case of fully-erodible PLLA scaffolds that degrade *in vivo* over much longer periods, a significant portion of the erosion process will occur while the implant is in a tissue-embedded state. Embedding will promote local accumulation of implant-derived soluble by-products, thereby increasing the risk of inflammatory or immune responses. Risks associated with by-product accumulation can detract from the benefits of complete resorption for vascular repair, and motivate comprehensive assessment of how material design parameters impact polymer degradation and erosion in the arterial environment.

PLLA degrades via an autocatalytic hydrolysis reaction, where an irreversible ester bond scission process creates oligomers and ultimately lactic acid (LA) [25, 9]. Though LA and the readily deprotonated anion L-lactate are common by-products of the Krebs cycle, excessive concentrations in arterial tissue could alter the local pH and induce toxicity. Bulk erosion of PLLA scaffolds occurs via diffusion of soluble degradation by-products out of the material network and into the surrounding medium, resulting in a near homogenous mass loss [76, 71]. A complex combination of factors governing scaffold degradation, generated by-product transport, and metabolism will determine the transient LA concentrations in arterial tissue. Previous studies suggest that scaffold-derived by-product clearance from local arterial tissue is dominated by transport as opposed to metabolic processes, and that environmental factors such as the properties of arterial wall and the extent of tissue-embedding significantly impact the peak LA concentration over the implant lifetime [75]. While environmental properties and tissue-embedding kinetics vary among individuals, several intrinsic PLLA properties can be altered in the scaffold manufacturing process and tuned to control degradation and erosion.

Although several studies characterize the generation, release, and transport of PLLA degradation by-products in various environments [94, 85, 90], the physical and chemical factors that influence transient LA concentrations in arterial tissue are difficult to independently assess with conventional experimental techniques. Degradation and erosion processes are not only affected by initial scaffold characteristics, including molecular weight, polydispersity, crystallinity, presence of plasticizers, additives, and size, but also by the operating temperature, pH, blood flow rate, and enzymatic activity [2]. As compared to bench-top or *in vivo* studies, computational models can readily provide insight into how these factors independently or collectively impact scaffold performance *in situ* and insomuch provide design guidelines for scaffold development. To the best of our knowledge, no computational model has been reported which relates scaffold degradation and erosion kinetics under arterial flow conditions to material parameters that can be controlled in the manufacturing process, [25, 79, 4, 68, 96, 91, 3]. While our earlier work simulated the evolution and transport of soluble species both within the scaffold and arterial wall [97], we did not explore how material parameters impacted by-product fate, and these aspects have been the focus of the current study.

A two-dimensional computational model of a tissue-embedded PLLA scaffold was developed to characterize the effects of compositional and structural parameters on LA accumulation within the arterial wall. Degradation and erosion kinetics were quantified for 120 days from initial deployment using metrics such as reduction in scaffold weight-average molecular weight (M_w) and weight (W_t), respectively. Within the same period, transient LA tissue levels were quantified via a surface integral of the concentration field in the local arterial wall. Model predictions suggest that some material parameters have a similar effect on degradation and erosion processes, while others induce qualitatively opposing responses. Moreover, peak LA levels in surrounding tissue and the times at which these levels occur exhibit high sensitivity to scaffold molecular structure and the amount of lactide doping. PLLA composition and structure can be tuned to control both degradation and erosion processes, and ultimately mitigate the risk associated with by-product accumulation in endovascular scaffold applications.

3.3 Methods

A two-dimensional computational model of a tissue-embedded PLLA scaffold was developed with geometrical regions representing a single scaffold strut (S) fully embedded within the arterial wall (W), a segment of the arterial wall adjacent to the strut termed the critical zone (CZ), and the arterial lumen (L) (Figure 3.1A). The diameter and length of the lumen were $3 \times 10^{-3}\ m$ and $1 \times 10^{-2}\ m$, respectively, the thickness of the arterial wall was $1 \times 10^{-3}\ m$, the side-length of the square strut was $1 \times 10^{-4}\ m$, and width and thickness of the critical zone were $8 \times 10^{-4}\ m$ and $4 \times 10^{-4}\ m$, respectively. Blood was considered as an incompressible and Newtonian fluid. Blood flow through the lumen was assumed to be steady, laminar, and fully-developed, and was modeled using momentum and continuity equations as follows:

$$\rho_L \left(\mathbf{u_L} \cdot \nabla\right) \mathbf{u_L} = -\nabla P_L + \mu_L \nabla^2 \mathbf{u_L} \tag{3.1}$$

$$\nabla \cdot \mathbf{u_L} = 0 \tag{3.2}$$

where $\mathbf{u_L}$, $\rho_L = 1060$ kg m^{-3}, $\mu_L = 3.5 \times 10^{-3}$ Pa-s [75], and P_L are respectively luminal blood velocity, density, viscosity, and pressure.

Steady blood plasma flow through the porous arterial wall was modeled using momentum and continuity equations as follows:

$$\rho_W \left(\mathbf{u_W} \cdot \nabla\right) \mathbf{u_W} = -\nabla P_W + (\frac{1}{\epsilon_W})\mu_W \nabla^2 \mathbf{u_W} - (\frac{\mu_W}{\kappa_W})\mathbf{u_W} \tag{3.3}$$

$$\nabla \cdot \mathbf{u_W} = 0 \tag{3.4}$$

where $\mathbf{u_W}$, $\rho_W = 1025$ kg m^{-3}, $\mu_W = 7.2 \times 10^{-4}$ Pa-s, [75, 97] and P_W, are respectively transmural blood plasma velocity, density, viscosity, pressure, whereas, $\kappa_W = 1.43 \times 10^{-18}\ m^2$ and $\epsilon_W = 0.43$ [45, 45] are respectively Darcy's permeability and porosity of the arterial wall.

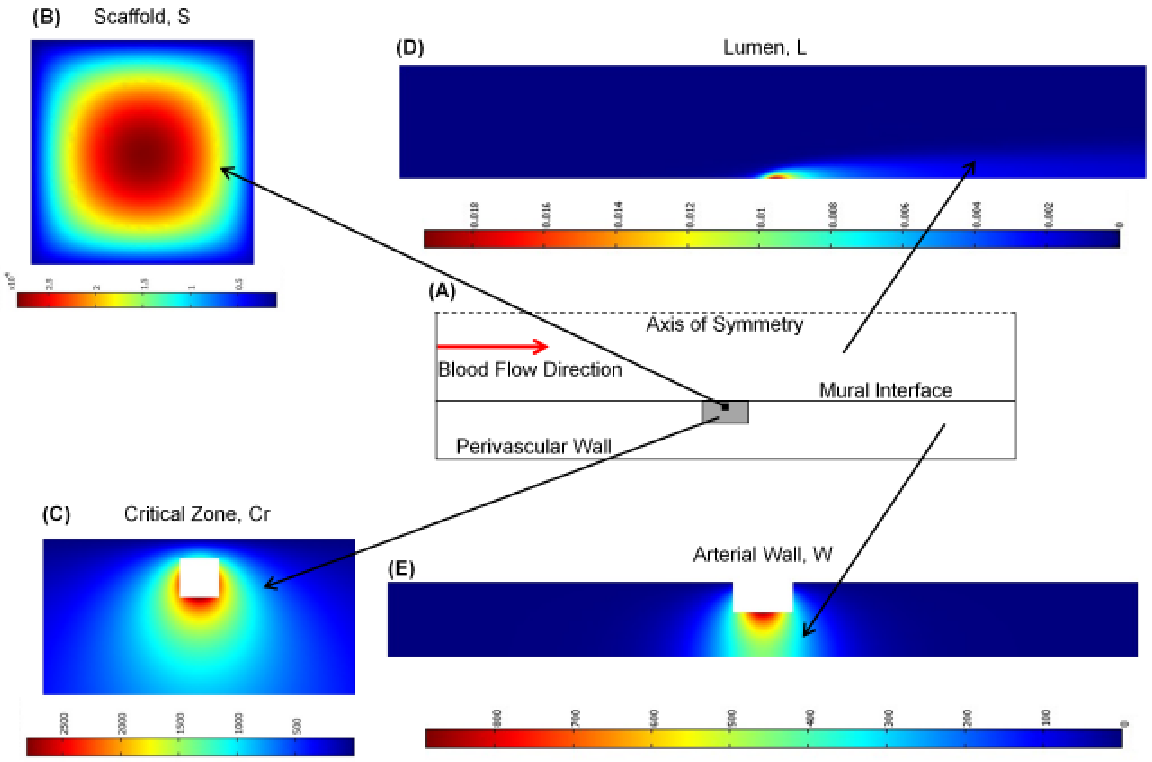

Figure 3.1 **(A)** Schematic of the two-dimensional computational framework consisting of a scaffold strut (S) fully-embedded within the arterial wall (W), a critical zone (Cr) in the arterial wall surrounding the scaffold, and the arterial lumen (L) (not to scale). Surface plots of LA concentration in the scaffold **(B)**, critical zone **(C)**, lumen **(D)**, and arterial wall **(E)** at 30 days post-implantation. Color bars represent LA concentration for each inset.

In the present study, degradation refers to a chain scission process where polymer chains are cleaved into oligomers and monomers, while erosion reflects material loss from the bulk polymer due to release of water soluble oligomers and monomers. Though PLLA can undergo both autocatalytic and un-catalytic reactions [92], only autocatalytic reaction was considered in this study as the scaffold was fully embedded in the arterial wall and water-soluble by-products were unlikely to be washed away immediately from the scaffold but they acted as catalysts that enhance further degradation. Further, the thickness of the scaffold was 0.1 mm, which was well below the critical thickness for surface erosion (0.2 - 0.3 mm) [28], suggesting that the scaffold underwent primarily bulk erosion.

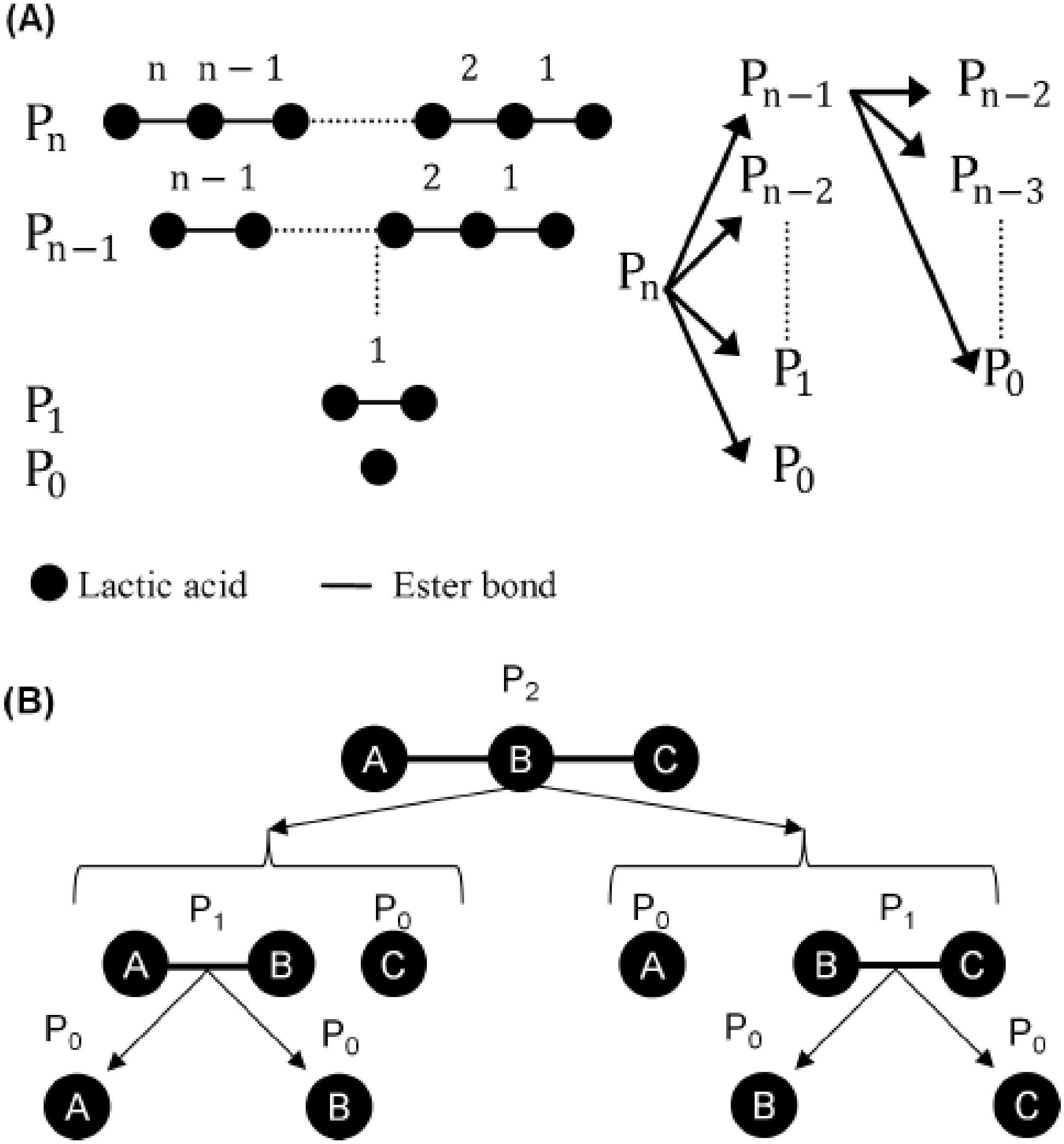

Figure 3.2 **(A)** Random scission of ester bond with equal probability. **(B)** Any constituent can randomly produces a specific daughter constituent in two ways or two molecules of a specific daughter constituent.

Each ester bond within constituent PLLA chains was assumed to undergo random scission with equal probability and generate two daughter oligomers of lower molecular weight [96, 4]. Hence, production of any specific constituents from a longer chain can randomly occur in two ways (Figure 3.2). Amorphous regions of the scaffold were subjected to degradation due to a favorable water penetration condition, while the crystalline polymer regions were considered stable [85, 30]. Initial and generated polymer chains with carboxylic acid end groups were assumed to catalyze subsequent degradation [4]. Moreover, polymeric constituents below the solubility limit (8° of polymerization) were assumed to undergo transient release from the scaffold into the surrounding medium [71]. Degradation of the longest constituent chain in the scaffold, P_n, is described by the following rate equation:

$$\frac{dC_n^S}{dt} = -nkC_n^S A \tag{3.5}$$

where n, C_n^S, k, and A are respectively the number of ester bonds, concentration of in the scaffold, hydrolytic degradation rate, and autocatalysis factor that accounts all constituents containing carboxylic acid end groups. The hydrolytic degradation rate was assumed to be equal irrespective of chain length.

$$\frac{dC_i^S}{dt} = -ikC_i^S A + 2 \sum_{m=i+1}^{n} kC_m^S A; 8 \leq i < n \tag{3.6}$$

where C_i^S is the insoluble constituent concentration; is number of ester bonds, and C_m^S is any insoluble constituents concentration with number of ester bonds between n and $i + 1$ in the scaffold The concentration and transport of scaffold constituents below the solubility limit were modeled by diffusion-reaction equations as follows:

$$\frac{\partial C_j^S}{\partial t} = \nabla \cdot (D_j^S \nabla C_5^S) - jkC_j^S A + 2 \sum_{m=j+1}^{n} kC_m^S A; 0 < j < n \tag{3.7}$$

where C_j^S and D_j^S are respectively the soluble constituent concentration and the diffusion coefficient, j is number of ester bonds, and C_m^S is any constituents concentration with number of ester bonds between n and $j + 1$ in the scaffold.

Monomer, LA (P_0) concentration within the scaffold was described as follows:

$$\frac{\partial C_0^S}{\partial t} = \nabla \cdot (D_0^S \nabla C_0^S) + 2 \sum_{m=1}^{n} k C_m^S A; 8 \leq i < n \tag{3.8}$$

where C_j^S and are D_j^S respectively LA concentration and diffusion coefficient, C_m^S is any constituents concentration with number of ester bonds between n and 1 in the scaffold. Polymer degradation increases the scaffold porosity and the diffusion coefficients of all mobile chains. Hence, the diffusion coefficients of soluble constituents at any time, D^t, were calculated as follows [92]:

$$D^t = D^0[1 + \alpha p] \tag{3.9}$$

where D^0, α, and p are respectively the initial diffusion coefficient, a material-specific proportionality constant, and scaffold porosity. Porosity of the scaffold increases as degradation takes place and was taken into account in the model through calculating the concentration of the available species in the scaffold [92].

The degree of polymer crystallinity X_{c0} represents the volume fraction of crystalline regions throughout the scaffold, and can change in two ways: (a) crystallization of small degradation by-products because of their greater mobility and (b) accelerated amorphous regions degradation and erosion as compared to the crystalline regions [30]. The temporal variation in PLLA X_{c0} was described by an adaptation of the Avrami equation that neglects degradation within crystalline domains [92, 6]:

$$X_c - X_{c0} = 1 - exp[-(k_c t)^{n_A}] \tag{3.10}$$

where X_{c0}, k_c, and n_A are respectively the initial degree of crystallinity, the temperature dependent degree of crystallinity change rate related to nucleation and growth parameters at isothermal conditions, and an Avrami constant that depends on the nucleation mechanism and crystal growth geometry/mechanism.

The transport of scaffold-derived soluble constituents in the arterial wall were modeled by transient diffusion-convection-reaction processes as follows:

$$\frac{\partial C_j^W}{\partial t} + \mathbf{u_W} \cdot \nabla C_j^W = \nabla \cdot (D_j^W \nabla C_j^W) - jKC_j^W A_1 + 2\sum_{m=j+1}^{7} kC_m^W A_1; 0 < j < 8 \tag{3.11}$$

$$\frac{\partial C_0^W}{\partial t} + \mathbf{u_W} \cdot \nabla C_0^W = \nabla \cdot (D_0^W \nabla C_0^W) + 2\sum_{m=1}^{7} kC_m^W A_1 - K_m C_0^W \tag{3.12}$$

where C_j^W and D_j^W are respectively soluble constituents concentration and diffusion coefficient in the arterial wall; j is number of ester bonds; is any soluble constituents concentration with number of ester bonds between 7 and j+1; C_0^W and D_0^W are respectively LA concentration and diffusion coefficient in the arterial wall; A_1 is the total concentration of constituents with carboxylic acid end groups; and k_m is the irreversible first-order reaction rate constant that characterizes metabolism of LA in the arterial wall.

Lastly, transport of soluble constituents in the lumen were modeled as transient diffusion-convection-reaction processes as follows:

$$\frac{\partial C_j^l}{\partial t} + \mathbf{u_l} \cdot \nabla C_j^l = \nabla \cdot (D_j^l \nabla C_j^l) - jKC_j^l A_1 + 2\sum_{m=j+1}^{7} kC_m^l A_1; 0 < j < 8 \tag{3.13}$$

$$\frac{\partial C_0^l}{\partial t} + \mathbf{u_l} \cdot \nabla C_0^l = \nabla \cdot (D_0^l \nabla C_0^l) + 2\sum_{m=1}^{7} kC_m^l A_1 - K_m C_0^l \tag{3.14}$$

where C_j^l and D^{l_j} are respectively soluble constituents concentration and diffusion coefficient in the lumen; j is number of ester bonds; C_0^l and D_0^l are respectively LA concentration and diffusion coefficient in the lumen.

A steady, Poiseuille parabolic velocity profile with peak velocity of 0.53 $m\ s^{-1}$ was imposed at the luminal inlet and a zero pressure boundary condition was applied at the luminal outlet to simulate coronary arterial flow [75]. The Kedem-Katchalsky equation was used at the mural interface to define the transport of blood plasma from the lumen perivascular wall [41, 19]. For simulating mass transfer, the initial scaffold molecular weight distribution (MWD) was prescribed to achieve specific M_w

and polydispersity index (PDI). A zero concentration boundary condition was assumed at the luminal inlet and a convective flux boundary condition was imposed at the luminal outlet and on the perivascular wall. Continuity of soluble constituents was assumed at scaffold-arterial wall and mural wall interfaces. The Delaunay triangular scheme was used to perform the mesh generation with maximum intensity of elements focused around the scaffold and critical zone. A finite-element model (COMSOL Multiphysics^{TM}) was used to perform numerical simulations and the iterations were continued until the relative error tolerance magnitude reached . The computational solution was considered mesh-independent when the relative change in scaffold M_w and LA concentration was less than 0.1% at any simulated time step between successive mesh iterations. The average computational runtime for each simulation was around 5 hours using an Intel Xeon CPU (2.80 GHz) processor with 20 GB ram.

Accumulation of scaffold-derived LA may lower the local pH below a critical value and induce toxicity in the arterial wall [53]. The critical zone maximum LA concentration ($C_{LA,max}^{Cr}$) and the time at which $C_{LA,max}^{Cr}$ occurs (t_{max}) are therefore considered as performance metrics for scaffold safety assessment. Degradation and erosion kinetics are typically monitored by tracking the Mw and Wt change of the scaffold over time. Hence, degradation and erosion half-lives ($t_{deg}^{1/2}$ and $t_{ero}^{1/2}$) as defined by the time at which the initial M_w and W_t are reduced by 50% respectively, are reported as reduced metrics of the degradation and erosion processes.

3.4 RESULTS

The developed random scission degradation model was validated by comparison to published data describing the transient reduction in M_w of a PLLA disc maintained in static, phosphate buffer solution [90]. An initial PLLA M_w of 7.6 kDa and PDI of 1.34 were imposed in the model to recreate experimental conditions. A theoretical degra-

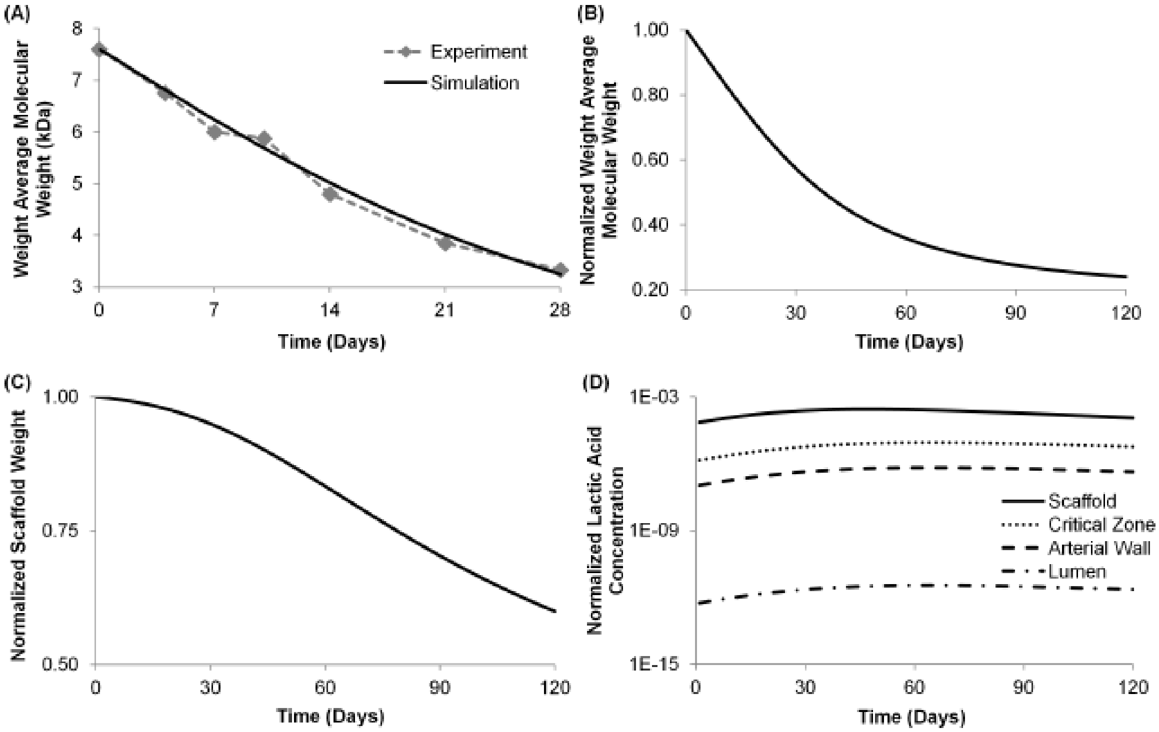

Figure 3.3 **(A)** Transient molecular weight (M_w) profile comparison between predicted results and experimentally-published values [90]. Best-fit model parameters included an initial weight-average MW of 7.6 kDa, initial polydispersity index of 1.34, hydrolytic degradation rate of 1.17×10^{-11} $m^3 mol^{-1} s^{-1}$, initial monomer diffusion coefficient of 1×10^{-13} $m^2 s^{-1}$, constant value of = 4.5, initial degree of crystallinity of 0.24, and degree of crystallization change rate of 4.63×10^{-8} s^{-1}. **(B, C)** Scaffold weight-average molecular weight (M_w) and weight (W_t) decrease nonlinearly with time, with relatively fast degradation and slow erosion at early times. **(D)** Transient lactic acid (LA) concentration profiles in different regions show that the accumulation of scaffold-derived by-product is orders-of-magnitude higher in the critical zone compared to other regions within the computational domain.

dation curve that exhibited excellent correlation (R=0.99) with experimental results was generated by tuning model parameters, yielding a hydrolytic degradation rate of 1.17×10^{-11} $m^3 mol^{-1} s^{-1}$ and initial monomer diffusion coefficient of 1×10^{-13} $m^2 s^{-1}$ (Figure 3.3A). Several experimentally verified-models quantified PLLA hydrolytic degradation rate with the same order of magnitude [4, 3] and a monomer diffusion coefficient between 1×10^{-12} - 1×10^{-14} $m^2 s^{-1}$ [66, 91], indicating that both fitted parameters are within a plausible range. The degree of crystallinity change rate and

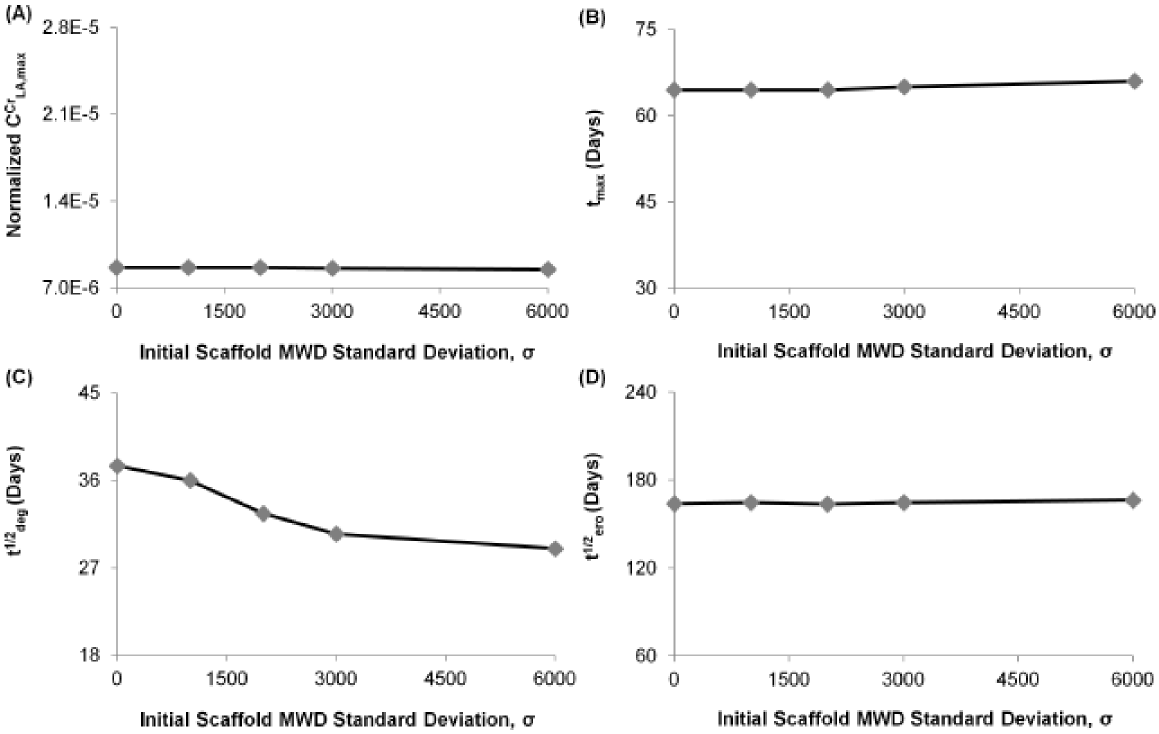

Figure 3.4 **(A, B)** Maximum critical zone LA concentration ($C^{Cr}_{LA,max}$) and the time which $C^{Cr}_{LA,max}$ occurs (t_{max}) are independent of the standard deviation (σ) of scaffold molecular weight distribution (MWD). **(C, D)** Higher σ results in faster degradation as indicated by the time required for 50% reduction of the initial weight-average molecular weight ($t^{1/2}_{deg}$), but does not alter the erosion kinetics as indicated by the analogous measure of weight loss ($t^{1/2}_{ero}$).

Avrami constant were calculated by fitting the Avrami equation against experimental results with an initial degree of crystallization of 0.24 [90].

Isotropic diffusion of all mobile constituents within the scaffold results in a maximal LA concentration at the strut center and a monotonic decrease towards all boundaries (Figure 3.1B). Within the defined critical zone, by-product clearance is augmented by luminal and transmural flow, resulting in reduced LA concentrations in tissue adjacent to the mural interface as compared to other regions. Upon reaching the mural interface, LA is rapidly transported downstream by the luminal blood flow (Figure 3.1D). Conversely, transmural flow convects LA towards the perivascular wall, resulting in higher concentrations beneath the scaffold strut (Figures 3.1B & E). All larger mobile constituents are transported in the same qualitative manner as LA but at relatively slower rates.

For the case of monodisperse PLLA, scaffold degradation is initiated upon deployment as indicated by the immediate decrease in M_w (Figure 3.3B). Scaffold M_w change rate is nearly constant for the first 40 days and then is gradually reduced, resulting in a more than 50% decrease of M_w within first 40 days followed by less than 25% additional reduction over the next 80 days. Scaffold erosion exhibits qualitatively-reversed kinetics, with a slow rate of mass loss at early times (t <30 days) followed by comparatively rapid mass loss for the remaining time (Figure 3.3C). Transient concentrations of scaffold-derived LA within different model regions exhibit order-of-magnitude differences over 120 days (Figure 3.3D). LA concentration is always highest within the scaffold, followed by critical zone, arterial wall, and lumen. Maximum LA concentration in the critical zone is 7.6% greater than in the surrounding arterial wall, motivating the subsequent focus on this region of tissue for risk assessment associated with by-product accumulation.

While maintaining constant number-average molecular weight (M_N), the initial scaffold MWD was systematically varied by increasing the standard deviation (σ) of the initial chain length distribution. Both $C_{LA,max}^{Cr}$ and t_{max} are minimally affected by the initial scaffold MWD profiles (Figures 3.4A & B). In comparison to the monodisperse scaffold ($\sigma = 0$), maximal polydispersity within our investigated range ($\sigma = 6000$) results in the same $C_{LA,max}^{Cr}$ at essentially the same time post-implantation (1.5 days later). Conversely, faster PLLA degradation, as indicated by a reduction in $t_{deg}^{1/2}$, is predicted for scaffolds with greater polymeric dispersion (Figure 3.4C). Approximately 30% decrease in $t_{deg}^{1/2}$ is observed for polydisperse scaffold with $\sigma = 6000$

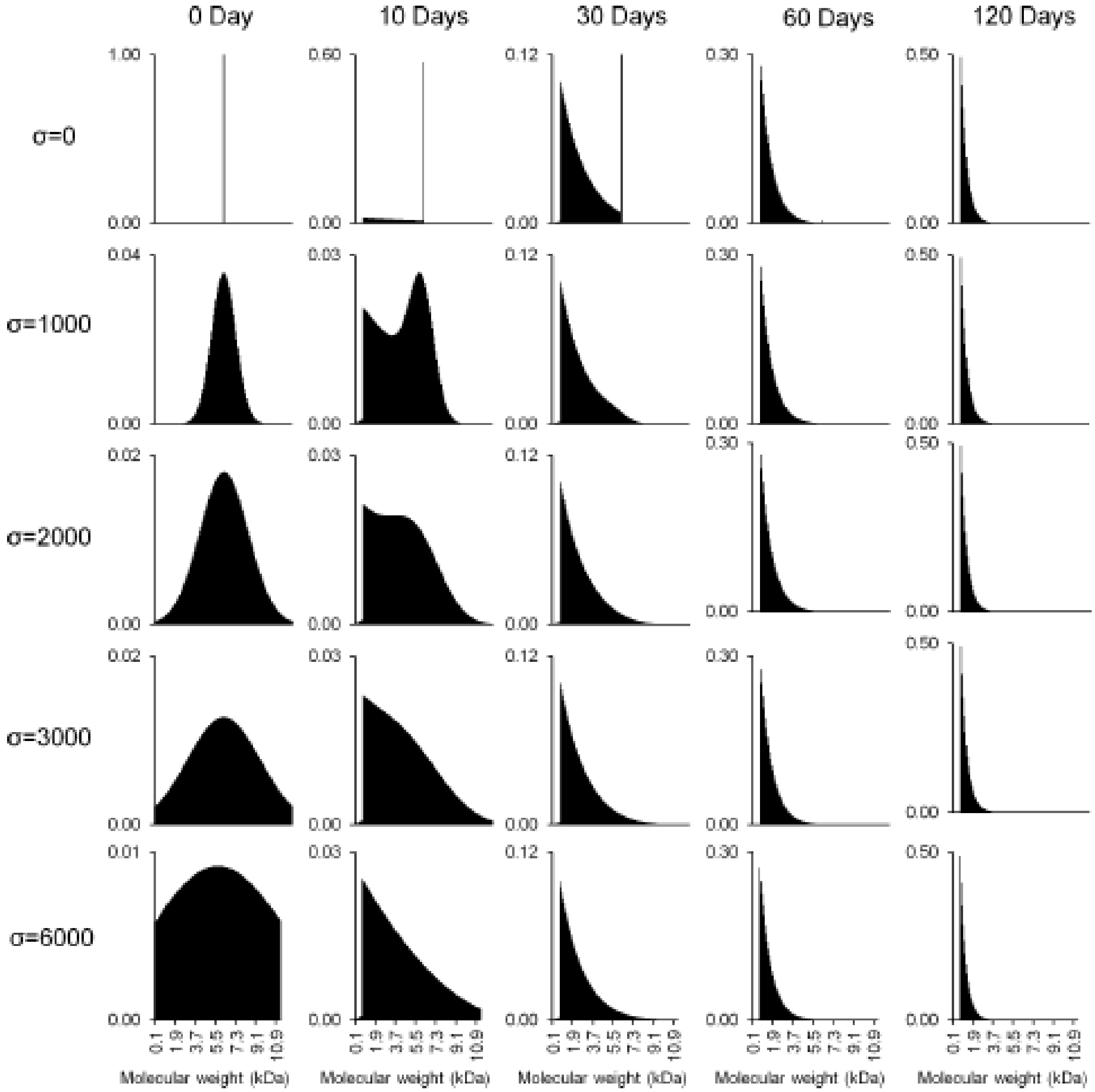

Figure 3.5 Comparative evolution of PLLA molecular profiles with varying initial standard deviations (σ) of the molecular weight distribution. The number of molecules is normalized with respect to total molecules present in the scaffold at t = 0 and presented in the vertical axis.

in comparison to the monodisperse scaffold. Polydispersity has an insignificant effect on erosion kinetics, as indicated by almost equal $t_{ero}^{1/2}$ among all PLLA variants (Figure 3.4D). Transient scaffold profiles reveal that after 30 days the MWD is largely independent of initial PLLA composition (Figure 3.5). These results suggest that the transformation of large constituents into shorter insoluble oligomers is a rapid process

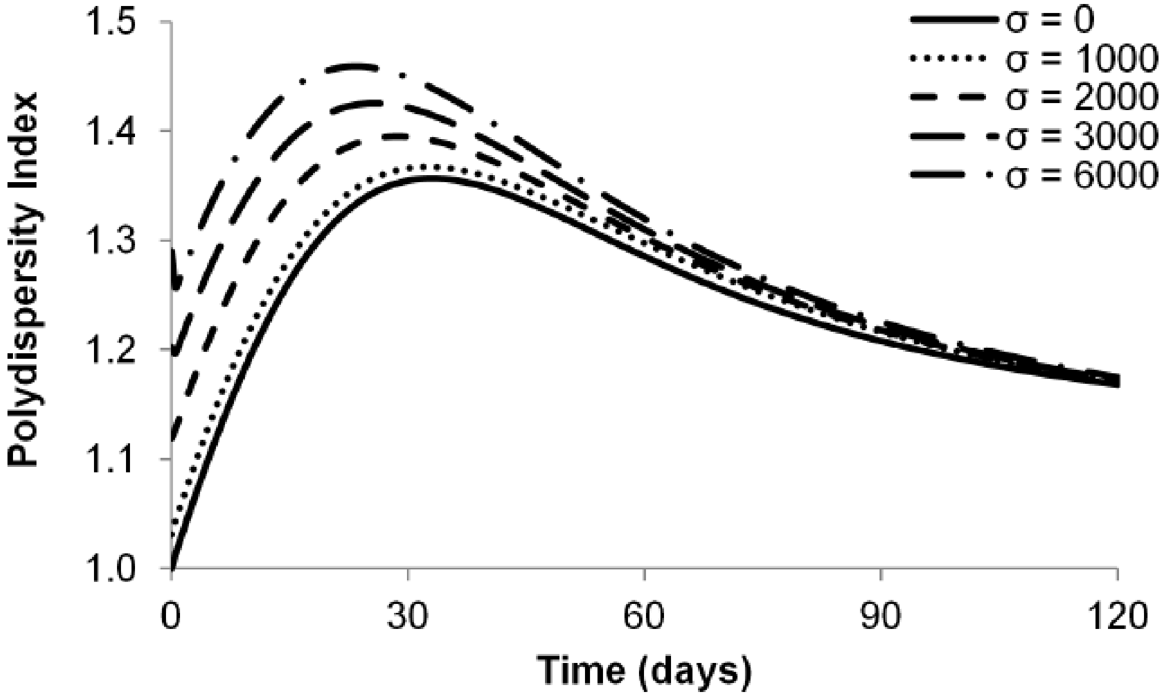

Figure 3.6 Hydrolytic degradation results small chain constituents evolution with wide range of molecular weight (M_w) at the early days followed by more uniform M_w-rich small chain constituents. Polydispersity index (PDI) is defined the ratio of weight-average molecular weight to number-average molecular weight. Higher polydispersity is observed when standard deviation (σ) of initial scaffold molecular weight distribution increases.

in comparison to soluble by-product generation and mass loss. As a consequence, the amount of soluble constituents in the scaffold is insignificant compared to insoluble constituents at all times, irrespective of the initial MWD. Over the range of considered PLLA formulations, degradation and erosion processes essentially homogenize all scaffold PDI by 120 days post-implantation (Figure 3.6).

Higher initial scaffold degree of crystallinity (X_{c0}) results in a linear decrease in $C_{LA,max}^{Cr}$ and a linear increase in t_{max} within the investigated range (Figures 3.7A & B). While both degradation and erosion kinetics are depressed with increasing X_{c0}, the comparative responses of $t_{deg}^{1/2}$ and $t_{ero}^{1/2}$ suggest erosion is the more sensitive Process (Figure 3.7C & D). While $t_{deg}^{1/2}$ is increased by 53%, $t_{ero}^{1/2}$ is increased by 130%

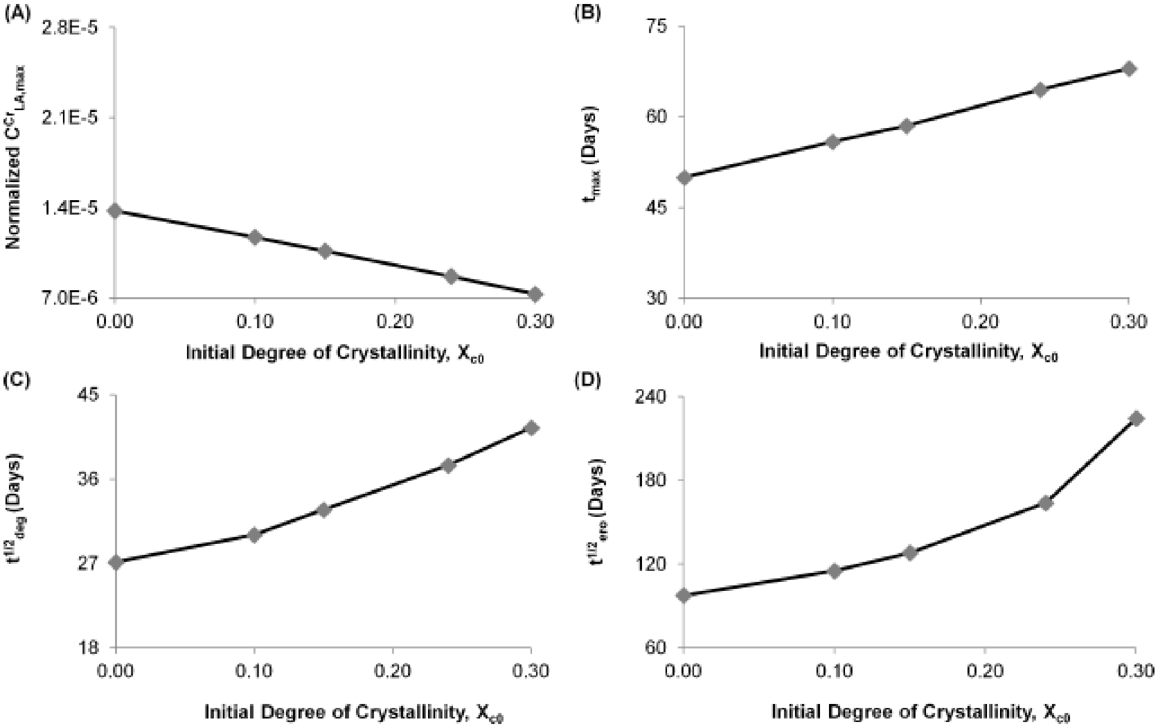

Figure 3.7 **(A, B)** Higher scaffold initial degree of crystallinity (X_{c0}) decreases the critical zone maximum LA concentration ($C_{LA,max}^{Cr}$) and delays the time at which $C_{LA,max}^{Cr}$ occurs (t_{max}). **(C, D)** Degradation and erosion kinetics are protracted by increasing (X_{c0}), as represented by increases in the times at which initial scaffold weight-average molecular weight ($t_{deg}^{1/2}$) and weight ($t_{ero}^{1/2}$) diminish by 50%.

within the investigated range. The degree of crystallinity change rate (k_c) dictates how fast crystalline regions become amorphous. Similar to the effect of increasing X_{c0} higher $k_c$causes a decrease in $C_{LA,max}^{Cr}$ (Figure 3.8A) with negligible change in t_{max} (Figure 3.8B). Increasing k_c slows down both degradation and erosion processes, with a more pronounced effect on the latter as observed by 109% increase within the investigated range (Figures 3.8C & D).

Lactide doping is expected to have a profound effect on all scaffold performance metrics via stimulation of autocatalytic processes. Simulation results predict that inclusion of lactide within the scaffold significantly increases $C_{LA,max}^{Cr}$ and reduces t_{max} (Figures 3.9A & B), and accelerates both degradation and erosion (Figures 3.9C &

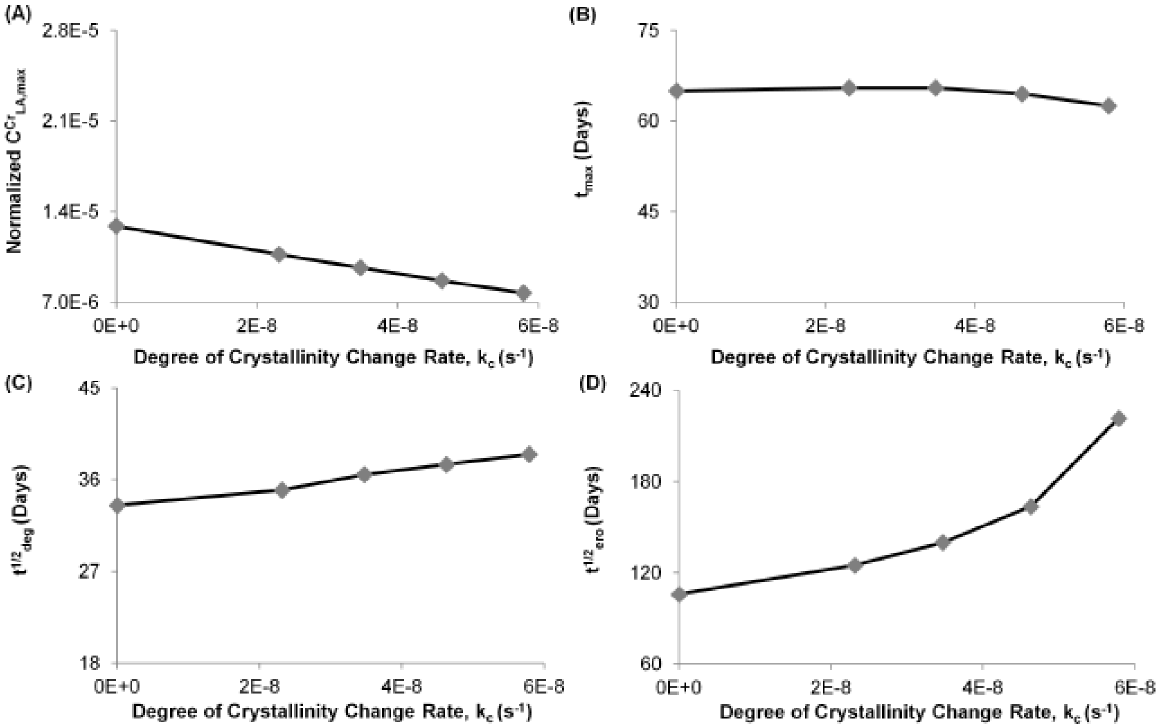

Figure 3.8 **(A, B)** An increased crystallinity change rate (k_c) reduces the critical zone maximum LA concentration ($C^{Cr}_{LA,max}$) and delays the time at which $C^{Cr}_{LA,max}$ occurs (t_{max}). **(C, D)** Trends in $t^{1/2}_{deg}$ and $t^{1/2}_{ero}$ suggest that degradation kinetics are independent of k_c, whereas erosion kinetics are protracted with increasing Degradation and erosion kinetics are protracted by increasing k_c.

B). The effect of lactide inclusion on degradation and erosion is similar, as both $t^{1/2}_{deg}$ and $t^{1/2}_{ero}$ are reduced by 50% when 5 wt% lactide is added to the initial scaffold.

3.5 Discussion

Performance of PLLA-based fully-resorbable endovascular scaffolds critically depends on scaffold degradation and erosion kinetics. Modulations in the molecular weight profile, average molecular weight and microstructure (crystallinity and porosity), as well as incorporation of additives such as lactic acid (LA) are some of the design aspects that can be adjusted during the manufacturing stages to control the fate of *in vivo* by-product distribution. Deeper understanding of these tunable parameters

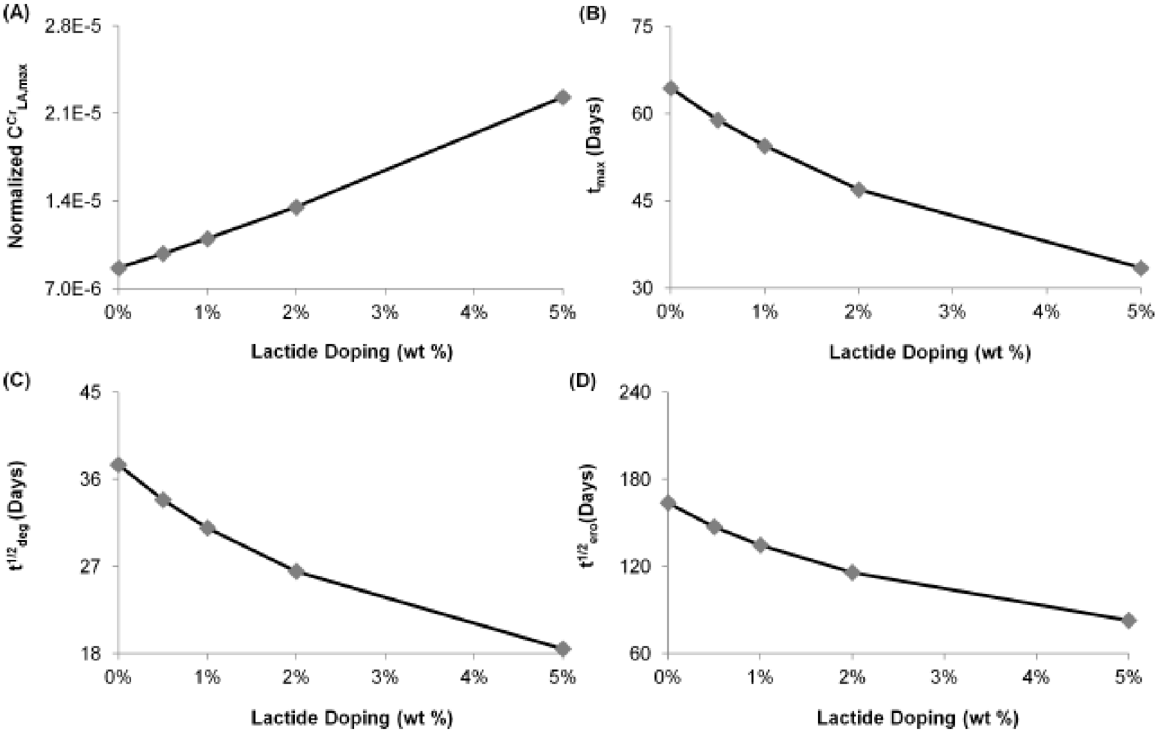

Figure 3.9 **(A, B)** ncorporation of free lactide increases the critical zone maximum LA concentration ($C^{Cr}_{LA,max}$) and decreases the time at which $C^{Cr}_{LA,max}$ occurs (t_{max}). **(C, D)** Excess lactide and its degradation products enhance autocatalytic hydrolysis and accelerate both the degradation and erosion as indicated by reductions in $t^{1/2}_{deg}$ and $t^{1/2}_{ero}$.

is required to enhance overall scaffold performance, and thereby improve the biocompatibility and clinical efficacy of erodible devices. We have used computational modeling to gain insight into the critical determinants of PLLA scaffold degradation and erosion, by accounting the effects of autocatalysis, polydispersity, degree of crystallinity, species-specific transport of scaffold-derived constituents, and porosity change due to degradation, blood flow, and LA metabolism.

Transient concentrations of scaffold-derived degradation by-products are concurrently modulated by the rates of diffusion, convection, generation, and metabolism. A parametric sensitivity analysis was performed to quantify the relative influence of structural and compositional factors on scaffold performance (Table 3.1). A relative change index (RCI) was calculated to quantify the percent change of defined performance indicators when material parameters are varied in isolation from the lowest to highest considered values. The safety assessment of PLLA modifications is based on the RCIs of $C^{Cr}_{LA,max}$ and t_{max}, whereas degradation and erosion assessments are based on $t^{1/2}_{deg}$ and $t^{1/2}_{ero}$, respectively.

Fine tuning of polydispersity was expected to enable a reduction in the inflammatory potential of PLLA scaffolds through protraction of LA generation [90]. A mixture theory based on a previously proposed model suggested that bulk polymer erosion was significantly affected by initial polydispersity due to early stage soluble constituents overall enhanced diffusivities [79]. However, our results show that though initial polydispersity affects scaffold LA production, it has negligible effect on LA accumulation adjacent to the scaffold and only mildly affects degradation (RCI =

Table 3.1 Sensitivity analyses on PLLA structural and compositional parameters. Relative change index (RCI) is based on percent increase (+) or decrease (-) of defined performance metrics due to isolated changes of material parameters. Safety assessment is based on maximum critical zone lactic acid concentration and the time at which it occurs. Degradation and erosion assessments are based on the corresponding half-lives ($t^{1/2}_{deg}$ and $t^{1/2}_{ero}$) when initial scaffold weight-average molecular weight and weight are reduced by 50% respectively.

Parameter	Range	Relative Change Index (RCI)			
		Safety Assessment (Concentration)	Safety Assessment (Time)	Degradation Assessment	Erosion Assessment
Initial Scaffold MWD Standard Deviation	0 - 6000	- 2 %	+ 2 %	- 29 %	+2 %
Initial Scaffold Degree of Crystallinity	0 - 0.3	- 47 %	+ 36 %	+ 53 %	+ 130 %
Degree of Crystallinity Change Rate, s^{-1}	0 -5.8×10^{-8}	- 40 %	- 4 %	+ 15 %	+ 109 %
Initial Lactide Doping, wt%	0 - 5	+ 157 %	- 48 %	- 51 %	- 49 %

+29%). This finding reinforces the notion that it is difficult to predict how a single material parameter will impact critical zone LA pharmacokinetics that are modulated by the relative rates of LA generation, diffusion within the scaffold, release into local tissue, transport within the arterial wall, and metabolism.

Increase in the degree of crystallinity due to the degradation of the amorphous regions gradually slows overall degradation and erosion rates, as crystalline regions are relatively resistant to hydrolytic breakdown [2]. Because the degradation rate at early times is maximal, $t_{deg}^{1/2}$ exhibits a moderate sensitivity to X_{c0} (RCI = +53%) and a mild response to k_c (RCI = +15%). On the other hand, erosion rates are initially slow and thus are highly sensitive to both X_{c0} and k_c, as reflected in the corresponding $t_{ero}^{1/2}$ RCIs. Previous studies have reported that PLLA degradation is accelerated with increasing X_{c0} due to two factors: (i) a decreased density of effective tie chains between adjacent crystalline blocks and (ii) increased void spaces in the amorphous regions which ultimately prompt hydrolysis by enhancing water diffusion [85]. However, the degradation response to X_{c0} was reported to vary substantially with polymer processing methodologies, most notably the employed film annealing temperature, which may account for the contradiction with our current findings [2]. Scaffold X_{c0} can be controlled by modifying the annealing and/or quenching protocols, whereas k_c at a specific temperature can be controlled by adding nucleating agents during the manufacturing process [51]. Hence, both X_{c0} and k_c provide potential avenues for selective tuning of scaffold degradation and erosion kinetics.

While lactide doping can potentially be used to tune scaffold degradation and erosion kinetics, the concomitant increase in tissue LA concentration should also be considered. Our study suggests that lactide doping should be employed with high precision in scaffold manufacturing due to the promotion of by-product accumulation. Although the inclusion of lactide has been previously considered and remains a promising scaffold design strategy, the risk associated with an elevated tissue response is significant and should be assessed with *in vivo* studies [70].

3.6 Study Limitations and Future Works

Although the proposed degradation model is verified using previously reported values from a static experimental study [90], the predicted degradation kinetics under physiologic conditions have not been validated with or compared to published data. While only *in vivo* studies can validate the predictions of this computational model, the requisite number of studies that would be needed considering the complexity of synthesizing scaffolds with precise variations of structural properties precludes inclusion of this validation from the current body of work. However, our computational study is a valuable contribution to the field as it suggests critical parameters that one may focus on when performing future animal studies. Moreover, the model could be extended to three-dimensions to better account for flow-mediated processes, but due to symmetry of the vessel (and most scaffolds as well) and computational cost, the study was conducted in two-dimensions. In comparison to our earlier study where all the degradable species were divided into only five groups to identify the dominating factors that modulate the fate of scaffold derived by-products clearance [75],here we have tracked all individual species generated during scaffold degradation to better understand the consequences of structural variations - this resulted in a substantially more complex model. With our current resources, coupling three-dimensional geometry effects with our detailed degradation model would have dramatically increased the computational time of the simulations (most likely an exponential increase). Computational costs also limit the examination of very high initial M_w-rich scaffolds that are typically used in endovascular applications. Modeling the performance of high M_w-rich scaffolds in three-dimensional environments will be interesting to investigate in future.

Although degradation processes are theoretically initiated at the time of implantation, PLLA-based bioresorbable scaffolds have been shown to provide structural support to vessel walls for prolonged times with minimum risk of restenosis [77]. Specifically, the PLLA-based bioresorbable Everolimus eluting stent results in an acceptable angiographic in-stent late loss, low stent area obstruction, no late thrombosis, and minimal neointimal hyperplasia after 6 months post-implantation [62]. While these factors are certainly related to the mechanical strength of the scaffold that may impact long-term performance, predicting the degradation-induced change in scaffold mechanical properties is not within the scope of this study. Moreover, a fully-embedded scaffold was considered in this simulation from the initial stage though it has been reported that fully bioresorbable vascular scaffolds are completely covered by the fibromuscular neointima by 4 weeks after implantation [59]. Finally, the pulsatility of blood flow was neglected due to the fully-embedded scaffold position and the minimal effect on constituent transport within the arterial wall. These are important aspects that need to be considered in developing a model to fully appreciate the efficacy of endovascular therapy using biodegradable scaffolds. Our current study lays a foundation to address these issues which we in fact plan to explore in our future studies.

3.7 Conclusion

Advanced design of erodible endovascular scaffolds requires careful assessment of material properties that impact implant performance and safety in the arterial environment. Our study reveals that potential variations in polymer composition and structure differentially impact metrics of performance. Specifically, we found that degradation is minimally affected by changes in either PLLA polydispersity or the initial degree of crystallinity, while erosion is sensitive to crystallinity. Additionally, scaffold degradation, erosion, and by-product accumulation were all responsive to lactide doping. Computational modeling serves as an efficient means to evaluate possible tuning strategies and enable improved design of erodible scaffolds.

Chapter 4

THE IMPARTED DEGREE OF RADIAL EXPANSION MODULATES DRUG ELUTING BIORESORBABLE VASCULAR SCAFFOLD PERFORMANCE

[1]

4.1 Abstract

Drug eluting bioresorbable vascular scaffolds (BRS) have the inherent potential to enable complete restoration the native vascular environment, an insomuch offer a distinct advantage over permanent percutaneous endovascular intervention technologies. To ensure that therapeutic gains are conferred for a sufficient period of time prior to scaffold resorption, the multitude of factors that dictate key metrics of BRS performance must be identified, characterized, and optimized. Some deterministic factors are controlled in the BRS design and manufacturing processes, while others depend on the specific method and site of implantation. The focus of this is study is to understand how and to what extent the imparted degree of radial expansion at the time of implantation modulates BRS performance, a factor which falls into the latter category. The significant variation in target arterial dimensions among individuals,

---

[1] Ferdous, J., Fatematuzzahan, Kolachalama V. B., and Shazly T. To be submitted to *Journal of Controlled Release*

e. g. the coronary artery diameter ranges from about 2-5 mm, as well as the differential geometries presented in various stages of plaque progression, suggest the need to expand BRS on an application-specific basis. To gain insight on the potential clinical implications, we systematically varied the radial expansion of a BRS composed of poly DL-lactide-glycolide and generated *in vitro* metrics of degradation, erosion, and drug release kinetics. Experimental data were used to develop a finite-element based computational model that predicts the transient concentrations of scaffold derived soluble species and drug in the arterial wall following various degrees of expansion. Taken together, our results demonstrate that BRS safety and efficacy will be significantly influenced by the degree of radial expansion and provide a foundation for continued product design and development.

4.2 Introduction

Drug eluting bioresorbable scaffolds (BRS) have the potential to displace metallic drug-eluting stents (DES) as the technology-of-choice in percutaneous coronary intervention (PCI) based on the inherent ability to mitigate the occurrence of late thrombosis. The transient resorption of BRS could enable gradual restoration of the native vascular environment, and thus promote complete vessel healing and recovery of function. Despite this apparent advantage and over thirty years of research and development [80], the introduction of BRS into clinical practice has been stifled by regulatory concerns and a lack of the necessary data to demonstrate superiority over current technologies. Only two manufactured BRS have received the CE mark of approval, which allows use in the European Economic Area, while none have been approved by the United States Federal Drug Administration. Although there are a few pre-clinical and early-phase clinical trials that cumulatively show therapeutic potential, there have been no randomized clinical trials with DES to demonstrate that BRS specifically lower risk of late and very late stent thrombosis [60].

In addition to providing superior efficacy over DES, the clinical introduction of BRS is predicated on a thorough demonstration of device safety that specifically addresses the risks inherent to erodible implants. A primary risk factor of BRS is the occurrence of early fracture, which has historically been a concern in metallic DES and is magnified in polymer-based endovascular devices. While material selection and fabrication protocols can be tuned to promote the requisite mechanical strength for the intended therapeutic duration, it is now evident that BRS strut malapposition and otherwise inappropriate deployment can enhance early fracture rates [61]. Irrespective of the specific base polymer and manufacturing technique, a given BRS will be limited by a maximum attainable degree of expansion prior to the onset of mechanical failure [73]. Thus, it is possible that BRS over-expansion at deployment could induce a fracture that immediately limits the ability of the device to restore lumen patency. Conversely and in a similar fashion to DES, under-expansion increases the risk of thrombosis due to an alteration of *in situ* scaffold geometry and concomitant disturbance of arterial blood flow [88].

To select appropriate BRS and balloon sizes for a given application, a priori measurement of vessel lumen diameter is typically performed with quantitative coronary angiography (QCA). Following this preliminary assessment, a surgeon would then select from a limited number of available BRS sizes and subsequently impart the necessary degree of radial expansion at deployment based on patient-specific geometry. Such measures are likely to ensure against instances of obvious over- and under-expansion, but will not fully eliminate inter-patient variation in the degree of expansion.

It is logical to posit that the degree of radial expansion will play a significant role in determining BRS performance, as the in-situ microstructure of the constituent polymeric network will accordingly vary and likely impact the rates of key kinetic processes for an erodible drug delivery device. To better understand the mechanisms by which device expansion alters device performance, we systematically varied the degree of radial expansion of BRS composed of poly DL-lactide-glycolide (PLGA) and generated *in vitro* metrics of degradation, erosion, and drug release kinetics. Experimental data were used to construct a finite-element model that predicts the transient concentrations of released drug and degradation by-products in the arterial wall. Our findings suggest that the imparted expansion will significantly alter the clinical safety and efficacy of BRS, and therefore support the need to carefully account for and control this parameter in device deployment.

4.3 Materials and Methods

Preparation of resorbable scaffolds

A solution-casting method was applied used to prepare PLGA- based resorbable scaffolds [89]. Homogenized polymer solutions of research grade, ester terminated 50:50 PLGA having with an inherent viscosity of 0.82 dL g^{-1} (LACTEL Absorbable Polymers, Alabama, USA) were achieved created by dissolving predetermined amount of PLGA pellets in dichloromethane (Fisher Scientific, New Hampshire, USA) followed by stirring for 24 hours at room temperature. To prepare films, tThe polymer solution was poured on a glass panel and a casting knife with a tunable clearance was moved over the solution at fixed speed to spread the solution along the direction of the movement and attain to yield uniform wet film thickness of 60 μm. To enhance the evaporation of residual dichloromethane from the wet film, the glass plate was placed in a fume-hood at ambient conditions for 24 hours followed byand then in a vacuum oven at 50 °C for one week. Dry films thickness was tuned through manip-

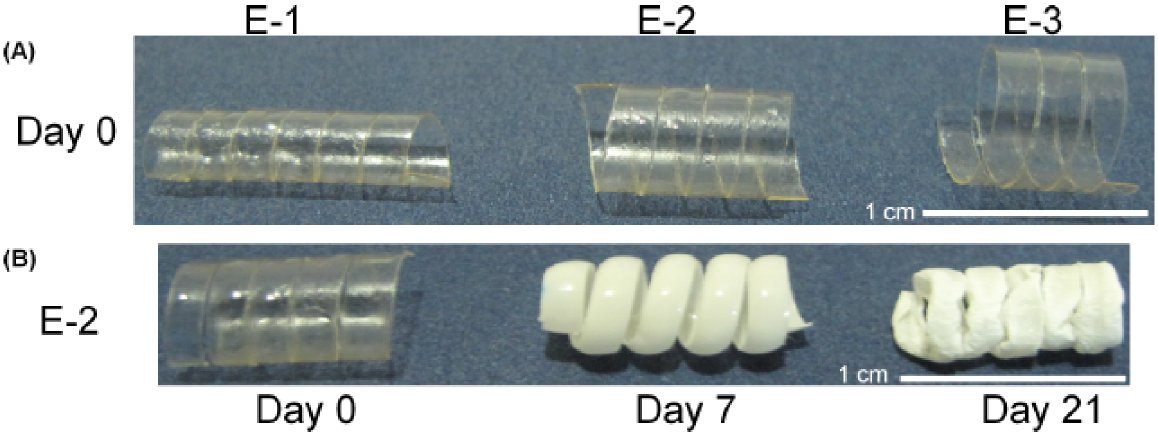

Figure 4.1 Helical bioresorbable scaffolds with different degrees of expansion prior to **(A)** and after **(B)** submersion in PBS for various time periods.

ulating the polymer concentration and wet film thickness, and resulting in 150±15 μm thick dry films were achieved as measured using a digital micrometer.

Dried films were cut into a rectangular strips of 70×2 mm^2 and wound onto a Teflon rod. Wound films were then heated at 50 °C for 24 hours to form the helical scaffolds. Finally, a balloon catheter was used to expand the scaffolds inside three different sizes of Teflon tubes to simulate different degrees of radial expansion (E-1, E-2, and E-3) as defined by the ratio of scaffold diameter before and after expansion (Figure 4.1A). Drug containing scaffolds (3% w/w) were prepared by homogenized mixing of the polymer solution with an 99.5% pure drug Paclitaxel prior to film formation (LC Laboratories,MA, USA).

In vitro erosion and degradation

Dried scaffolds were weighted (W_0) before immersion into the phosphate buffered saline (PBS) maintained at 37 °C and pH of 7.4. PBS medium was replaced daily to maintain pH levels, which is critical as PLGA polymer degradation is a pH sensitive process [2]. At predetermined times, samples were weighted after gently removing unabsorbed solution from the scaffold surface (W_{wet}). After multiple rinses with deionized water, samples were dried at 37 °C for one week and weighted (W_{dry}). Scaffolds water absorption and erosion/weight loss kinetics were calculated as follows.

$$Water absorption(\%) = \frac{W_{wet} - W_{dry}}{W_{dry}} \times 100\% \tag{4.1}$$

$$Erosion(\%) = \frac{W_0 - W_{dry}}{W_0} \times 100\% \tag{4.2}$$

Gel permeation chromatography (GPC, Polymer Laboratories) was used to analyze the weight-average molecular weight (M_w) and polydispersity index (PDI) of dried scaffolds. A linear M_w profile (R^2=0.9999) of polystyrene (Polymer Standards Service, Massachusetts, USA) was used as standards to calibrate the GPC system. Samples were dissolved in HPLC-grade anhydrous tetrahydrofuran (THF) (Fisher Scientific, New Hampshire, USA) at a concentration between 10-15 mg mL^{-1}, which also provided the solvent for the mobile phase of the GPC (flow rate of 1 mL min^{-1}, injection volume of 200 μL sample^{-1}). Oven temperature was maintained at 30 °C while the pressure was held 4 at Mpa.

Radial strength study

A uniaxial mechanical testing system (3200 testing system, Bose ElectroForce®, Minnesota, USA) was used to measure the radial strength of dried scaffolds. Samples were placed between two flat compression test fixtures and subjected to a ramped uniaxial compressive displacement of 0.5 mm at 0.005 mm sec^{-1}. Sample force and displacement data were continuously recorded at an acquisition rate of 10 points sec^{-1} using a system integrated software (Wintest®, Minnesota, USA).

In vitro Paclitaxel release study

Individual teflon tubes containing drug-loaded dried scaffolds were completely immersed in separate glass vials containing PBS (pH of 7.4) and 10% (v/v) dimethyl sulfoxide (DMSO) (Fisher Scientific New Hampshire, USA). DMSO was used to enhance paclitaxel solubility in PBS and restrict the Paclitaxel adherence with glass walls [48]. A perfect sink condition was maintained and all glass vials were kept in the incubator at 37 °C throughout the release study. Intact scaffolds at initial time points were dissolved in acetone to measure drug dissolution (Fisher Scientific, New Hampshire, USA). Paclitaxel was quantified by an Agilent Series 1100 HPLC (Agilent Technologies, California, USA) equipped with a 4.6×150 mm LiChrospher RP-18 (particle size: 5 μm). The mobile phase consisted of 60% (v/v) HPLC grade acetonitrile (Sigma-Aldrich, Missouri, USA) and 40% (v/v) deionized water with a flow rate 1 mL min_{-1}. The injection volume was 100 μ sec^{-1} and UV detection was performed at 227 nm with the column oven temperature at 30 °C. Paclitaxel retention time was approximately 5 min. A linear concentration profile (R^2=0.99) of 0.1 âĂŞ 100 μM paclitaxel was used as a standard for calibration (Figure 4.2A).

Morphological characterization

Exterior surface morphology of the scaffolds was analyzed using a variable pressure scanning electron microscope (SEM) (Tescan Vega-3 SBU) at accelerating voltage of 20 kV. Prior to image acquisition, segments of dried scaffolds were coated using a Denton Vacuum Desk II Gold Sputter (New Jersey, USA) for 60 sec^{-1} at approximately 35 mA current and chamber pressure of P $<$ 100 mTorr. Scaffold porosities were calculated from the images using a National Institutes of Health developed open-source image processing program (ImageJ). Computational

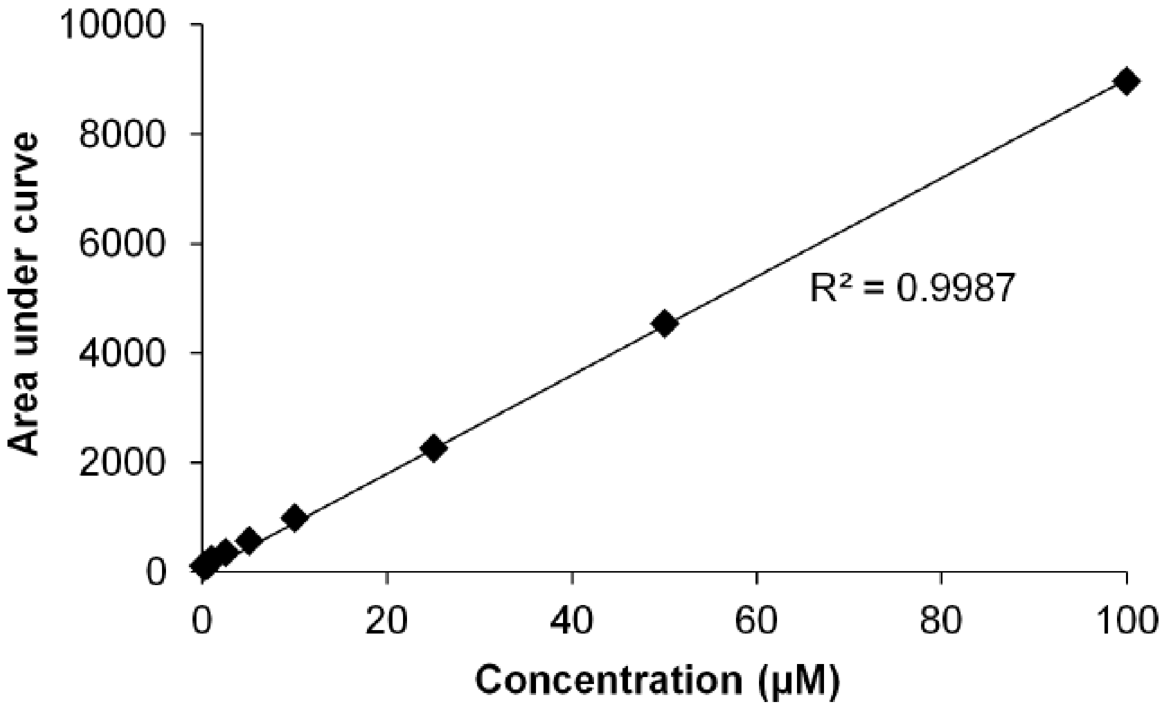

Figure 4.2 Calibration curve for paclitaxel detection.

Computational model

A two-dimensional finite-element model was developed to investigate the effect of radial expansion on soluble species and drug pharmacokinetics within the arterial wall. The computational domain was comprised of a cross-section of an arterial wall with 1 mm thickness, and a single fully-tissue embedded square-shaped scaffold strut of dimensions 0.1 × 0.1 mm. Degradation was modeled as a random scission process of ester bonds between monomers, while bulk erosion was modeled as the release of soluble species from the strut domain [20]. The concentrations of insoluble species were modeled by the following reaction equations:

$$\frac{dC_n^S}{dt} = -nkC_n^S A \tag{4.3}$$

$$\frac{dC_i^S}{dt} = -ikC_i^S A + 2\sum_{m=i+1}^{n} kC_m^S A \tag{4.4}$$

where n, C_n^S, k, and A are respectively the number of ester bonds, concentration of the largest species, hydrolytic degradation rate, and autocatalytic factor; C_i^S, i, C_m^S are respectively the insoluble species concentration, number of ester bonds, and insoluble species concentrations with the number of ester bonds between n and $i+1$.

The concentrations of soluble species (small oligomers and monomers) inside the scaffold (C_0^S) were modeled by the following diffusion-reaction equation:

$$\frac{\partial C_0^S}{\partial t} = \nabla \cdot (D_0^S \nabla C_0^S) + 2 \sum_{m=1}^{n} k C_m^S A \tag{4.5}$$

where D_0^S is the diffusion coefficient of soluble species in the scaffold that was modelled as an experimentally-derived empirical function of current scaffold M_w. The concentrations of soluble species in the arterial wall (C_0^W) were modeled by the following diffusion-reaction equation:

$$\frac{\partial C_0^W}{\partial t} = \nabla \cdot (D_0^W \nabla C_0^W) - K_m C_0^W \tag{4.6}$$

where D_0^W and $K_m = 10^{-5}\ m^2 sec^{-1}$ are the diffusion coefficient and metabolism rate of soluble species in the arterial wall, respectively [88].

Assuming diffusion as the dominant transport mechanism for drug within the arterial tissue and reversible binding to nonspecific tissue sites [14, 50, 52, 87, 86], the concentration kinetics of Paclitaxel in the arterial wall was modeled by the following equations:

$$\frac{\partial C_{p,f}^W}{\partial t} = \nabla \cdot (D_p^W \nabla C_{p,f}^W) - \frac{dC_{p,b}^W}{dt} \tag{4.7}$$

$$\frac{dC_{p,b}^W}{dt} = K_a C_{p,f}^W (B^M - C_{p,b}^W) - K_d C_{p,f}^W \tag{4.8}$$

where $C_{p,f}^W$ and $C_{p,b}^W$, are respectively the concentrations of free and bound Paclitaxel in the arterial wall; $D_{p,f}^W = 5.71 \times 10^{-10}\ m^2 s^{-1}$ and $B_M = 13$ mol m^{-3} are respectively the Paclitaxel diffusivity and net tissue-binding capacity; $k_a = 21.97$ mol $m^{-3}s^{-1}$ and $k_d = 2.98798$ s^{-1} are respectively the Paclitaxel association and dissociation rate constants [46].

Based on the molecule retention profiles from the GPC, the initial scaffold molecular weight distribution (MWD) was prescribed to achieve initial $M_w = 55.757$ kDa and PDI = 1.24. A zero concentration boundary condition was imposed both at the intramural interface and perivascular wall. Continuity of soluble species concentrations was assumed at the scaffold-arterial wall interface. For drug transport, zero initial free and bound Paclitaxel concentrations at the arterial wall were imposed. Assuming erosion mediated drug release and using experimental drug release profiles, a scaffold weight dependent concentration boundary condition was imposed for the free drug at the scaffold-arterial wall interface. For the free drug, a zero concentration condition was applied at the perivascular wall whereas a zero flux boundary condition was assumed at the intramural interface due to hydrophobicity of Paclitaxel and high resistance provided by the intima. For the bound drug, zero flux boundary condition was assigned at mural interface, scaffold-arterial wall interface, and the perivascular wall.

All transient simulations were solved using a standard finite-element based software package (COMSOL Multiphysics^{TM}, Comsol, Inc.). A Delaunay triangular scheme was used to mesh the computational domain with maximum intensity of elements adjacent to the scaffold strut. Iterative mesh refinement was performed until the relative error tolerance reached 10^{-5}. The numerical solution was deemed to be mesh independent when the relative change in average arterial wall soluble species and Paclitaxel (free and bound) concentrations was less than 1% for successive mesh refinements.

Statistical analysis

Results are presented as the average and standard errors of at least three independent samples at each time point. Considering incubation time and degree of expansion as independent variables, statistical analyses were performed using both one-way and two-way ANOVA followed by Tukey's post-hoc multi-comparison test. Experimental differences were considered statistically significant at $p < 0.05$. The coefficient of determination (R^2) and Pearson product-moment correlation coefficient (r) were computed to respectively assess the goodness of fit of linear regression and strength of correlation between the independent variables and performance metrics

4.4 RESULTS

Constant initial drug dose and surface area were maintained for all the scaffolds irrespective of the degree of expansion, implying a variation in scaffold length (Figure 4.1A). Glassy and flexible initial scaffolds transformed to whitish and brittle within one week of degradation and began to lose their structural integrity thereafter (Figure 4.1B). Not surprisingly, water permeated into the scaffold as soon as it was placed in the buffer solution, resulting in increased scaffold weight with uptake increasing significantly along with incubation time ($p < 0.001$) (Figure 4.3A)). Scaffold absorbed water more than 50% of its weight by the end of 14 days. Water uptake was also significantly affected by the degree of expansion ($p < 0.01$), with 2-fold higher expansion of the scaffolds leading to over 40% higher uptake in the first week.

Water uptake by the scaffold immediately resulted ester bonds scission of polymer chains and generated smaller oligomers and monomers by the hydrolysis reaction as observed by decreasing M_w profiles (Figure 4.3B). Generation of smaller oligomers and monomers diverged the species MWD profiles and increased PDI the (Figures 4.3C & D). Average degradation half-life of the scaffolds ($t_{deg}^{1/2}$), defined as the time at which

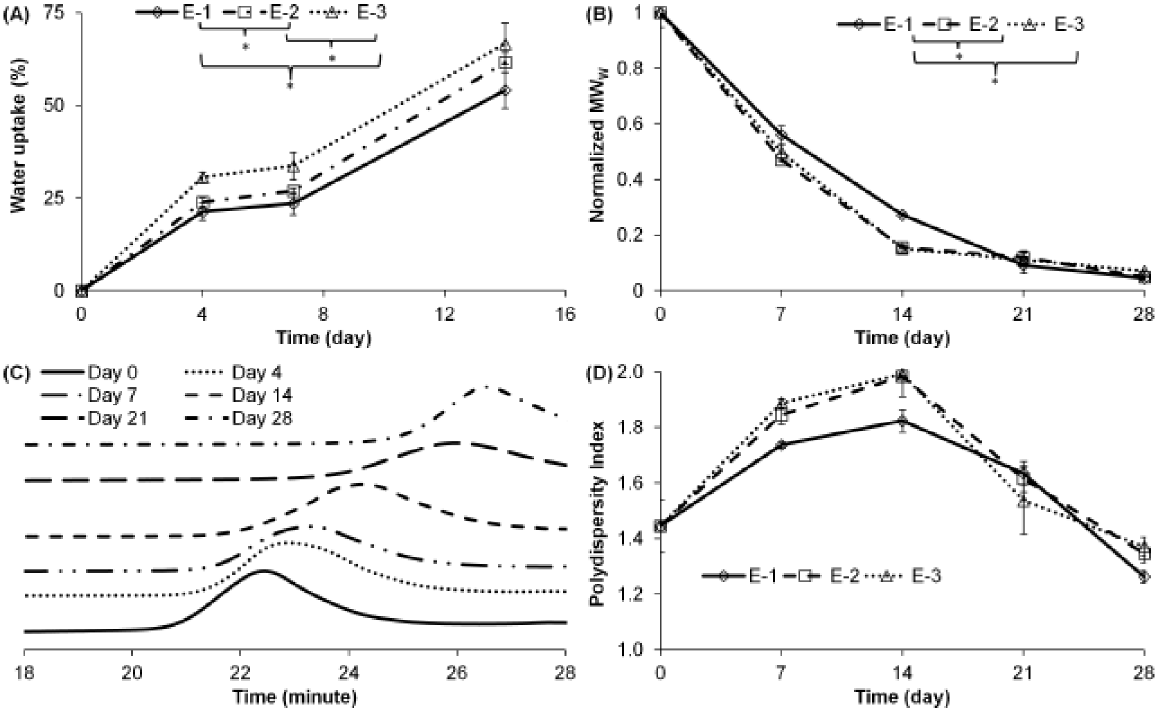

Figure 4.3 Water uptake **(A)**, Molecular weight **(B)**, GPC molecule retention profile **(C)**, and polydispersity **(D)** of variably expanded BRS as a function of submersion time in PBS. * statistically significant at $p < 0.05$.

the initial M_w is reduced by 50%, were less than one week. Within first two weeks of degradation, scaffold lost almost 80% of its initial M_w and generated most diverged MWD profile. After two weeks, presence of smaller oligomers and their degradation resulted less M_w change and decreased PDI. Meanwhile, higher degree of expansion resulted faster overall M_w reduction ($p < 0.005$). Scaffold M_w reduced 44% more for E-3 in comparison to E-1 after two weeks. Though the M_w profiles of the lowest expanded scaffold are significantly lower than rest, similar M_w profiles were observed after 3 weeks irrespective of the degree of expansion.

The time delay between generation of enough soluble species and their release from the scaffold resulted the slow erosion process at the initial stage. Hence, almost no weight loss was observed till two weeks (Figure 4.4A). Scaffolds started to lose weight gradually after three weeks and by week four, E-1, E-2, and E-3 lost 29%,

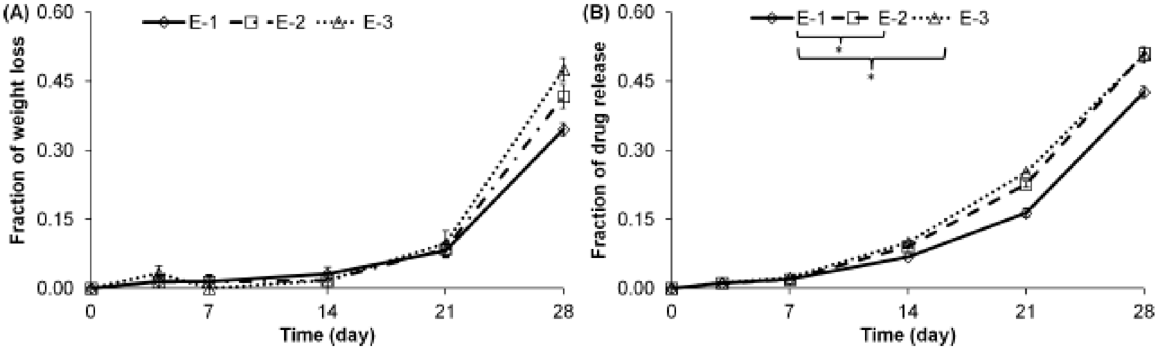

Figure 4.4 Weight loss **(A)** and paclitaxel release **(B)** profiles from variably expanded BRS over 28 days submersion in PBS. * statistically significant at $p < 0.05$.

36%, and 42% of their initial weight, respectively. The erosion half-life of the scaffolds ($t_{ero}^{1/2}$), defined as the time at which the W_0 is reduced by 50%, was predicted from the erosion kinetics profiles as more than four weeks irrespective of the degree of expansion. Though degree of radial expansion does not affect the overall erosion kinetics ($p > 0.1$), E-3 lost 38% higher weight than that of E-1 in four weeks ($p < 0.05$).

Drug slowly released from the scaffolds at the initial stage where less than 10% of total initial drug was released in first two weeks (Figure 4.4B). However, faster drug release was observed in next two weeks with almost 50% of initial drug released by four weeks. No burst release of Paclitaxel was observed for any of the scaffolds. Degree of radial expansion markedly enhanced Paclitaxel release kinetics ($p < 0.001$). Scaffolds having lowest expansion ratio released less amount of drug than other scaffolds. At the end of four weeks, almost 20% more Paclitaxel was released when scaffold degree of expansion was increased from E-1 to E-3.

Characterization of scaffold's mechanical property is very critical to understanding its effectiveness to support and retain native vessel structure and prevent recoiling. Therefore, response in mechanical properties due to degradation and different

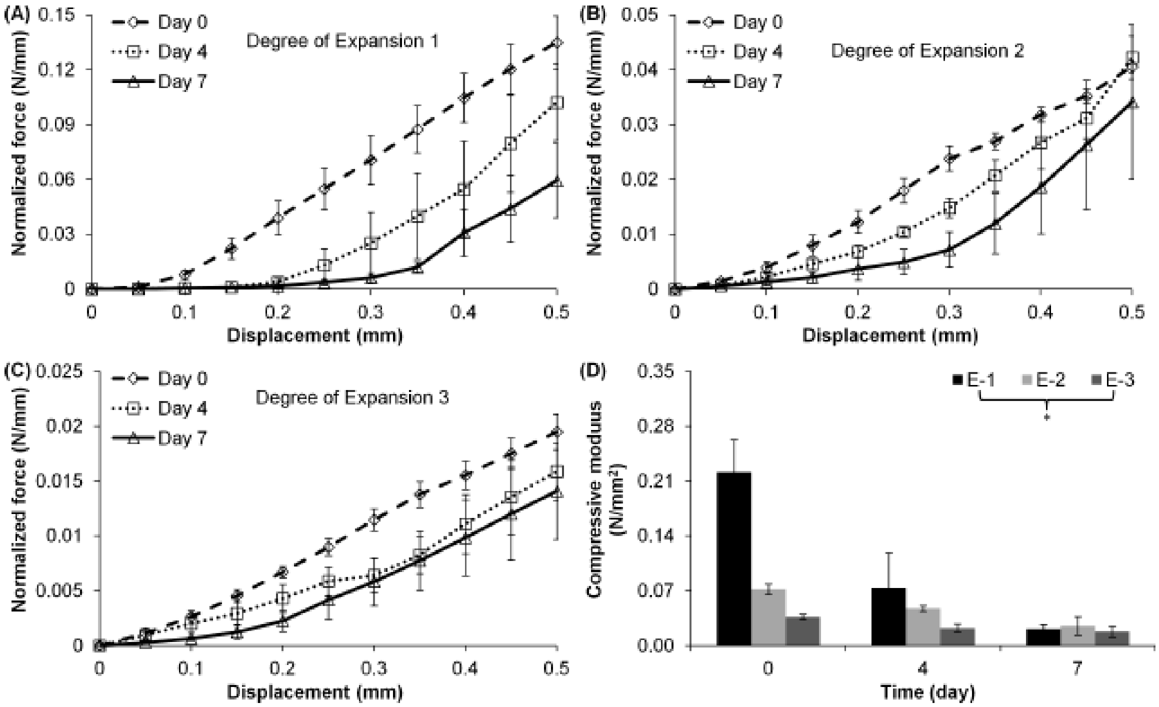

Figure 4.5 Compressive load vs. displacement profiles **(A-C)** and radial strength as measured by the compressive modulus **(B-D** of variably expanded BRS over 7 days submersion in PBS. * statistically significant at $p < 0.05$.

degrees of expansion are important to investigate. All forces were normalized with corresponding scaffold length to minimize the effect of contact surface area. Compressive modulus (E_c) represented the radial strength of the scaffold and were calculated based on the slope of the linear regression model of force exerted by the scaffold for 0 to 0.3 mm displacement (Figure 4.5A. All the scaffolds lost their radial strengths as degradation took place as indicated by the decreased E_c (Figure 5D) where E-1 lost more than 90% of its initial radial strength by one week. Higher degree of expansion significantly altered the initial and E-1 exhibited 6-fold higher initial radial strength than that of E-3 ($p < 0.05$). Overall, radial strength of E-1 was estimated to be significantly higher than that of E-3 over the investigated one week ($p < 0.01$). Non-uniform scaffold structure limited radial strength investigation after one week.

SEM of the scaffolds surface illustrates that the porosity significantly increased

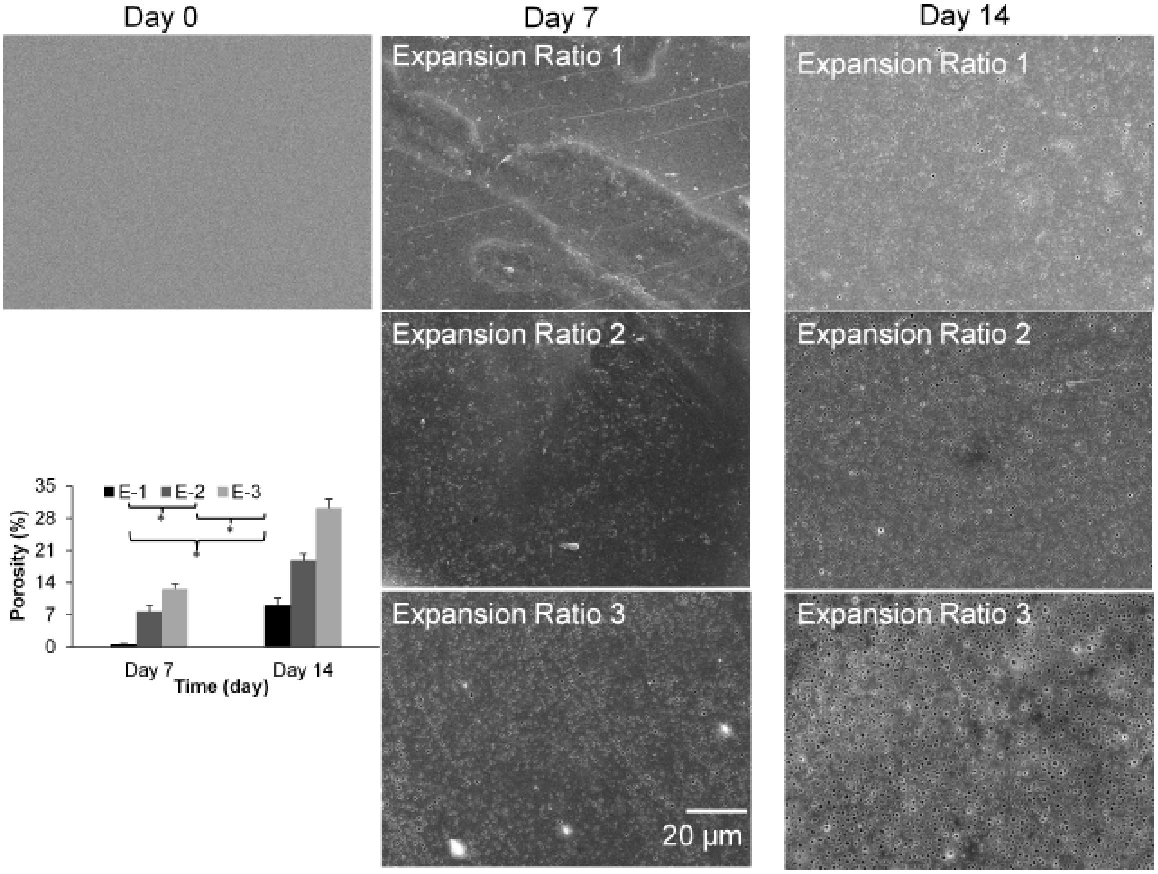

Figure 4.6 Porosity of variably expanded BRS over 14 days submersion in PBS. * statistically significant at $p < 0.05$.

with the degradation time ($p < 0.001$) and degree of expansion ($p < 0.001$) (Figure 4.6). Although the initial scaffold porosity was negligible, E-3 resulted more than 20-fold and 3-fold higher void areas than that of E-1 after one and two weeks of degradation, respectively. Almost similar pore size was observed over the degradation period, hence number of pores homogeneously increased with time and degree of radial expansion. Computational model-based predictions of the degradation profiles showed excellent correlation with experimental findings (Figure 4.7), where an initial soluble species diffusion coefficient of 1×10^{-13} m^2s^{-1} and hydrolytic degradation rate of 4.0×10^{-8} $m^3mol^{-1}s^{-1}$, 4.3×10^{-8} $m^3mol^{-1}s^{-1}$, and 4.6×10^{-8} $m^3mol^{-1}s^{-1}$ were estimated for E-1, E-2, and E-3, respectively.

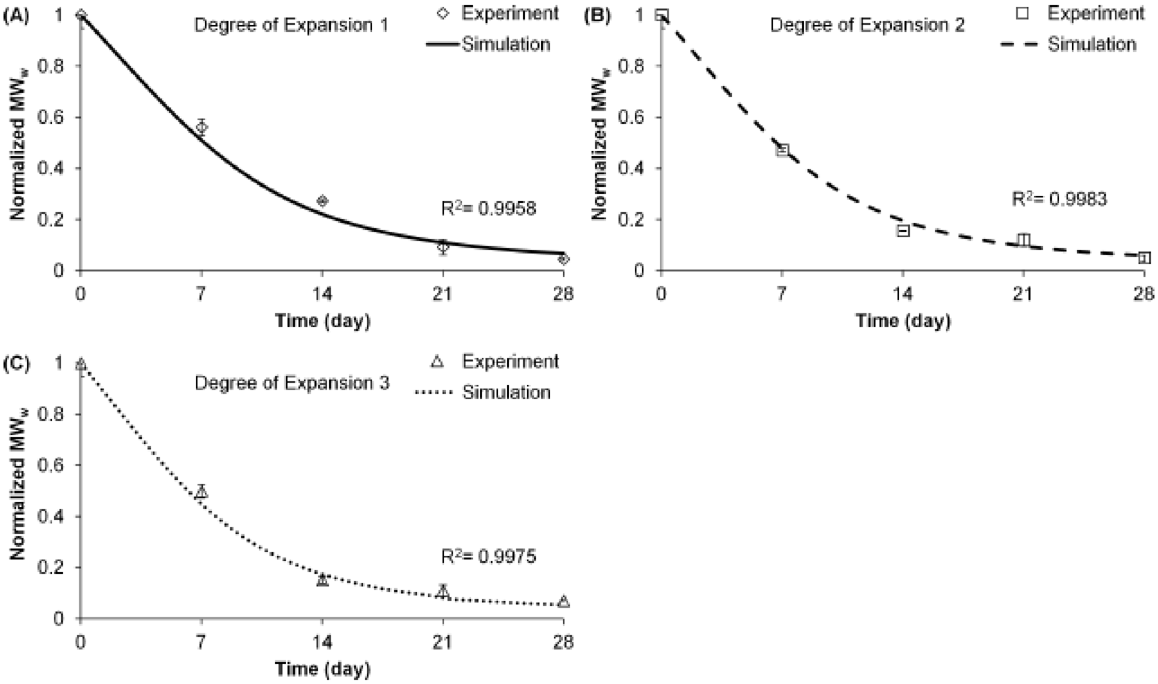

Figure 4.7 Transient M_W profiles of scaffold having different degree of radial expansion comparing the predicted results with experimental findings.

Isotropic diffusion and homogeneous initial distribution of soluble species inside the scaffold yielded maximal soluble species concentration at the core of the strut (Figure 4.8A). Meanwhile, clearance from intramural surface due to blood flow resulted minimal species accumulation in the regions adjacent to the intramural surface and strut. Accumulation of soluble species in the arterial wall at the early stage (until 30 days) demonstrated that the rate of species release from the scaffold exceeded the clearance within this time span. Degree of expansion markedly influenced the peak arterial wall soluble species concentration (Figure 4.8B). Peak soluble species concentration was increased by 15% when the scaffold was expanded 2-fold more from E-1 even though only 5% more weight loss was observed at corresponding time points (Figure 8C). This result leads to the inference that the degree of expansion indirectly modulates the hydrolytic degradation rate and controls the soluble species release kinetics from the scaffold accordingly.

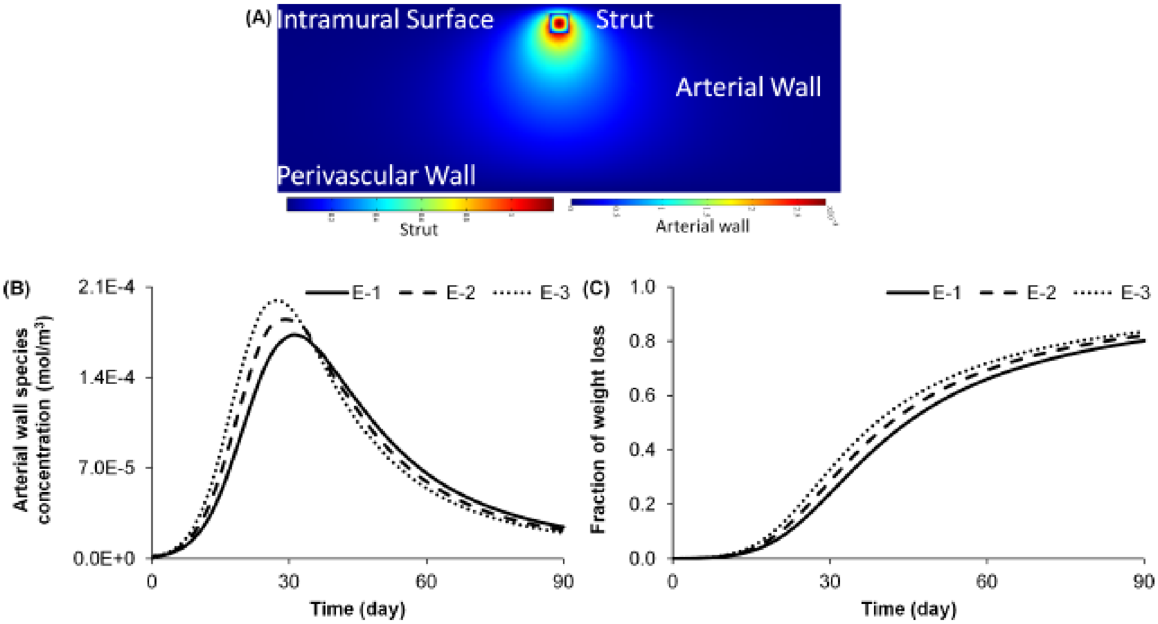

Figure 4.8 Soluble species concentration surface plot consisting a scaffold strut fully embedded within the arterial wall **(A)**. Color bars represent soluble species concentration for each domain. Arterial wall soluble species concentration **(B)** and scaffold weight loss **(C)** of variably expanded BRS as a function time.

Scaffold implantation immediately resulted in peak Paclitaxel concentration in the arterial wall that remained invariant until two weeks and started to decrease thereafter (Figure 4.1B). Degree of radial expansion minimally affected arterial wall drug content after two weeks and resulted maximum 6% lower drug content in E-3 than E-1. Most of the drug in the arterial wall was available as a bound form as illustrated by the high bound-to-free drug ratio (Figure 4.9C). Since it required some time to transport the free drug from the scaffold surface to the perivascular wall, washout of free drug through the perivascular wall increased the bound-to-free drug ratio in the later stage. Higher scaffold expansion minimally affected the bound to free drug ratio and a maximum of 4% higher ratio was observed in E-3 than E-1.

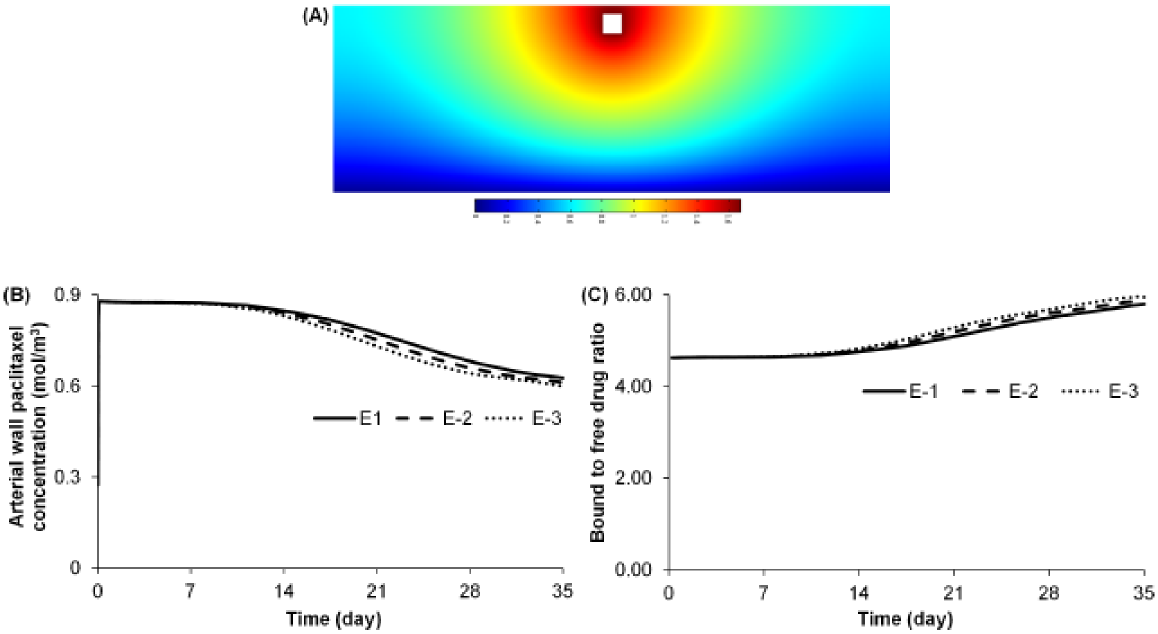

Figure 4.9 Paclitaxel concentration surface plots within the arterial wall **(A)**. Color bar represents paclitaxel concentration. Arterial wall paclitaxel concentration **(B)** and bound to free drug ratio **(C)** of variably expanded BRS as a function time.

4.5 DISCUSSION

Initial slow paclitaxel release from the scaffold is controlled by the diffusion, whereas erosion mediated paclitaxel release in the later stage. Despite of faster hydration, water molecules are unable to transport paclitaxel due to hydrophobicity of paclitaxel. However, onset of erosion markedly enhances the drug release process. Overall, a good linear correlation is observed between the fraction of released drug and erosion ($R^2 = 0.92$) (Figure 4.10A). Radial strength of the scaffold are not only dependent on the initial scaffold deployment but also linearly dependent on the M_w within the first week of degradation (Figure 4.1B). Scaffolds preserve structural integrity until 50% of initial M_w is available. Rate of M_w decrease is higher than the rate of water absorption suggesting that on top of hydrolysis reaction there may be other factors affect the ester bond scission and among which autocatalysis is the major factor. Meanwhile, higher water absorption rate over erosion confirms bulk erosion which

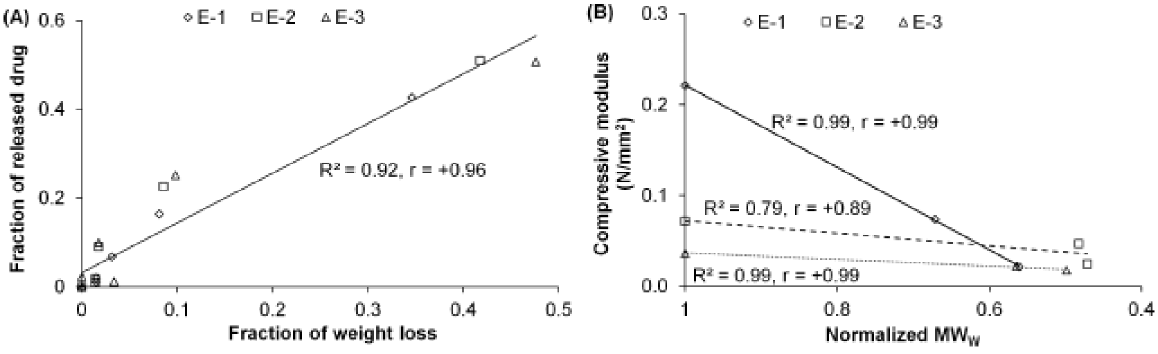

Figure 4.10 Paclitaxel release as function of weight loss **(A)** and compressive modulus as function of M_w **(B)** of variably expanded BRS.

was expected for this scaffold as the thickness of the scaffold was below the critical thickness for surface erosion [28]. Controlled $t_{deg}^{1/2}$ and $t_{ero}^{1/2}$ can be achieved by tuning the material during the manufacturing process e.g. type of polymer, initial M_w, additive, lactide-to-glycolide ratio, end-group capping, porosity, degree of crystallinity, and taking consideration of implant site environmental situation as M_w change is markedly affect by the enzyme activity, temperature, pH, and medium flow condition [2, 20, 23]. All these factors eventually affect the drug release kinetics and radial strength.

In vitro metrics of BRS performance are significantly influenced by the degree of deployment. More pore formation under stretched condition favors water penetration into the scaffold matrix thus enhanced the hydrolytic degradation. As a consequence, mechanical stiffness of the scaffold is decreased that increases the likelihood of scaffold fracture and loss of structural integrity. Dilation beyond 3.5 mm of a 3.0 mm resulted strut fracture as observed by the OPT and early restenosis due to early recoil by the disrupted scaffold [61]. The fractured strut protruded into the lumen, however it was not clear whether the adverse outcome had any association with strut fracture. A metallic stent was used to trap the strut against the vessel wall and restore vessel scaffolding. The fractured strut could be washed away by the blood distal to the strut and result severe ramification. The 4.0 mm BRS from Abbott vascular appeared to be safe and effective when under-expanded in small vessels (<2.5 mm), with similar clinical and angiographic outcomes observed when compared with those of the over-expanded in large vessels (>2.5 mm) [16].

Though, under-expansion condition was not considered in the study, smaller vessel size due to under-expanded scaffolds may be less able to accommodate the same volume of NH as compare to larger vessel and result increased rate of restenosis. Previous studies on BRS have suggested a association between the thicker struts and increased risk of restenosis [88]. Although less drug release is observed for low degree of scaffold deployment due to smaller pore volume, fortunately computational results suggest that the arterial wall paclitaxel concentration is degree of deployment independent and highly diffusion controlled. Otherwise, lower drug release may not be strong enough to trigger the therapeutic effect to minimize NH and restenosis accordingly. Extensive *in vivo* experiment will be required to investigate the effect of scaffold deployment of arterial drug content and restenosis rate.

Fate of degradation by-products (soluble species) are considered another important safety factor associated with BRS. Excessive accumulation of these acidic by-products lowers the local pH and could result necrosis. While *in vitro*/*in vivo* tracking of arterial soluble species adjacent to the scaffold strut at different degree of scaffold deployment are difficult to determined, computational studies provide a complementary way to predict the soluble species pharmacokinetics. Results indicate that scaffold with higher expansion are more likely to decrease the pH. Arterial soluble species pharmacokinetics are erosion controlled, hence can be tuned by manipulating the factors those affect scaffold erosion kinetics. Although the model parameters were used for paclitaxel based on the porcine femoral arteries and arterial ultrastructure and drug type markedly affect the local drug uptake [37], this preliminary study will guide the future comprehensive *in vivo* study.

4.6 Conclusion

Personalized medical therapy is an emerging practice of medical treatment offering tailored solutions to each individual. Although changes in strut design and alternation of polymeric processing increase the vessel diameter working range, it is suggested to use site-specific BRS for safe and effective clinical outcomes. Careful and adequate sizing of vessel diameter are of paramount importance for the correct performance of this scaffolding technique and require accurate assessment of vessel dimension by QCA prior to implantation.

CHAPTER 5

EFFECT OF DYNAMIC ENVIRONMENT ON BIORESORBABLE SCAFFOLD PERFORMANCE

[1]

5.1 INTRODUCTION

Late-in-stent restenosis, the primary drawback of current metal based drug-eluting stent (DES), motivated the innovation of bioresorbable scaffolds (BRS) as an alternative to DES that resorb after controlled period of time and restore normal vascular function [60]. Though first BRS was implanted in human more than 15 years ago [80], only two types of BRS (Absorb everolimus-eluting bioresorbable vascular scaffold (BVS) and DESolve® Novolimus Eluting Coronary Scaffold) met European regulatory requirements. There are several procedural, lesion, patient, and design related factors associated with BRS implantation that can result major post complication. To determine the robustness of this mode of treatment and compete with current DES, BRS has to be effective in patients with acute coronary syndromes who have the highest risk of late and very late stent thrombosis.

Aliphatic polyesters such as poly-lactic acid (PLA), poly-glycolic acid (PGA), and their copolymers poly-lactic-co-glycolic (PLGA) are most commonly used as bioresorbable polymers [57]. Generally, the hydrolytic degradation of these polyester in

---

[1] Ferdous, J., Fatematuzzahan, Kolachalama V. B., and Shazly T. To be submitted to *Journal of Controlled Release*

aqueous media proceeds through random ester bond scission between the monomers. However, degradation causes a increase of the number if carboxylic chain ends which know to autocatalyze the ester hydrolysis process [25]. Only the soluble species (small oligomers and monomers) near the exterior surface can escape from the polymer matrix whereas those which are located well inside the matrix remain entrapped ad contribute totally to the autocatalytic effect. Degradation rate also markedly depends o the amount of water absorption. Release of soluble species depends on surrounding environments and more specifically factors like solubility, pH, ionic strength, and temperature [2, 23]. These surrounding medium are dynamic of physiological conditions and nature of the flow in terms of volume, pulsatility, pressure varies among different arteries. Even the nature of blood flow profiles significantly varies among individuals along with their sex, and age [17, 72].

Luminal blood flow profiles also modulate the thrombosis formation adjacent to the strut [69]. Generation of stagnant or recirculation zone around the struts favors thrombus accumulation. Luminal blood flow profiles also dictate the arterial wall drug accumulation kinetics [45, 8]. The released drug from the drug-eluting stent (DES) is entrapped in the stagnant zones that act as a pocket for drug. These accumulated drug acts as a secondary source and increase the local arterial wall drug concentration that eventually leads to neointimal hyperplasia.

To reduce the cost and time of clinical trials and animal studies, the effectiveness of BRS can be preliminary investigated by simple *in silico* and/or bench top *in vitro* experiments that mimic the physiological and pathological environments. In current study, a *in vitro* dynamic flow system that mimic the physiological conditions were developed and compare with static flow system to better understand the effect of flow. Results indicated that presence of fluid flow significantly altered the scaffold performance matrixes as monitored by water uptake, degradation, erosion and radial strengths duo to autocatalysis. This study motivates to investigate the effect of pulsatile flow o scaffold performance matrix in future.

5.2 Materials and Methods

Preparation of resorbable scaffolds

Resorbable scaffolds were prepared using PLGA based polymer films and solution-casting method was applied to prepare the films [89]. Homogenized solutions of research grade, ester terminated 50:50 PLGA having an inherent viscosity of 1.15 dL g^{-1} (LACTEL Absorbable Polymers, Alabama, USA), antiproliferative drug paclitaxel (LC Laboratories, Massachusetts, USA), and plasticizer Poly(ethylene glycol) having average M_w of 4000 kDa were achieved by dissolving them in dichloromethane (Fisher Scientific New Hampshire, USA) followed by stirring for 24 hour at room temperature. The polymer solution was then poured on a glass panel and a casting knife with a tunable clearance was moved at fixed speed to spread the solution to attain uniform wet film thickness. To enhance the evaporation of residual acetone from the wet film, the glass plate was placed in a fume-hood at ambient condition for 24 hour followed by in a vacuum oven at 37 °C for one week. The thickness of the dry films was tuned through manipulating the polymer concentration and wet film thickness. The thickness of the dried films was 150±15 μm which was measured using a digital micrometer. The dried films were cut into a rectangular strip of 70×2 mm^2 and wound onto a Teflon rod followed by heat at 37 °C for 24 hours to form a helical scaffold. Finally, each scaffold was inserted into a Teflon tube.

In vitro erosion and degradation

Dried scaffolds were weighted (W_0) before immersion into the medium containing 90%(v/v) phosphate buffer saline (PBS) having pH of 7.4 at 25 °C and 10% (v/v) dimethyl sulfoxide (DMSO) (Fisher Scientific New Hampshire, USA). DMSO was used to enhance paclitaxel solubility in PBS and restrict the paclitaxel adherence with surface. Since PLGA polymer erosion and degradation are pH sensitive [2], bulk medium was maintained and medium was replenished with fresh PBS solution in every 3-4 days. To simulate static condition, scaffolds were placed into a glass jar with 50 mL of medium at 37 °C and ensured that there was no bubble inside the Teflon rod, hence the scaffolds were completely exposed to the medium. To simulate the physiologic dynamic condition, a 12-channel peristaltic pump (Ismatec, Germany) was used and ran at medium velocity of 30 mL min^{-1}(Figure 5.1 & Figure 5.2) [33]. Continuous medium flow was maintained through a closed flow system and 37 °C medium temperature was maintained using a water heater bath. Tube length were remained constant from the outlet of the pump to the inlet of the test section to ensure same pressure at the test section.

At every predetermined time intervals, samples were taken out and weighted after removing the absorbed solution on the surface of the scaffolds (W_{wet}). Water absorption kinetics of the scaffolds was calculated as follows:

$$Waterabsorption(\%) = \frac{W_{wet} - W_{dry}}{W_{dry}} \tag{5.1}$$

After multiple rinse with deionized water to wash-out surface PBS , the samples were dried at 37ÂřC for one week and weighted (W_{dry}). Erosion or weight loss kinetics of the scaffolds was calculated as follows:

$$Erosion(\%) = \frac{W_0 - W_{dry}}{W_0} \tag{5.2}$$

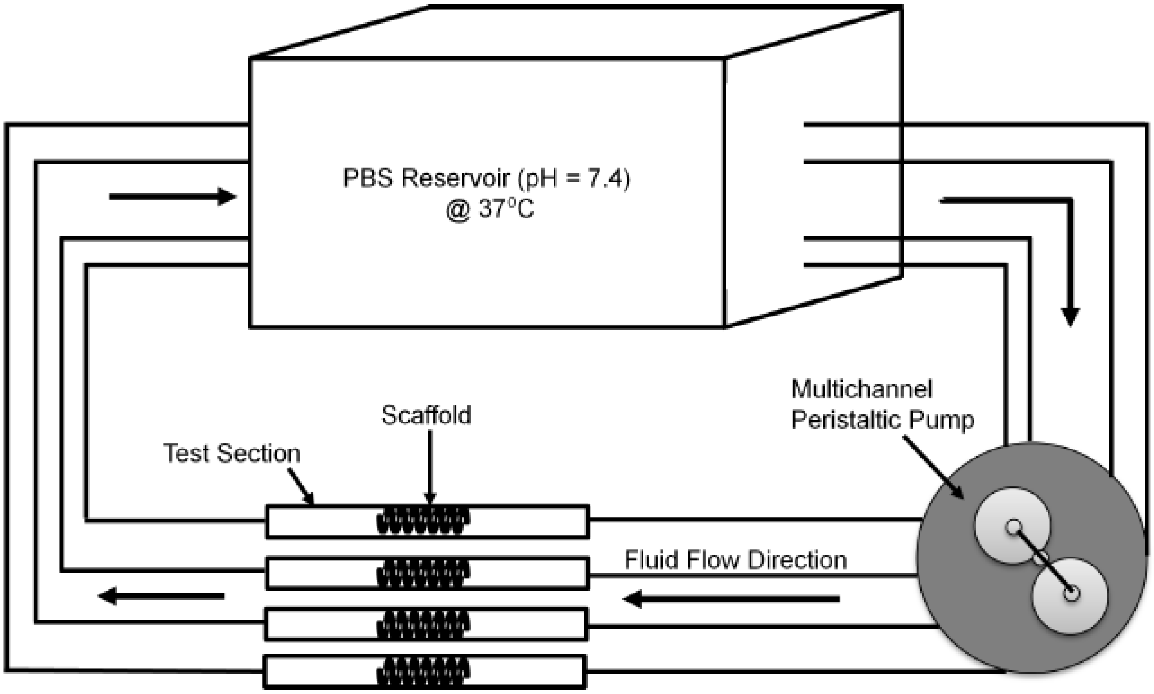

Figure 5.1 Experimental of the simulated dynamic system containing the peristaltic pump, test section with scaffold, PBS reservoir in water bath at 37 °C.

Gel permeation chromatography (GPC) from Polymer Laboratories was used to analyze the weight-average molecular weight (M_w) and polydispersity index (PDI) of dried scaffolds. A linear M_w profile (R^2=0.9999) of polystyrene (Polymer Standards Service, Massachusetts, USA) was used as standards to calibrate the GPC system. HPLC grade anhydrous tetrahydrofuran (THF) (Fisher Scientific, New Hampshire, USA) was used to dissolve the polymer at a concentration between 10-15 mg mL^{-1} and as a solvent for the mobile phase of the GPC at a flow rate of 1 mL min^{-1}. For each sample, 200 μL of the dissolved solution was injected into the GPC. Temperature of the oven was maintained at 30 °C while the pressure was approximately 4 MPa.

Radial strength study

Radial strength of the dried scaffolds was measured using an ElectroForce® load frame 3200 testing system from Bose® (Minnesota, USA). Samples were placed between two

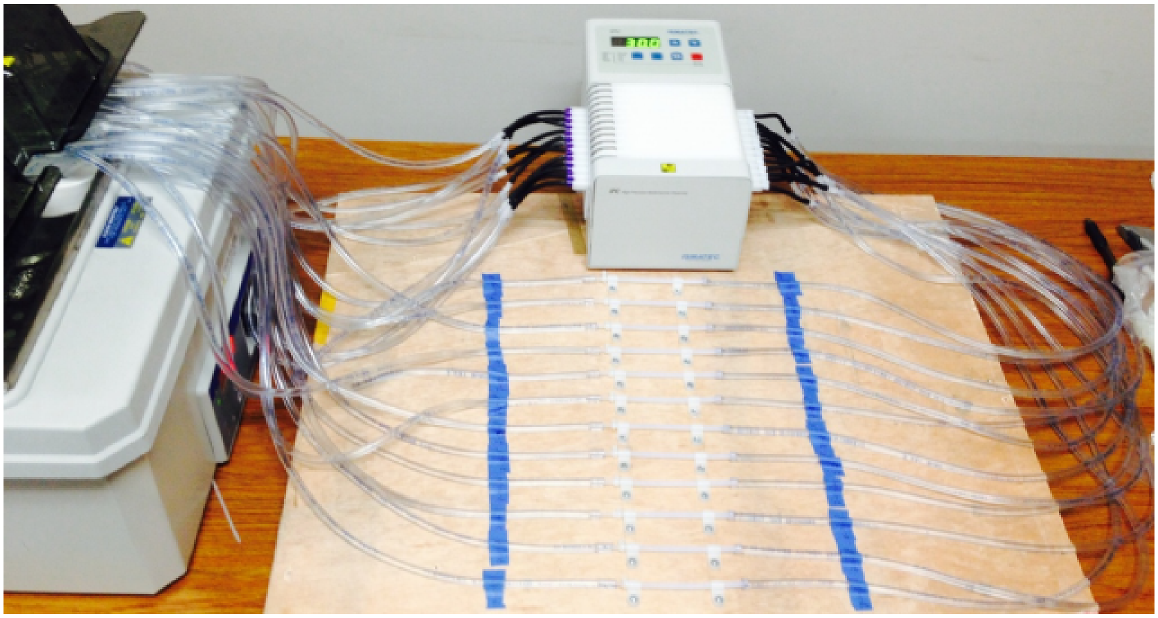

Figure 5.2 Schematic diagram of the simulated dynamic system containing the peristaltic pump, test section with scaffold, PBS reservoir in water bath at 37 °C.

flat compression test fixtures and were subjected to a ramped uniaxial compressive displacement of 0.5 mm at a rate of 0.005 mm sec^{-1}. Sample forces and displacements data were continuously recorded at a data acquisition rate of 10 points sec^{-1} using a software package Wintest® Software (Minnesota, USA).

Statistical analysis

Results are presented as the average and standard errors of atleast three independent samples at every time points. Considering incubation time and medium flow condition as independent variables, statistical analyses were performed using two-way ANOVA followed by Tukey's post-hoc multi-comparison test. Experimental differences were considered statistically significant at $p < 0.05$.

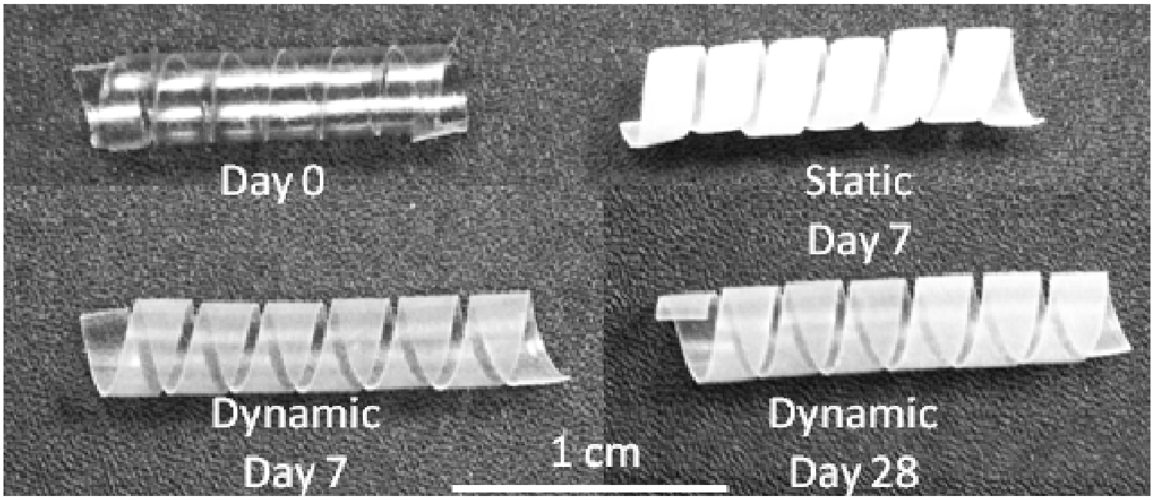

Figure 5.3 Helical bioresorbable scaffolds before and after submersion in PBS for various time periods under static and dynamic conditions.

5.3 RESULTS

The helical shape of the BRS at static flow was lost after 7 days of submersion in PBS, whereas it retained the initial shape even after 28 days of submersion in PBS at dynamic condition (Figure 5.3). Length of the scaffolds increased as they degraded.

Water uptake by the scaffolds are significantly affected by the nature of flow medium ($p < 0.001$) (Figure 5.4). Rate of water absorption increased abruptly after one weeks of submersion in static condition and continued till third weeks. Meanwhile, amount of water uptake in dynamic conditions very slowly increased over the 4 weeks of experiments. At the end of 4 weeks almost 1800 folds more water was absorbed in static condition than that of dynamic condition.

Hydrolytic degradation as result of random ester bonds scission between monomers took place immediately after submersion of BRS into the PBS irrespective to the flow condition (Figure 5.5). Since water absorption triggers degradation, BRS in static condition degrades significantly faster than that of the dynamic condition ($p < 0.001$).

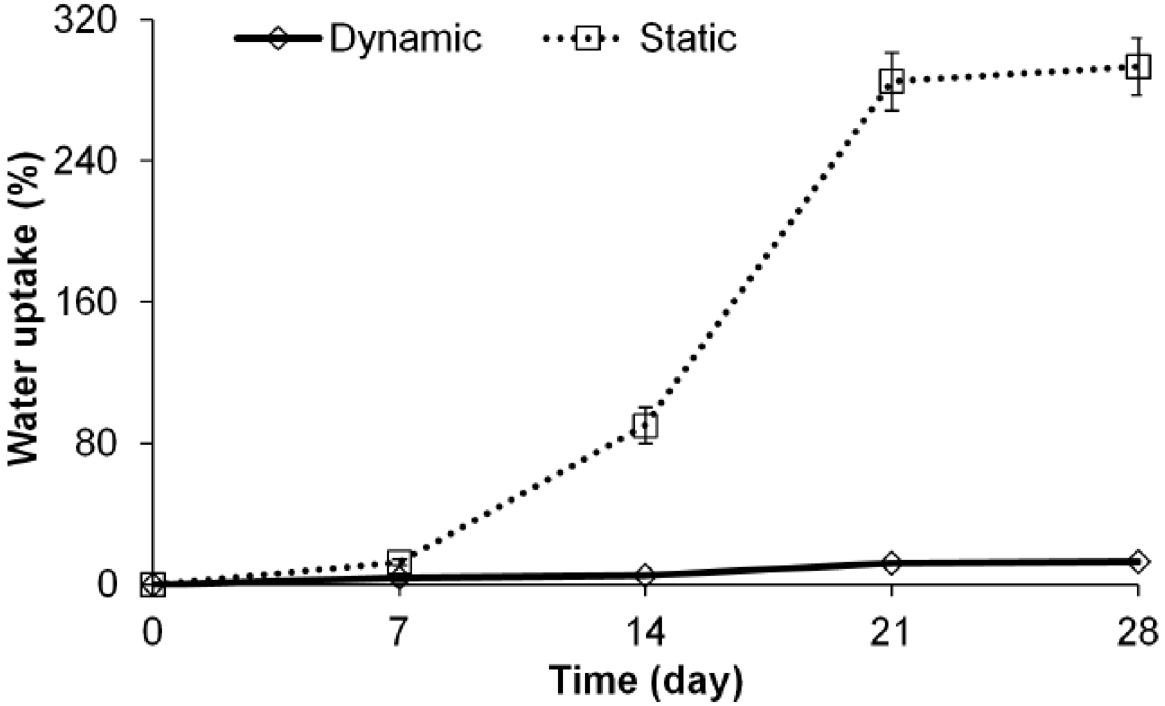

Figure 5.4 Water absorption by BRS under static and dynamic flow conditions after submersion in PBS at various time points.

BRS in static flow condition lost more than 60% of its initial M_w in 1 week, whereas more than 50% of initial M_w is still available after 4 weeks of submersion in PBS. Dynamic flow preserved more than 90% BRS M_w than static flow after 28 days of degradation. Distribution of oligomers and monomers inside the BRS were also influenced by the nature of flow. Generation of smaller oligomers due to degradation increased the PDI in the early stage, however after certain period of time (4 days and 2 weeks for static and dynamic conditions respectively) bigger molecules start to diminish that lowered the PDI. At the end of 28 days, oligomers having almost similar M_w were available in BRS under static flow condition as observed by the near unity PDI.

Erosion, as measured by the weight loss due to release of water soluble oligomers and monomers from the polymer matrix, was also significantly high for the BRS

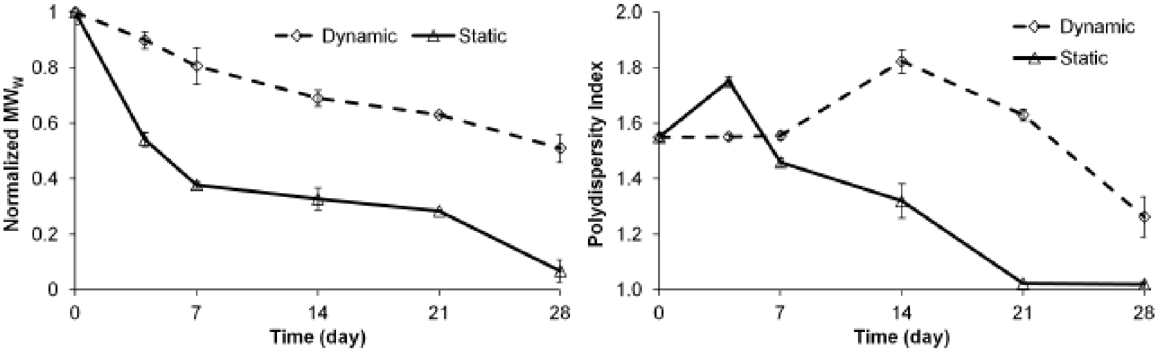

Figure 5.5 Normalized molecular weight **(A)** and polydispersity index **(B)** of BRS polymer matrix under static and dynamic flow conditions after submersion in PBS at various time points.

under static flow than the dynamic flow ($p < 0.01$) (Figure 5.6). Negligible weight loss was observed upto 1 week irrespective to the flow condition. After 1 week, BRS started to loose weight exponentially under static condition, whereas linearly and slowly loose under dynamic condition. After 28 of immersion, BRS lost 85% more of its weight under static condition than that of dynamic condition. Higher rate of water absorption than weight loss the bulk erosion of the BRS.

Characterization of scaffold mechanical property is very critical to understand its effectiveness to support and retain native vessel structure and prevent recoiling. Therefore, response in mechanical properties due to degradation and flow are important to investigate. All forces were normalized with corresponding scaffold length to minimize the effect of contact surface area. The toe regions, as defined by the distance required for 0 to 0.001 N mm^{-1} compressive load (Figure 5.7), exhibited by the BRS were not significantly affected by the flow after degradation for 1 week ($p > 0.05$). Compressive modulus (E_c) represented the radial strength of the scaffold and were calculated based on the slope of the linear regression model of force exerted by the scaffold after the toe region.

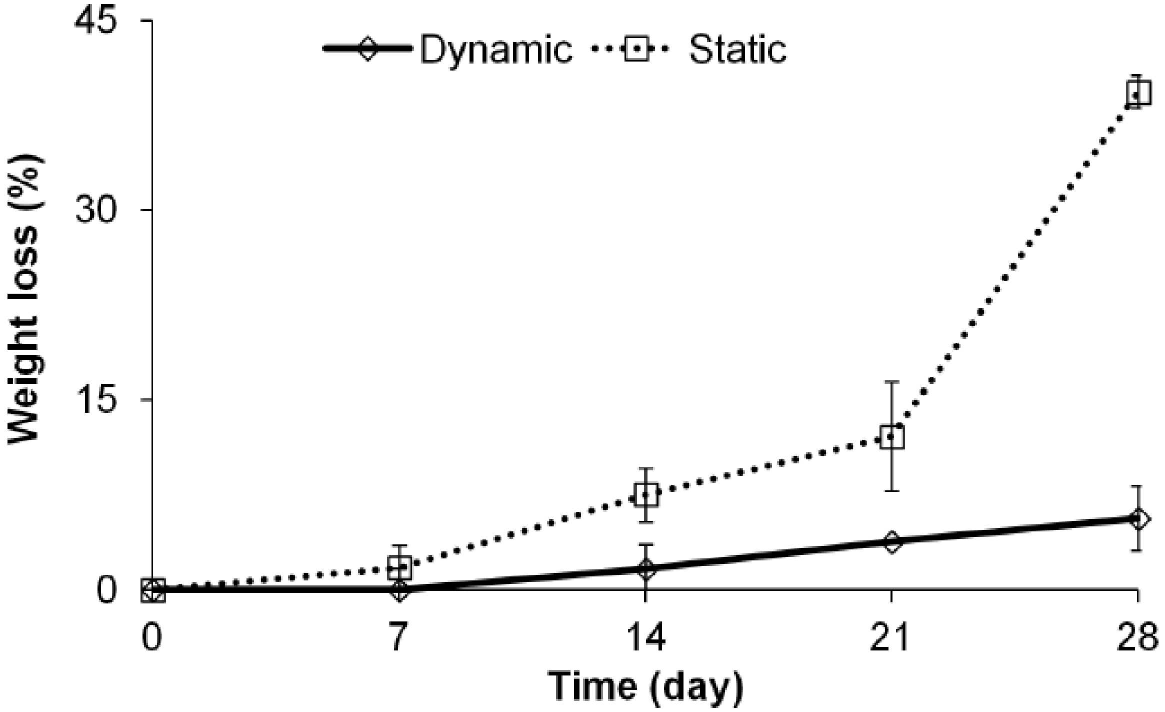

Figure 5.6 BRS weight loss under static and dynamic flow conditions after submersion in PBS at various time points.

Radial strength after 1 week degradation were significantly increased (more than 100%) when the BRS were exposed to flow ($p < 0.005$). BRS from the dynamic condition exerted force linearly until the maximum allowed force of the load cell. On the other hand, both elastic and plastic regions were observed when BRS from the static condition were subjected to compressive displacement. The average yield and ultimate strengths were approximately 0.05 N mm^{-1} and 0.055 N mm^{-1} respectively. Though BRS from static flow condition exhibited necking at high displacements, no breaking point (fracture) was observed with the investigated 1 mm displacement.

5.4 DISCUSSION

Inclusion of PEG markedly increased the water absoption that eventually enhanced the degradation and erosion processes significantly. PEG could restricts the release of

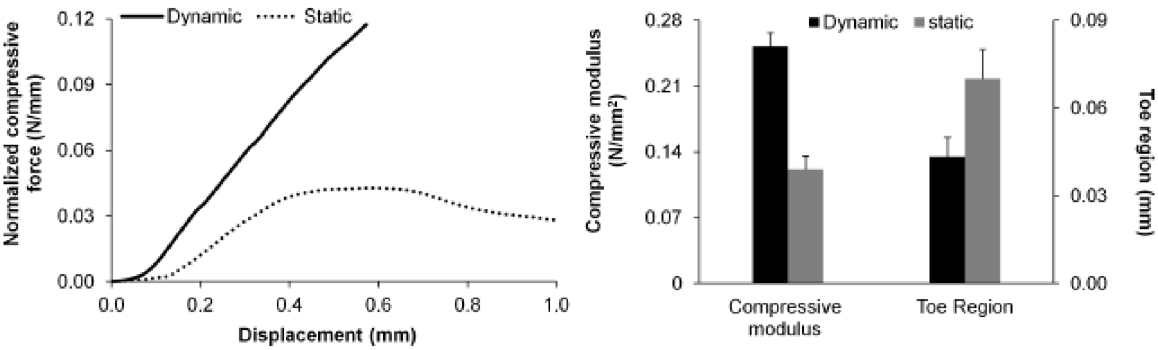

Figure 5.7 Force exerted by a representative BRS due to compression **(A)** and effect of flow on BRS compressive modulus and toe region **(B)** under static and dynamic flow conditions after submersion in PBS for one week.

soluble oligomers and monomers by obstructing the small pores in the early stage and thus increases the autocatalysis effect that explains the early fast degradation and slow erosion processes [36]. However, along with the increase in porosity, the effect of autocatalysis diminishes as the soluble species could easily released out into the bulk medium. PEG also increased the flexibility of the BRS under low displacement as observed by the toe region which is important as BRS is always under pulsetile flow in *in vivo* condition. Due to the toe region, the BRS can easily deform with the artery to accommodate the flow change without extra stress that could be harmful to the artery. Too much PEG could also make very flexible BRS which enhance the likelihood recoiling. Therefore, it is important to tune the PEG content by considering its effect degradation, erosion, and mechanical properties.

BRS *in vitro* performance matrices are significantly influenced by the nature of the flow of the medium. Dynamic flow condition markedly decreases the water absorption, degradation, erosion and radial strength. In the static flow condition, water can easily diffused into the scaffold (Figure 5.8A). Homogeneous water uptake as confirmed by the absent of no swelling fronts results uniform hydrolytic polymer chain scission all over the scaffold. As a result, the generated carboxylic acid groups lowers

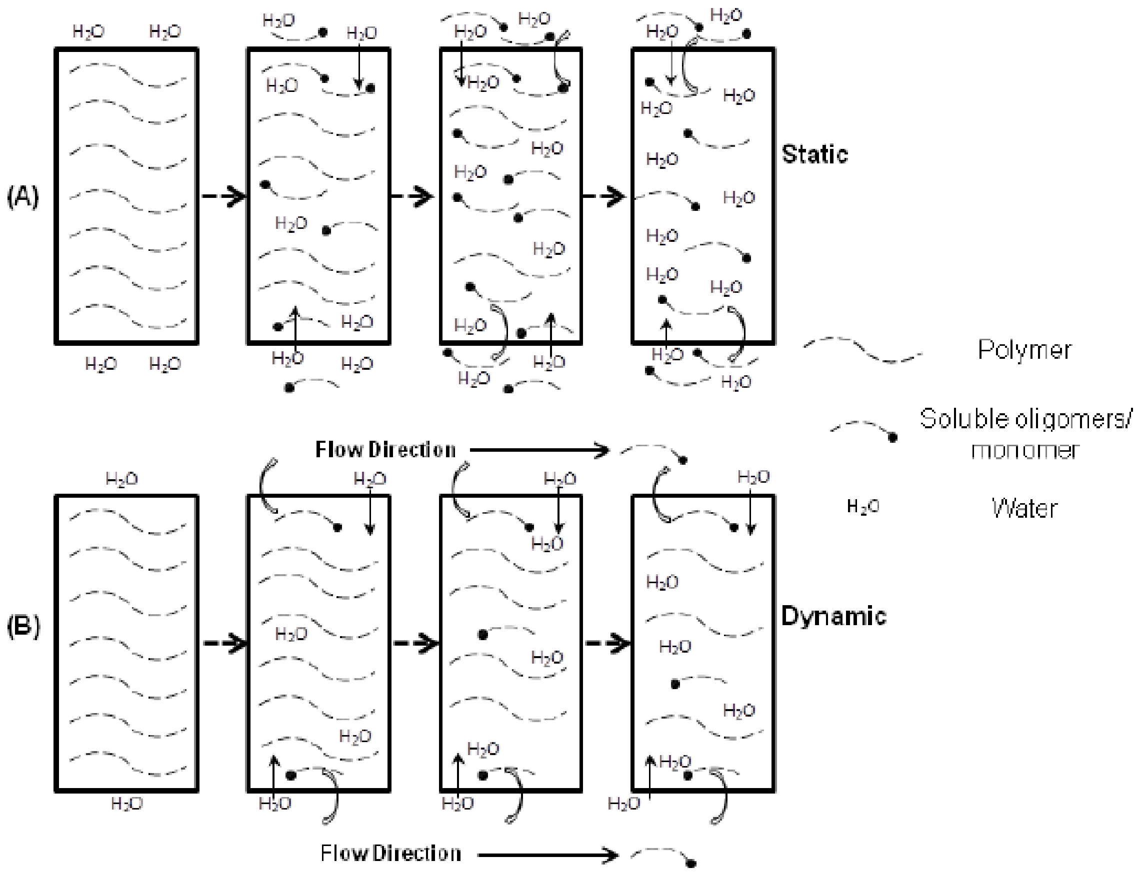

Figure 5.8 BRS polymer degradation/erosion mechanism under static **(A)** and dynamic **(B)** flow conditions.

the pH value inside the polymer scaffold and accelerates the degradation kinetics inside the polymer bulk [28]. As uniform neutral pH is maintained at the surface of the scaffold, a pH gradient is developed that slow down the degradation of the scaffold surface compared to the center. Scaffold mass loss occurs due to the release of soluble monomers and oligomers when the scaffolds forms a network of pores after certain critical degree of degradation[42].

In the dynamic flow condition, water diffusion inside the scaffold was decreased because of the flow direction, which delayed the hydrolytic cleavage of eater bonds inside the polymer matrix (Figure 5.8B). The cleavage of ester bonds occurred predominantly at the surface of the polymer because of probability of the water contact with polymer surface increased due to the medium flowing. However, this is not surface erosion as for surface erosion mass loss starts at the beginning of the experiment while M_w does not change in early stage [26]. In contrast, M_w started to loose from the beginning whereas no significant mass loss was observed till 2 weeks in current study. Mass loss in dynamic condition can be described as delayed bulk erosion. Generated carboxylic acid groups did not accumulate and washed out by flowing medium resulting constant pH inside the polymer matrix and cannot contribute in the hydrolytic degradation process, hence lowered the degradation process and erosion process accordingly.

Since mechanical properties of the polymeric scaffold are dependent on the M_w, degradation in dynamic condition preserves initial radial strength long than that of in static condition. Therefore, early fracture is likely in BRS when they are exposed to static condition. Performing future experiments at several intermediate flow rates followed under physiologic pulsetile flow would be interesting to investigate.

5.5 Conclusion

BRS *in vitro* performance matrixes are significantly affected by the nature of the medium flow. It is important to mention that to investigate any behavior of any polymeric BRS for endovascular applications, the BRS should be testes in dynamic condition as the behaviors in the simple static condition do not provide the big picture. This study will also assist to design implantation site-specific BRS as each artery are exposed to different flow condition.

Chapter 6

CONCLUSION

6.1 Overall Conclusion

Tissue remodeling and polymer degradation kinetics modulate lactic acid (LA) accumulation within adjacent arterial tissue in the case of a tissue-embedded, fully bioresorbable vascular scaffold (BVS) comprised of PLLA. On the other hand, peak LA concentrations were insensitive to large variation in the tissue metabolic rate, suggesting that metabolism is a secondary by-product clearance mechanism compared to diffusive and convective transport. Synchrony between rates of remodeling and degradation is predicted to minimize peak LA levels in local tissue over the scaffold lifetime. As BVS are increasingly considered for the treatment of coronary artery disease, insights on the production and tissue retention of degradation by-products can help predict clinical performance and provide a basis for iterative device design.

Advanced design of erodible endovascular scaffolds requires careful assessment of material properties that impact implant performance and safety in the arterial environment. Potential variations in polymer composition and structure differentially impact metrics of performance. Specifically, degradation is minimally affected by changes in either PLLA polydispersity or the initial degree of crystallinity, while erosion is sensitive to crystallinity. Additionally, scaffold degradation, erosion, and by-product accumulation were all responsive to lactide doping.

Personalized medical therapy is an emerging practice of medical treatment offering tailored solutions to each individual. Although changes in strut design and alternation of polymeric processing increase the vessel diameter working range, it is suggested to use size-specific BRSs for safe and effective clinical outcomes. Careful and adequate sizing of vessel diameter are of paramount importance for the correct performance of this scaffolding technique and require accurate assessment of vessel dimension by QCA prior to implantation. BRS in vitro performance matrixes are also significantly affected by the nature of the medium flow. It is important to mention that to investigate any behavior of any polymeric BRS for endovascular applications, the BRS should be testes in dynamic condition as the behaviors in the simple static condition do not provide the big picture. This study provides important insights to guide the future safe and effective use of vascular polymeric BRS in a patient specific manner.

6.2 FUTURE STUDIES

1. Effect of luminal blood flow rates on BRS performance: Based on the outcomes of dynamic flow effect on BRS performance, it will be interesting to investigate how different flow rates within the physiological will affect the BRS performance.

2. Effect of blood flow pulsatility on BRS performance: Blood flow pulsatility markedly altered the blood flow profiles adjacent to the strut, wall shear stress, and arterial wall drug accumulation [60]. Therefore, it will be also interesting to investigate the effect of blood flow pulsatility on BRS performance.

3. Effect of coronary artery curvature on BRS performance: Curvature of coronary arteries is different among individuals and even one single coronary artery dynamically changes in morphology through the heart cycle. Acute changes

in the geometry of coronary arteries after implantation of BVS can affect the clinical outcomes. The most important device property that determines these changes in vessel geometry is the conformability as described as the flexibility of a device in its expanded state with adaptation to the natural shape of the vessel, hence minimizing trauma to the vessel wall [13]. Flow profiles and stress distribution in the vessel wall are also affected by the curvature of the arteries [93]. Though current clinical trial indicates better conformability of BRS than convention metallic stent, further investigations will be required for to confirm this differences [24]. An *in vitro* model having controlled variation in vessel curvatures can be prepared to investigate the transient characteristics of the BRS which will assist to design *in vivo* experiments prior to expensive clinical studies.

BIBLIOGRAPHY

[1] Taiji Adachi, Yuki Osako, Mototsugu Tanaka, Masaki Hojo, and Scott J Hollister, *Framework for optimal design of porous scaffold microstructure by computational simulation of bone regeneration*, Biomaterials **27** (2006), no. 21, 3964–3972.

[2] Frank Alexis, *Factors affecting the degradation and drug-release mechanism of poly (lactic acid) and poly [(lactic acid)-co-(glycolic acid)]*, Polymer International **54** (2005), no. 1, 36–46.

[3] Harro Antheunis, Jan-Cees van der Meer, Matthijs de Geus, Andreas Heise, and Cor E Koning, *Autocatalytic equation describing the change in molecular weight during hydrolytic degradation of aliphatic polyesters*, Biomacromolecules **11** (2010), no. 4, 1118–1124.

[4] Harro Antheunis, Jan-Cees van der Meer, Matthijs de Geus, Wieb Kingma, and Cor E Koning, *Improved mathematical model for the hydrolytic degradation of aliphatic polyesters*, Macromolecules **42** (2009), no. 7, 2462–2471.

[5] Kyriacos A Athanasiou, Gabriele G Niederauer, and C Agrawal, *Sterilization, toxicity, biocompatibility and clinical applications of polylactic acid/polyglycolic acid copolymers*, Biomaterials **17** (1996), no. 2, 93–102.

[6] Melvin Avrami, *Kinetics of phase change. ii transformation-time relations for random distribution of nuclei*, The Journal of Chemical Physics **8** (1940), 212.

[7] Brinda Balakrishnan, John F Dooley, Gregory Kopia, and Elazer R Edelman, *Intravascular drug release kinetics dictate arterial drug deposition, retention, and distribution*, Journal of Controlled Release **123** (2007), no. 2, 100–108.

[8] Brinda Balakrishnan, Abraham R Tzafriri, Philip Seifert, Adam Groothuis, Campbell Rogers, and Elazer R Edelman, *Strut position, blood flow, and drug deposition implications for single and overlapping drug-eluting stents*, Circulation **111** (2005), no. 22, 2958–2965.

[9] Friederike von Burkersroda, Luise Schedl, and Achim Göpferich, *Why degradable polymers undergo surface erosion or bulk erosion*, Biomaterials **23** (2002), no. 21, 4221–4231.

[10] Yuhang Chen, Shiwei Zhou, and Qing Li, *Mathematical modeling of degradation for bulk-erosive polymers: Applications in tissue engineering scaffolds and drug delivery systems*, Acta Biomaterialia **7** (2011), no. 3, 1140–1149.

[11] ———, *Microstructure design of biodegradable scaffold and its effect on tissue regeneration*, Biomaterials **32** (2011), no. 22, 5003–5014.

[12] Antonio Colombo and Evangelia Karvouni, *Biodegradable stents âĂIJfulfilling the mission and stepping awayâĂİ*, Circulation **102** (2000), no. 4, 371–373.

[13] Antonio Colombo, Goran Stankovic, and Jeffrey W Moses, *Selection of coronary stents*, Journal of the American College of Cardiology **40** (2002), no. 6, 1021–1033.

[14] Christopher J Creel, Mark A Lovich, and Elazer R Edelman, *Arterial paclitaxel distribution and deposition*, Circulation Research **86** (2000), no. 8, 879–884.

[15] William M Deen, *Analysis of transport phenomena (topics in chemical engineering)*, vol. 3, Oxford University Press, New York, 1998.

[16] Roberto Diletti, Yoshinobu Onuma, Vasim Farooq, Josep Gomez-Lara, Salvatore Brugaletta, Robert Jan van Geuns, Evelyn Regar, Bernard de Bruyne, Dariusz Dudek, Leif Thuesen, et al., *6-month clinical outcomes following implantation of the bioresorbable everolimus-eluting vascular scaffold in vessels smaller or larger than 2.5 mm*, Journal of the American College of Cardiology **58** (2011), no. 3, 258–264.

[17] JT Dodge, B Greg Brown, Edward L Bolson, and Harold T Dodge, *Lumen diameter of normal human coronary arteries. influence of age, sex, anatomic variation, and left ventricular hypertrophy or dilation.*, Circulation **86** (1992), no. 1, 232–246.

[18] Raimund Erbel, Carlo Di Mario, Jozef Bartunek, Johann Bonnier, Bernard de Bruyne, Franz R Eberli, Paul Erne, Michael Haude, Bernd Heublein, Mark Horrigan, et al., *Temporary scaffolding of coronary arteries with bioabsorbable magnesium stents: a prospective, non-randomised multicentre trial*, The Lancet **369** (2007), no. 9576, 1869–1875.

[19] Jahid Ferdous, *Numerical modeling of local pharmacokinetics associated with drug-eluting stent.*, Ph.D. thesis, 2009.

[20] Jahid Ferdous, Vijaya B Kolachalama, and Tarek Shazly, *Impact of polymer structure and composition on fully resorbable endovascular scaffold performance*, Acta biomaterialia **9** (2013), no. 4, 6052–6061.

[21] David L Fischman, Martin B Leon, Donald S Baim, Richard A Schatz, Michael P Savage, Ian Penn, Katherine Detre, Lisa Veltri, Donald Ricci, Masakiyo Nobuyoshi, et al., *A randomized comparison of coronary-stent placement and balloon angioplasty in the treatment of coronary artery disease*, New England Journal of Medicine **331** (1994), no. 8, 496–501.

[22] Paul J. Flory, *Principles of polymer chemistry*, Cornell University Press, 1953.

[23] Susanne Fredenberg, Marie Wahlgren, Mats Reslow, and Anders Axelsson, *The mechanisms of drug release in poly (lactic-co-glycolic acid)-based drug delivery systemsâĂŤa review*, International journal of pharmaceutics **415** (2011), no. 1, 34–52.

[24] Josep Gomez-Lara, Hector M Garcia-Garcia, Yoshinobu Onuma, Scot Garg, Evelyn Regar, Bernard De Bruyne, Stefan Windecker, Dougal McClean, Leif Thuesen, Dariusz Dudek, et al., *A comparison of the conformability of everolimus-eluting bioresorbable vascular scaffolds to metal platform coronary stents*, JACC: Cardiovascular Interventions **3** (2010), no. 11, 1190–1198.

[25] Achim Göpferich, *Mechanisms of polymer degradation and erosion*, Biomaterials **17** (1996), no. 2, 103–114.

[26] Achim Göpferich and Robert Langer, *The influence of microstructure and monomer properties on the erosion mechanism of a class of polyanhydrides*, Journal of Polymer Science Part A: Polymer Chemistry **31** (1993), no. 10, 2445–2458.

[27] Niels Grabow, David P Martin, Klaus-Peter Schmitz, and Katrin Sternberg, *Absorbable polymer stent technologies for vascular regeneration*, Journal of Chemical Technology and Biotechnology **85** (2010), no. 6, 744–751.

[28] Iisoto Grizzi, H Garreau, S Li, and M Vert, *Hydrolytic degradation of devices based on poly (dl-lactic acid) size-dependence*, Biomaterials **16** (1995), no. 4, 305–311.

[29] A Grüntzig and HJ Schneider, *The percutaneous dilatation of chronic coronary stenoses–experiments and morphology].*, Schweizerische medizinische Wochenschrift **107** (1977), no. 44, 1588.

[30] Xiaoxiao Han and Jingzhe Pan, *A model for simultaneous crystallisation and biodegradation of biodegradable polymers*, Biomaterials **30** (2009), no. 3, 423–430.

[31] ______, *Polymer chain scission, oligomer production and diffusion: a two-scale model for degradation of bioresorbable polyesters*, Acta Biomaterialia **7** (2011), no. 2, 538–547.

[32] Tomoaki Higo, Yasunori Ueda, Jota Oyabu, Katsuki Okada, Mayu Nishio, Akio Hirata, Kazunori Kashiwase, Nobuyuki Ogasawara, Shinichi Hirotani, and Kazuhisa Kodama, *Atherosclerotic and thrombogenic neointima formed over sirolimus drug-eluting stentan angioscopic study*, JACC: Cardiovascular Imaging **2** (2009), no. 5, 616–624.

[33] Mark Hofman, Albert C van Rossum, Michiel Sprenger, and Nico Westerhof, *Assessment of flow in the right human coronary artery by magnetic resonance phase contrast velocity measurement: effects of cardiac and respiratory motion*, Magnetic resonance in medicine **35** (1996), no. 4, 521–531.

[34] http://www.britannica.com.

[35] http://www.who.int.

[36] Charlotte L Huang, Terry WJ Steele, Effendi Widjaja, Freddy YC Boey, Subbu S Venkatraman, and Joachim SC Loo, *The influence of additives in modulating drug delivery and degradation of plga thin films*, NPG Asia Materials **5** (2013), no. 7, e54.

[37] Chao-Wei Hwang and Elazer R Edelman, *Arterial ultrastructure influences transport of locally delivered drugs*, Circulation research **90** (2002), no. 7, 826–832.

[38] Ioannis Iakovou, Thomas Schmidt, Erminio Bonizzoni, Lei Ge, Giuseppe M Sangiorgi, Goran Stankovic, Flavio Airoldi, Alaide Chieffo, Matteo Montorfano, Mauro Carlino, et al., *Incidence, predictors, and outcome of thrombosis after successful implantation of drug-eluting stents*, JAMA: the journal of the American Medical Association **293** (2005), no. 17, 2126–2130.

[39] Refat Jabara, Nicolas Chronos, and Keith Robinson, *Novel bioabsorbable salicylate-based polymer as a drug-eluting stent coating*, Catheterization and Cardiovascular Interventions **72** (2008), no. 2, 186–194.

[40] Joseph Jagur-Grodzinski, *Polymers for tissue engineering, medical devices, and regenerative medicine. concise general review of recent studies*, Polymers for Advanced Technologies **17** (2006), no. 6, 395–418.

[41] O t Kedem and A Katchalsky, *Thermodynamic analysis of the permeability of biological membranes to non-electrolytes*, Biochimica et biophysica Acta **27** (1958), 229–246.

[42] Takeshi Kimura, Kenichi Abe, Satoshi Shizuta, Keita Odashiro, Yoshinori Yoshida, Koyu Sakai, Kazuaki Kaitani, Katsumi Inoue, Yoshihisa Nakagawa, Hiroyoshi Yokoi, et al., *Long-term clinical and angiographic follow-up after coronary stent placement in native coronary arteries*, Circulation **105** (2002), no. 25, 2986–2991.

[43] Masaki Kobayashi, Itaru Fujita, Shirou Itagaki, Takeshi Hirano, and Ken Iseki, *Transport mechanism for l-lactic acid in human myocytes using human prototypic embryonal rhabdomyosarcoma cell line (rd cells)*, Biological and Pharmaceutical Bulletin **28** (2005), no. 7, 1197–1201.

[44] Joachim Kohn and Joan Zeltinger, *Degradable, drug-eluting stents: a new frontier for the treatment of coronary artery disease*, (2005).

[45] Vijaya B Kolachalama, Evan G Levine, and Elazer R Edelman, *Luminal flow amplifies stent-based drug deposition in arterial bifurcations*, PloS one **4** (2009), no. 12, e8105.

[46] Vijaya B Kolachalama, Stephen D Pacetti, Joseph W Franses, John J Stankus, Hugh Q Zhao, Tarek Shazly, Alexander Nikanorov, Lewis B Schwartz, Abraham R Tzafriri, and Elazer R Edelman, *Mechanisms of tissue uptake and retention in zotarolimus-coated balloon therapy*, Circulation **127** (2013), no. 20, 2047–2055.

[47] Robert Langer and David A Tirrell, *Designing materials for biology and medicine*, Nature **428** (2004), no. 6982, 487–492.

[48] Luciana Lisa Lao, Subbu S Venkatraman, and Nicholas A Peppas, *A novel model and experimental analysis of hydrophilic and hydrophobic agent release*

from biodegradable polymers, Journal of Biomedical Materials Research Part A **90** (2009), no. 4, 1054–1065.

[49] Jan W Leenslag, Albert J Pennings, Ruud RM Bos, Fred R Rozema, and Geert Boering, *Resorbable materials of poly (l-lactide): Vii. in vivo and in vitro degradation*, Biomaterials **8** (1987), no. 4, 311–314.

[50] Andrew D Levin, Neda Vukmirovic, Chao-Wei Hwang, and Elazer R Edelman, *Specific binding to intracellular proteins determines arterial transport properties for rapamycin and paclitaxel*, Proceedings of the National Academy of Sciences of the United States of America **101** (2004), no. 25, 9463–9467.

[51] Hongbo Li and Michel A Huneault, *Effect of nucleation and plasticization on the crystallization of poly (lactic acid)*, Polymer **48** (2007), no. 23, 6855–6866.

[52] Mark A Lovich, Chris Creel, Kristy Hong, Chao-Wei Hwang, and Elazer R Edelman, *Carrier proteins determine local pharmacokinetics and arterial distribution of paclitaxel*, Journal of pharmaceutical sciences **90** (2001), no. 9, 1324–1335.

[53] Lichun Lu, Charles A Garcia, and Antonios G Mikos, *In vitro degradation of thin poly (dl-lactic-co-glycolic acid) films*, Journal of biomedical materials research **46** (1999), no. 2, 236–244.

[54] Guy Meyer, Alain Tedgui, et al., *Effects of pressure-induced stretch and convection on low-density lipoprotein and albumin uptake in the rabbit aortic wall*, Circulation research **79** (1996), no. 3, 532–540.

[55] John C Middleton and Arthur J Tipton, *Synthetic biodegradable polymers as orthopedic devices*, Biomaterials **21** (2000), no. 23, 2335–2346.

[56] Robert A Miller, John M Brady, and Duane E Cutright, *Degradation rates of oral resorbable implants (polylactates and polyglycolates): rate modification with changes in pla/pga copolymer ratios*, Journal of biomedical materials research **11** (1977), no. 5, 711–719.

[57] Lakshmi S Nair and Cato T Laurencin, *Biodegradable polymers as biomaterials*, Progress in polymer science **32** (2007), no. 8, 762–798.

[58] Soji Nishio, Kunihiko Kosuga, Keiji Igaki, Masaharu Okada, Eisho Kyo, Takafumi Tsuji, Eiji Takeuchi, Yasutaka Inuzuka, Shinsaku Takeda, Tatsuhiko Hata, et al., *Long-term (> 10 years) clinical outcomes of first-in-human biodegradable*

poly-l-lactic acid coronary stentsclinical perspective igaki-tamai stents, Circulation **125** (2012), no. 19, 2343–2353.

[59] Yoshinobu Onuma, Patrick W Serruys, Laura EL Perkins, Takayuki Okamura, Nieves Gonzalo, Hector M García-García, Evelyn Regar, Marika Kamberi, Jennifer C Powers, Richard Rapoza, et al., *Intracoronary optical coherence tomography and histology at 1 month and 2, 3, and 4 years after implantation of everolimus-eluting bioresorbable vascular scaffolds in a porcine coronary artery modelclinical perspective an attempt to decipher the human optical coherence tomography images in the absorb trial*, Circulation **122** (2010), no. 22, 2288–2300.

[60] Yosinobu Onuma and Patrick W Serruys, *Bioresorbable scaffold the advent of a new era in percutaneous coronary and peripheral revascularization?*, Circulation **123** (2011), no. 7, 779–797.

[61] John A Ormiston, Frederic De Vroey, Patrick W Serruys, and Mark WI Webster, *Bioresorbable polymeric vascular scaffolds a cautionary tale*, Circulation: Cardiovascular Interventions **4** (2011), no. 5, 535–538.

[62] John A Ormiston, Patrick W Serruys, Evelyn Regar, Dariusz Dudek, Leif Thuesen, Mark WI Webster, Yoshinobu Onuma, Hector M Garcia-Garcia, Robert McGreevy, and Susan Veldhof, *A bioabsorbable everolimus-eluting coronary stent system for patients with single de-novo coronary artery lesions (absorb): a prospective open-label trial*, The Lancet **371** (2008), no. 9616, 899–907.

[63] John A Ormiston and Patrick WS Serruys, *Bioabsorbable coronary stents*, Circulation: Cardiovascular Interventions **2** (2009), no. 3, 255–260.

[64] JC Palmaz, DT Kopp, H Hayashi, RA Schatz, G Hunter, FO Tio, O Garcia, R Alvarado, C Rees, and SC Thomas, *Normal and stenotic renal arteries: experimental balloon-expandable intraluminal stenting.*, Radiology **164** (1987), no. 3, 705–708.

[65] Elzbieta Pamula and Elzbieta Menaszek, *In vitro and in vivo degradation of poly (l-lactide-co-glycolide) films and scaffolds*, Journal of Materials Science: Materials in Medicine **19** (2008), no. 5, 2063–2070.

[66] Giuseppe Perale, P Arosio, D Moscatelli, V Barri, M Müller, S Maccagnan, and M Masi, *A new model of resorbable device degradation and drug release: Transient 1-dimension diffusional model*, Journal of controlled release **136** (2009), no. 3, 196–205.

[67] Santosh Prabhu and Syed Hossainy, *Modeling of degradation and drug release from a biodegradable stent coating*, Journal of Biomedical Materials Research Part A **80** (2007), no. 3, 732–741.

[68] Filippo Rossi, Tommaso Casalini, Edoardo Raffa, Maurizio Masi, and Giuseppe Perale, *Bioresorbable polymer coated drug eluting stent: A model study*, Molecular Pharmaceutics **9** (2012), no. 7, 1898–1910.

[69] ZM Ruggeri, *Mechanisms initiating platelet thrombus formation.*, Thrombosis and haemostasis **78** (1997), no. 1, 611–616.

[70] Swapan Kumar Saha and Hideto Tsuji, *Effects of molecular weight and small amounts of d-lactide units on hydrolytic degradation of poly (l-lactic acid) s*, Polymer degradation and stability **91** (2006), no. 8, 1665–1673.

[71] Gesine Schliecker, Carsten Schmidt, Stefan Fuchs, and Thomas Kissel, *Characterization of a homologous series of d, l-lactic acid oligomers; a mechanistic study on the degradation kinetics in vitro*, Biomaterials **24** (2003), no. 21, 3835–3844.

[72] Daniel J Schneck, *An outline of cardiovascular structure and function*, Biomedical Engineering Handbook Bd **1** (2010), 1–1.

[73] Patrick W Serruys, Yoshinobu Onuma, John A Ormiston, Bernard de Bruyne, Evelyn Regar, Dariusz Dudek, Leif Thuesen, Pieter C Smits, Bernard Chevalier, Dougal McClean, et al., *Evaluation of the second generation of a bioresorbable everolimus drug-eluting vascular scaffold for treatment of de novo coronary artery stenosisclinical perspective six-month clinical and imaging outcomes*, Circulation **122** (2010), no. 22, 2301–2312.

[74] Tahmer Sharkawi, Frederick Cornhill, Antoine Lafont, Patrick Sabaria, and Michel Vert, *Intravascular bioresorbable polymeric stents: A potential alternative to current drug eluting metal stents*, Journal of pharmaceutical sciences **96** (2007), no. 11, 2829–2837.

[75] Tarek Shazly, Vijaya B Kolachalama, Jahid Ferdous, James P Oberhauser, Syed Hossainy, and Elazer R Edelman, *Assessment of material by-product fate from bioresorbable vascular scaffolds*, Annals of biomedical engineering **40** (2012), no. 4, 955–965.

[76] Juergen Siepmann, Khaled Elkharraz, Florence Siepmann, and Diana Klose, *How autocatalysis accelerates drug release from plga-based microparticles: a quantitative treatment*, Biomacromolecules **6** (2005), no. 4, 2312–2319.

[77] Ulrich Sigwart, Jacques Puel, Velimir Mirkovitch, Francis Joffre, and Lukas Kappenberger, *Intravascular stents to prevent occlusion and re-stenosis after transluminal angioplasty*, New England Journal of Medicine **316** (1987), no. 12, 701–706.

[78] Sidney C Smith, Ted E Feldman, John W Hirshfeld, Alice K Jacobs, Morton J Kern, Spencer B King, Douglass A Morrison, William W O'Neill, Hartzell V Schaff, Patrick L Whitlow, et al., *Acc/aha/scai 2005 guideline update for percutaneous coronary interventionâĂŤsummary article: a report of the american college of cardiology/american heart association task force on practice guidelines (acc/aha/scai writing committee to update the 2001 guidelines for percutaneous coronary intervention)*, Catheterization and cardiovascular interventions **67** (2006), no. 1, 87–112.

[79] João S Soares and Paolo Zunino, *A mixture model for water uptake, degradation, erosion and drug release from polydisperse polymeric networks*, Biomaterials **31** (2010), no. 11, 3032–3042.

[80] RS Stack, RM Califf, HR Phillips, DB Pryor, PJ Quigley, RP Bauman, JE Tcheng, and JC Greenfield Jr, *Interventional cardiac catheterization at duke medical center.*, The American journal of cardiology **62** (1988), no. 10 Pt 2, 3F.

[81] Nanfeng Sun, Nigel B Wood, Alun D Hughes, Simon AM Thom, and X Yun Xu, *Fluid-wall modelling of mass transfer in an axisymmetric stenosis: effects of shear-dependent transport properties*, Annals of biomedical engineering **34** (2006), no. 7, 1119–1128.

[82] Shigeru Tada and John M Tarbell, *Fenestral pore size in the internal elastic lamina affects transmural flow distribution in the artery wall*, Annals of biomedical engineering **29** (2001), no. 6, 456–466.

[83] Hideo Tamai, Keiji Igaki, Eisho Kyo, Kunihiko Kosuga, Akiyoshi Kawashima, Shigeo Matsui, Hidenori Komori, Takafumi Tsuji, Seiichiro Motohara, and Hiromu Uehata, *Initial and 6-month results of biodegradable poly-l-lactic acid coronary stents in humans*, Circulation **102** (2000), no. 4, 399–404.

[84] AG Thombre and KJ Himmelstein, *A simultaneous transport-reaction model for controlled drug delivery from catalyzed bioerodible polymer matrices*, AIChE journal **31** (1985), no. 5, 759–766.

[85] Hideto Tsuji and Yoshito Ikada, *Properties and morphology of poly (l-lactide) 4. effects of structural parameters on long-term hydrolysis of poly (l-lactide) in*

phosphate-buffered solution, Polymer Degradation and Stability **67** (2000), no. 1, 179–189.

[86] A Rami Tzafriri, Andrew D Levin, and Elazer R Edelman, *Diffusion-limited binding explains binary dose response for local arterial and tumour drug delivery*, Cell proliferation **42** (2009), no. 3, 348–363.

[87] Abraham R Tzafriri, Neda Vukmirovic, Vijaya B Kolachalama, Irina Astafieva, and Elazer R Edelman, *Lesion complexity determines arterial drug distribution after local drug delivery*, Journal of Controlled Release **142** (2010), no. 3, 332–338.

[88] J ürgen Pache, Adnan Kastrati, Julinda Mehilli, Helmut Schühlen, Franz Dotzer, J örg Hausleiter, Martin Fleckenstein, Franz-Josef Neumann, Ulrich Sattelberger, Claus Schmitt, et al., *Intracoronary stenting and angiographic results: strut thickness effect on restenosis outcome (isar-stereo-2) trial*, Journal of the American College of Cardiology **41** (2003), no. 8, 1283–1288.

[89] Subbu Venkatraman, Tan Lay Poh, Tjong Vinalia, Koon Hou Mak, and Freddy Boey, *Collapse pressures of biodegradable stents*, Biomaterials **24** (2003), no. 12, 2105–2111.

[90] Horst A von Recum, Robert L Cleek, Suzanne G Eskin, and Antonios G Mikos, *Degradation of polydispersed poly (l-lactic acid) to modulate lactic acid release*, Biomaterials **16** (1995), no. 6, 441–447.

[91] Ying Wang, *Modelling degradation of bioresorbable polymeric devices*, Ph.D. thesis, University of Leicester, 2009.

[92] Ying Wang, Jingzhe Pan, Xiaoxiao Han, Csaba Sinka, and Lifeng Ding, *A phenomenological model for the degradation of biodegradable polymers*, Biomaterials **29** (2008), no. 23, 3393–3401.

[93] David C Warltier, Judy R Kersten, and Paul S Pagel, *Alterations in regional vascular geometry produced by theoretical stent implantation influence distributions of wall shear stress: analysis of a curved coronary artery using 3d computational fluid dynamics modeling*, Biomedical engineering online **5** (2006), 40.

[94] NA Weir, FJ Buchanan, JF Orr, and GR Dickson, *Degradation of poly-l-lactide. part 1: in vitro and in vivo physiological temperature degradation*, Proceedings of the Institution of Mechanical Engineers, Part H: Journal of Engineering in Medicine **218** (2004), no. 5, 307–319.

[95] Ning Yang and Kambiz Vafai, *Modeling of low-density lipoprotein (ldl) transport in the artery-effects of hypertension*, International Journal of Heat and Mass Transfer **49** (2006), no. 5, 850–867.

[96] Hengxing Yu, Nanxun Huang, Chaosheng Wang, and Zhilian Tang, *Modeling of poly (l-lactide) thermal degradation: Theoretical prediction of molecular weight and polydispersity index*, Journal of applied polymer science **88** (2003), no. 11, 2557–2562.

[97] Paolo Zunino, *Multidimensional pharmacokinetic models applied to the design of drug-eluting stents*, Cardiovascular Engineering: An International Journal **4** (2004), no. 2, 181–191.

Copyright Clearance for Chapter 2 This is a License Agreement between Jahid Ferdous (You) and Springer (Springer) provided by Copyright Clearance Center (CCC). The license consists of your order details, the terms and conditions provided by Springer, and the payment terms and conditions. All payments must be made in full to CCC. For payment instructions, please see information listed at the bottom of this form.

License Number: 3371970870223

License date: Apr 18, 2014

Licensed content publisher: Springer

Licensed content publication: Annals of Biomedical Engineering

Licensed content title: Assessment of Material By-Product Fate from Bioresorbable Vascular Scaffolds

Licensed content author: Tarek Shazly

Licensed content date: Jan 1, 2011

Volume number: 40

Issue number: 4

Type of Use: Thesis/Dissertation

Portion: Full text

Number of copies: 1

Author of this Springer article: Yes and you are a contributor of the new work
Title of your thesis /dissertation: Identifying Performance Criteria of Fully Bioresorbable Scaffolds for Endovascular Applications
Expected completion date: Apr 2014
Estimated size(pages): 109

Copyright Clearance for Chapter 3 This is a License Agreement between Jahid Ferdous (You) and Elsevier (Elsevier) provided by Copyright Clearance Center (CCC). The license consists of your order details, the terms and conditions provided by Elsevier, and the payment terms and conditions. All payments must be made in full to CCC. For payment instructions, please see information listed at the bottom of this form.
Supplier: Elsevier Limited, The Boulevard,Langford Lane, Kidlington,Oxford,OX5 1GB,UK
Registered Company Number: 1982084
Customer name: Jahid Ferdous
Customer address: 1035 Comanchee trail, West Columbia, SC 29169
License number: 3371971221618
License date: Apr 18, 2014
Licensed content publisher: Elsevier
Licensed content publication: Acta Biomaterialia
Licensed content title Impact of polymer structure and composition on fully resorbable endovascular scaffold performance
Licensed content author Jahid Ferdous,Vijaya B. Kolachalama,Tarek Shazly
Licensed content date: April 2013
Licensed content volume number: 9
Licensed content issue number: 4

Number of pages: 10

Start Page: 6052

End Page: 6061

Type of Use reuse: in a thesis/dissertation

Intended publisher of new work: other

Portion full: article

Format: both print and electronic

Are you the author of this Elsevier article?: Yes

Will you be translating?: No

Title of your thesis/dissertation: Identifying Performance Criteria of Fully Bioresorbable Scaffolds for Endovascular Applications

Expected completion date: Apr 2014

Estimated size (number of pages): 109